Universität Hamburg
Department Physik

From SuperWIMPs to Decaying Dark Matter: Models, Bounds and Indirect Searches

Dissertation

zur Erlangung des Doktorgrades

des Department Physik

der Universität Hamburg

vorgelegt von

Christoph Weniger

aus Wuppertal

Hamburg

2010

Gutachter der Dissertation:	Dr. A. Ringwald
	Prof. Dr. G. Sigl
	Prof. Dr. D. Hooper
Gutachter der Disputation:	Dr. A. Ringwald
	Prof. Dr. G. Moortgat-Pick
Datum der Disputation:	3. Februar 2010
Vorsitzender des Prüfungsausschusses:	Dr. M. Martins
Vorsitzender des Promotionsausschusses:	Prof. Dr. J. Bartels
Dekan des Fachbereichs Physik:	Prof. Dr. H. Graener

Zusammenfassung

Trotz größter experimenteller und theoretischer Anstrengungen ist die Frage nach der Teilchennatur der Dunklen Materie ungelöst. Neben den paradigmatischen WIMPs (*Weakly Interacting Massive Particles*) existieren viele theoretisch gut motivierte Modelle, die Kopplungen zwischen Dunkler Materie und Standardmodellteilchen vorhersagen welche viel schwächer als elektroschwach sind. In diesen Fällen ergeben sich eine ganze Reihe von neuen Phänomenen, die vom möglichen Einfluss auf die Kosmologie des frühen Universums bis hin zu Modellen mit zerfallender Dunkler Materie reichen.

In dieser Arbeit beschäftigen wir uns mit verschiedenen Aspekten solcher superschwach koppelnder Dunkler Materie im Allgemeinen, und unter spezieller Berücksichtigung von *hidden* $U(1)_X$ *gauginos*, die kinetisch mit der Hyperladung des minimalen supersymmetrischen Standardmodells mischen. Dabei nehmen wir an, dass – in Analogie zum Elektromagnetismus – die $U(1)_X$ ungebrochen bleibt. Aus Berechnungen der thermischen Produktion der hidden $U(1)_X$ gauginos im frühen Universum und der möglichen Wechselwirkung mit primordialer Nukleosynthese und Stukturbildung leiten wir Schranken an die Modellparameter ab. Wir studieren auch die in diesem Modell mögliche Produktion von exotischen Beiträgen zur kosmischen Strahlung in Hinblick auf die aktuellen Meßergebnisse der Satellitenexperimente PAMELA und Fermi LAT.

Darüberhinaus betrachten wir die möglichen Signaturen von zerfallender Dunkler Materie in der kosmischen Strahlung auch unabhängig von konkreten teilchenphysikalischen Modellen. Dabei konzentrieren wir uns auf die Frage, inwieweit der von PAMELA beobachtete Anstieg des Positronenanteils bei Strahlungsenergien oberhalb von 10 GeV zerfallender Dunkler Materie zugeschrieben werden kann. Aus diesen Ergebnissen leiten wir dann entsprechende Vorhersagen für die kosmische Gammastrahlung ab, wie sie derzeit vom Fermi LAT gemessen wird. Wir schlagen die dem vorhergesagten Gammasignal inhärente dipolartige Anisotropie vor, um es vom extragalaktischen Gammastrahlungshintergrund zu unterscheiden.

Abstract

Despite lots of observational and theoretical efforts, the particle nature of dark matter remains unknown. Beyond the paradigmatic WIMPs (*Weakly Interacting Massive Particles*), many theoretically well motivated models exist where dark matter interacts much more weakly than electroweak with Standard Model particles. In this case new phenomena occur, like the decay of dark matter or the interference with the standard cosmology of the early Universe.

In this thesis we study some of these aspects of superweakly coupled dark matter in general, and in the special case of *hidden* $U(1)_X$ *gauginos* that kinetically mix with hypercharge. There, we will assume that the gauge group remains unbroken, similar to the Standard Model $U(1)_{\rm em}$. We study different kinds of cosmological bounds, including bounds from thermal overproduction, from primordial nucleosynthesis and from structure formation. Furthermore, we study the possible cosmic-ray signatures predicted by this scenario, with emphasis on the electron and positron channel in light of the recent observations by PAMELA and Fermi LAT.

Moreover we study the cosmic-ray signatures of decaying dark matter independently of concrete particle-physics models. In particular we analyze in how far the rise in the positron fraction above 10 GeV, as observed by PAMELA, can be explained by dark matter decay. Lastly, we concentrate on related predictions for gamma-ray observations with the Fermi LAT, and propose to use the dipole-like anisotropy of the prompt gamma-ray dark matter signal to distinguish exotic dark matter contributions from the extragalactic gamma-ray background.

Meinen Eltern gewidmet

Contents

Chapter 1

Introduction

Evidence for the existence of a large fraction of dark (non-luminous) matter in the Universe comes from many different observations [1–6]: For example from rotation curves of spiral galaxies and the peculiar velocities of stars inside of dwarf spheroidals, which both indicate that these objects are mostly dominated by some kind of non-luminous matter that cannot be accounted for by the observed stars or the galactic gas; from the X-ray emission of intra-cluster gas and from weak gravitational lensing, which confirm the same dominance of non-luminous matter also on cluster scales; or from observations of the angular anisotropies of the *Cosmic Microwave Background* (CMB) and the formation of the *Large Scale Structure* (LSS) of galaxies, which both can only be understood in the presence of a sizeable and very weakly interacting gravitating matter component.

After the pioneering work of Fritz Zwicky in the 1930s [7] and of Vera Rubin in the early 1970s [8], much efforts were made to understand whether the gravitating substance seen in galaxies and galaxy clusters could be accounted for by some combination of baryonic matter, or whether it required particles and mechanisms that were not allegeable within the Standard Model of particle physics [4, 5]. By now it is widely established that the nature of dark matter lies indeed beyond the realms of the Standard Model. Confidence is mainly coming from a detailed study of *Big Bang Nucleosynthesis* (BBN) and observations of LSS on cluster scales, but also from *e.g.* a detailed study of the CMB anisotropies and from negative results of searches for *Massive Compact Halo Objects* (MACHOs) [1, section 22].

Being physics beyond the Standard Model, concrete predictions and optimal search strategies for non-baryonic dark matter become notoriously de-

pendent on the way the Standard Model is extended. Luckily, existing theoretical drawbacks of the Standard Model (like the hierarchy problem and the strong CP problem) often suggest extensions that predict or can very well accommodate dark matter particles. Indeed, WIMP dark matter is strongly supported by the observation that a mechanism stabilizing the Higgs mass in general requires new weakly interacting particles with masses at the electroweak scale. One popular manifestation of this idea is the *Minimal Supersymmetric Standard Model* (MSSM, see Ref. [9]) with a neutralino as *Lightest Supersymmetric Particle* (LSP) [2]. The neutralino is stable due to R-parity conservation and constitutes a typical and very well studied WIMP candidate, with fairly precise predictions for direct and indirect searches. On the other hand, the solution of the strong CP problem via the Peccei-Quinn mechanism [10], which requires the introduction of a new dynamical scalar field with appropriate charges, predicts the axion as new particle [11–13]. The axion is a pseudo-scalar that can well be dark matter due to non-thermal production in the early Universe, although it has particle properties, like a sub-eV mass and strongly suppressed couplings, that are completely different from any WIMP dark matter candidate.

However, predictions from extensions of the Standard Model are far from unique, and more elaborate models in context of *e.g.* supergravity [14, 15], string theory [16] and models with extra dimensions (see *e.g.* Ref. [17]) predict or allow a multitude of possible dark matter candidates that all come with their own peculiar properties and features [3, 6]. One well motivated and known example is the gravitino, which is associated with local supersymmetry transformations of supergravity, and which constitutes a dark matter candidate with Planck-scale suppressed couplings to the visible world [18, 19]. Another interesting example, on which we will concentrate in part of this work, is the gaugino of a very weakly coupled hidden $U(1)_X$ gauge group. Such a *hidden* gauge group, under which Standard Model particles are not charged, could couple to the low energy visible world in different ways via higher-dimensional operators, but in particular the possible kinetic mixing with the hypercharge $U(1)_Y$, which constitutes a *renormalizable* coupling, is intriguing and leads to clean predictions for cosmology and indirect searches [20, 21].

Common features of gravitino and hidden $U(1)_X$ gaugino dark matter are the superweak coupling to the visible world, a mass that often lies in the GeV–TeV regime, and the fact that they are typically produced non-

thermally in the late decay of other particles. Particles with these features were dubbed *superWIMPs* in the literature [22], and they share a similar phenomenology with regard to cosmology and collider physics. Indeed, being superweakly coupled to their parent particle, they are often produced as late as minutes or hours after the Big Bang, and this production can interfere with BBN or structure formation and might lead to observable effects. Furthermore, the longevity of their parent particles is a common collider signature of superWIMP scenarios.

Primordial Nucleosynthesis, or BBN, is the fusion of primordial elements, mainly D, ^{3}He, ^{4}He and ^{7}Li, from protons and neutrons, and takes place between 3 and 20 min after Big Bang, see *e.g.* Ref. [23]. During this time, the temperature of the Universe drops well below the bounding energies of the different elements, allowing them to form without being destroyed subsequently by interaction with the hot photon gas. After this time, the plasma becomes too diluted, due to the expansion of the Universe, and the fusion reactions freeze out. The details of BBN are very well studied, and main uncertainties stem from the required nuclear cross sections. The standard BBN scenario depends essentially on one free parameter, the baryon density, and predictions of this standard scenario agree very well with current observations [1, section 20]. As mentioned above, exotic physics like superWIMPs could strongly interfere with BBN [24]: The byproducts of the decay of their parent particles could release large amounts of electromagnetic or hadronic energy into the primordial plasma during BBN, destroying some of the fragile elements and changing their abundance [22, 25–27]. Furthermore, if the parent particle is charged, it could form bound states with ^{4}He and ^{8}Be , leading to a catalytic production of ^{6}Li and ^{9}Be [28, 29]. The non-observation of large deviations from the standard BBN scenario puts strong constraints on any superWIMP model.

SuperWIMP particles are typically produced with a large initial momentum and they can travel large distances before they again become non-relativistic due to the expansion of the Universe. This distance corresponds to the particle's free-streaming length and characterizes the scale on which primordial density fluctuations are washed out during superWIMP dark matter production [30, 31]. This wash-out of small scale fluctuations has direct impact on structure formation, and is actually best seen in the density distribution of neutral hydrogen clouds, which can be inferred from observations of the Lyman-α forest at higher redshifts $z \gtrsim 2$ [32]. Current upper bounds on the free-streaming scale are of the scale of galaxy groups, and it would be

challenging to derive these bounds from observations at lower redshifts, since there fluctuations on the relevant scales have already entered their non-linear regime. For superWIMPs, free-streaming bounds directly constrain their initial momentum and the lifetime of their parent particles [33–36]. But apart from the possibility of constraining dark matter scenarios, it was also pointed out that superWIMPs could be a possible solution to the "missing satellite" problem, which denotes the apparent mismatch between the large number of satellite halos predicted by N-body simulations, and the smaller number of actually observed satellite galaxies [37]. A wash-out of small scale fluctuations would reduce the number of small dark matter halos, increasing the agreement between theory and observation [31, 38].

As mentioned above, a typical collider signature for superWIMP dark matter is the possible observation of its long-lived parent particles. Depending on its lifetime, the parent particle (which is often the next-to-lightest supersymmetric particle, NLSP) could decay inside the detector, producing events with displaced vertices. If it is charged (*e.g.* a stau NLSP) it would furthermore generate heavily ionizing charged tracks inside the detector [39]. Although long-lived parent particles often behave similar in different superWIMP scenarios, differentiating observationally between *e.g.* gravitinos and hidden $U(1)_X$ gauginos could finally be possible by a careful study of the kinematics and the angular distribution of the initial and final state particles [40].

In superWIMP scenarios the parent particles typically have lifetimes in the range seconds to hours. These lifetimes are related to Planck-scale suppressed dimension-five operators in case of the gravitino, and to mixing parameters in the range $\chi \sim 10^{-15}$–10^{-11} in case of the hidden $U(1)_X$ gauginos. However, for much smaller couplings, the parent particles could become so long-lived, with lifetimes well beyond the age of the Universe, that they can actually by themselves constitute a viable, though slowly decaying, dark matter candidate. Examples of models where dark matter decays are again the hidden $U(1)_X$ gauginos, but with exponentially suppressed mixing parameters that are much smaller than in the above superWIMP case, and gravitino dark matter with a small R-parity violation (where the "parent particle" is actually the gravitino itself, its decay into Standard Model particles being double suppressed by the Planck-mass and a tiny R-parity violation) [41]. But in principle most models with stable dark matter particles become models for decaying dark matter if higher dimensional operators, which violate

the stabilizing symmetries, are taken into account [42, 43]. One concrete example of this kind is hidden $SU(2)$ vector dark matter [44], where the stabilizing custodial symmetry can be violated by dimension-six operators. If these operators are suppressed by masses around *e.g.* the GUT (*Grand Unified Theory*) scale, this induces the decay of the vector dark matter particles with lifetimes orders of magnitude longer than the lifetime of the Universe [45].

The decay of dark matter can affect cosmology in different ways, and in addition to the discussion of observational prospects it is possible to derive a number of constraints on the lifetime and decay channels from observations of CMB, LSS, supernovae (SNs) and cosmic rays.[1] The weakest of the possible constraints on the lifetime of dark matter holds if its decay products are invisible to Standard Model particles, as can happen when the decay resides completely in a hidden sector. In this case dark matter decay can only affect the expansion history of the Universe, leaving its imprints on *e.g.* CMB anisotropies and SN redshifts. Corresponding lower bounds on the dark matter lifetime are relatively weak and only an order of magnitude beyond the lifetime of the Universe [46, 47]. However, around a billion times stronger bounds on the lifetime hold in the generic case where the decay products include Standard Model particles, since they could show up as exotic contributions to the cosmic-ray fluxes, see *e.g.* Refs. [41–43, 48, 49], making decaying dark matter accessible to indirect dark matter searches. This is similar to WIMP dark matter, where the ongoing annihilation process is a source of high-energetic particles [50–53]. Although the decay/annihilation channels of concrete dark matter models can be very similar, decaying and annihilating dark matter scenarios differ in their emission profiles: Annihilation processes are proportional to the square of the local dark matter density, whereas decay processes simply scale linearly. This fact makes predictions from decaying dark matter quite robust, since in contrast to annihilation signals they do not depend on the details of the dark matter distribution on very small (sub-halo) scales [53, 54]. The differences in the emission profile have strongest impact on cosmic-ray channels that are sensitive to the spatial distribution of the sources, namely gamma rays and neutrinos, and imply different optimal search strategies for decaying and annihilating dark matter.

[1] Note that the term *cosmic rays* will be used for high-energetic nuclei, electrons and positrons as well as gamma rays throughout this work.

In the 1990s EGRET (*Energetic Gamma Ray Experiment Telescope*) performed a full-sky observation of gamma rays with energies up to around 10 GeV.[2] Apart from different resolvable point sources [55] the skymap showed a strong diffuse component [56, 57]. Concerning astrophysical sources, this diffuse gamma-ray flux is expected to split up into an anisotropic Galactic component, which is strongest by far in the region of the Galactic disk [56], and an isotropic extragalactic component, which can dominate the overall gamma-ray flux only in the region of the Galactic poles [58, 59]. The diffuse Galactic flux (or "galactic foreground") is known to come from interaction between cosmic rays and the interstellar radiation field (ISRF, made up of starlight, dust radiation and CMB) or, respectively, with the interstellar medium (ISM, mainly hydrogen and helium) [60]. Interactions between high-energetic electrons and the ISRF lead to inverse Compton scattering (ICS) radiation, interactions between electrons and the ISM to Bremsstrahlung radiation. Furthermore, spallation processes between the ISM and high-energetic cosmic-ray nuclei produce π^0s, whose subsequent decay into gamma-ray pairs also accounts for a large part of the observed Galactic foreground. On the other hand, the diffuse extragalactic flux (usually denoted "extragalactic gamma-ray background", EGBG), is expected to come mainly from unresolved point sources like active galactic nuclei [61].

Dark matter could generate an exotic gamma-ray component in two different ways: Firstly, the decay or annihilation of dark matter could produce prompt radiation, like final-state radiation or radiation from fragmentation of gauge or Higgs bosons. This component should be best seen at high Galactic latitudes around the pole region in the case of decay [41], and typically in the Galactic center region in the case of annihilation [62]. It is well know that for this reason gamma rays from decaying dark matter could be easily misidentified as contribution to the EGBG. Exotic contributions to the EGBG are expected to show then up in the EGBG energy spectrum as a deviation from a simple power law [41], the power law being the naive expectation for generic astrophysical backgrounds. Secondly, dark matter could produce electrons and positrons, whose subsequent inverse Compton scattering on photons in and outside of the Galaxy would generate another gamma-ray component [63–69]. Unfortunately, this component depends strongly on the details of the diffusive motion of cosmic rays inside the Galaxy, a mechanism

[2] See `http://heasarc.nasa.gov/docs/cgro/egret/egret_doc.html` for more details and data access.

that is qualitatively understood but has many free parameters. In case of decaying dark matter and standard diffusion models the corresponding radiation is often expected to dominate at regions close above and below the Galactic center, yielding a component that does not contribute to the apparent EGBG (although exceptions exist, see discussion in Ref. [70]). Since June 2008, the gamma-ray sky is being observed by the Fermi LAT (*Large Area Telescope*) [71], up to energies of 300 GeV and with an unprecedented precision. Although a full-sky map of the diffuse gamma rays is not yet officially released, preliminary data as well as publicly accessible photon event data have already been used to constrain and search for dark matter signals [70, 72–74].

During the propagation of charged cosmic rays (like electrons, positrons and antiprotons) from their sources to Earth most directional information is lost due to their diffusive motion through the tangled Galactic magnetic field, and the observed fluxes are expected to be mainly isotropic. Apart from that, most experiments, measuring *e.g.* electron and positron fluxes, do not measure these fluxes separately, but instead give, for technical reasons, results for the positron fraction of the overall signal (*e.g.* PAMELA [75], although also results for the absolute fluxes are announced), or the absolute electron plus positron flux (*e.g.* Fermi LAT [76]). The astrophysical expectations for the electron and positron fluxes follow in general from phenomenological models that describe the production and diffusive motion of cosmic rays in the Galaxy, possibly also including reacceleration and convection effects [60, 77, 78]. From these models the general expectation is that the positron fraction should decrease with energy, since the electron flux is mostly due to primary electrons, which have a hard spectrum and stem from primary sources like supernovae remnants, whereas the purely secondary positron flux has a softer spectrum and comes from spallation processes between cosmic-ray nuclei and the ISM.

Dark matter decay or annihilation is generically expected to produce equal amounts of electrons and positrons, often with very hard spectra, which in principle could be observed as a rise in the positron fraction to values up to 0.5. At the same time, a corresponding deviation from a simple power law is expected to be observed in the total electron plus positron flux. Predictions for the electron and positron fluxes as observable on Earth are very similar for decaying and annihilating dark matter scenarios, since only local sources with distances around a few kpc contribute to the fluxes in vicinity of the Earth (see *e.g.* Ref. [79]), and on these scales differences in the emis-

sion profile are not too relevant. Most interestingly, a rise in the positron fraction at energies above 10 GeV, measured up to energies around 100 GeV by PAMELA [75], and deviations from a simple power-law in the electron plus positron flux as measured by Fermi LAT [76] and HESS [80, 81] up to energies around 5 TeV, are indeed what is observed by the current instruments. These recent observations triggered a lot of excitement in the particle physicists community and were interpreted in terms of a large number of different decaying [21, 43, 48, 49, 82–102] and annihilating [103–111] dark matter models. Furthermore, the fact that at the same time no excess beyond the astrophysical expectations is observed in the antiproton channel [112] up to 100 GeV has allowed stringent constraints to be put on the viable dark matter models that can explain the excess. However, one has to bear in mind that much less exotic astrophysical primary sources of high-energetic positrons and electrons are known to exist: It was shown that, for appropriate model parameters, local pulsars could also well explain the current observations [113–121]. Nevertheless, the question of whether the observed fluxes are due to pulsars or to dark matter is not settled yet, although dark matter interpretations are already strongly constrained by gamma-ray and antiproton observations [49, 54, 63, 83, 109, 122], and are currently further tested by Fermi LAT.

The aim of this work is twofold: Firstly, we will discuss in detail the phenomenological aspects of a hidden $U(1)_X$ extension of the MSSM, concentrating on the case where the $U(1)_X$ mixes kinetically with hypercharge, remains unbroken at low energies and where no light matter states charged under $U(1)_X$ exist. This scenario is intriguing because of its simplicity on the one hand, and because it is well motivated in many string theoretic extensions of the Standard Model, including heterotic [123–125] and type II strings [126–129], on the other hand. However, its phenomenological prospects had not been worked out in the literature. Although Z' extensions of the Standard Model [130–135] and the MSSM [136–138] were studied, the case where the additional gauge group simply remains unbroken did not receive much attention until very recently [129, 139]. We will shortly discuss some theoretical aspects of the model, like the typical sizes of the kinetic mixing parameter and the gaugino mass in different theoretical frameworks, as well as the renormalization group equations that govern the evolution of these parameters. Then we will work out the relevant cosmological constraints from BBN, LSS and thermal overproduction that hold for this exemplary superWIMP

model, concentrating on the most common spectra where the hidden gaugino is the LSP and either a bino or a stau constitute the NLSP, with mixing parameters $\chi \gtrsim 10^{-16}$ (see also Ref. [20]). We will also discuss the intriguing case where the gravitino is the LSP, and the hidden gaugino the NLSP. In this case we have actually two superWIMP particles, and it turns out that their interplay allows to considerably weaken upper bounds on the reheating temperature that hold for standard gravitino dark matter scenarios [39]. These bounds are usually in general conflict with leptogenesis [140–142], an attractive mechanism for the generation of the observed baryon asymmetry. Finally, as already mentioned above, for very small mixing parameters $\chi \sim \mathcal{O}(10^{-24})$ (and without a light gravitino in the spectrum) the lifetime of the NLSP, which can be the hidden gaugino or the neutralino, becomes so long that the NLSP constitutes a decaying dark matter candidate. We will work out the cosmic-ray predictions of this model, calculating all the relevant branching ratios for a reference mSUGRA model as well as for more general cases. We will compare the resulting cosmic-ray predictions with current observations, concentrating on electrons/positrons, gamma rays and antiprotons (see also Ref. [21]).

Secondly, we will work out the cosmic-ray signatures of decaying dark matter more generally, independently of a concrete particle-physics model. We will concentrate on the hypothesis that the positron excess as measured by PAMELA is due to dark matter decay. To this end we will consider some decay channels, assuming most of the time that the corresponding branching ratios are 100% for simplicity, and single out some channels that can well fit the data (see also Ref. [49]). In light of the large uncertainties related to the actual astrophysical electron and positron background, and in contrast to other recent work [48, 73, 74, 109], we do not attempt to fit the data with some kind of quantitative χ^2-fits, but we try to single out channels that qualitatively agree well with the observations for standard propagation models and standard astrophysical backgrounds. These reference channels are useful for dark matter model building and comparison with other cosmic-ray observations. For our reference channels we will later discuss the corresponding predictions for current gamma-ray observations by the Fermi LAT. More generally, as mentioned above, dark matter decay produces exotic gamma-ray fluxes coming from prompt and ICS radiation. The prompt component is known to be best seen at high Galactic latitudes, and can be misidentified as part of the EGBG. However, the prompt signal is not completely isotropic, due to the offset between the Galactic center and the Sun: The dark matter

flux is largest in direction of the Galactic center, and smallest in direction of the Galactic anti-center. This dipole-like anisotropy is well known for the case of annihilating dark matter [143], however, a thorough discussion of the analogous case for decaying dark matter scenarios was lacking in the literature. We calculated the size of this anisotropy, including prompt radiation coming from cosmological distances, and find that the anisotropy lies in the range 20%–30%, which is larger than the anisotropy predicted by standard models for the Galactic foreground. We discuss prospects for seeing such an anisotropy in the upcoming Fermi LAT data (see also Ref. [54]) based on theoretical assumptions for the Galactic foreground. Finally we will also shortly show the anisotropies of the overall flux as *observed* by Fermi LAT after one year, based on publicly available photon event data, and comment on them in light of possible dark matter contributions.

The rest of this work is organized as follows: In *chapter 2* we will discuss the very basics of the Cosmological Concordance Model and the Standard Model of particle physics, mainly to fix notations. We will shortly review the observational evidence for the existence of dark matter, discuss why dark matter forces us to go beyond the Standard Model, and summarize what is known about the properties of dark matter particles. In *chapter 3* we will then concentrate on three concrete classes of dark matter models. After first reviewing the standard WIMP scenario, we will discuss the motivation and phenomenology of superWIMP dark matter. As an important example we will work out in detail the phenomenology of a hidden $U(1)_X$ gaugino superWIMP, with emphasis on the cosmological bounds coming from BBN, LSS and overproduction arguments. We will then close with a discussion about motivation and phenomenological aspects of decaying dark matter models. In *chapter 4* we will concentrate on indirect searches for decaying dark matter. After reviewing the basics about cosmic-ray propagation inside the Galaxy, we will discuss the decaying dark matter interpretation of the positron excess observed by PAMELA, and single out some reference decay channels that are in agreement with the observations. Afterwards, we will also discuss the typical cosmic-ray signatures of different scenarios with hidden $U(1)_X$ gauginos and extremely small mixing parameter as a concrete particle-physics example. Finally we will discuss the gamma-ray predictions of decaying dark matter, with emphasis on our above reference channels that we found to well fit the observed positron and electron data. We will analyze the dipole-like anisotropy of prompt gamma rays from decaying dark mat-

ter, which can be used to distinguish the dark matter component from the EGBG, in light of the upcoming Fermi LAT gamma-ray data, and based on theoretical foreground expectations as well as on preliminary and publicly available Fermi LAT data. Finally, in *chapter 5*, we conclude and give an outlook. Furthermore, in *appendix A* we outline some technical details about the calculations related to hidden $U(1)_X$ gauginos. In *appendix B* we shortly discuss the statistical errors of the dipole-like anisotropy.

Parts of the work presented in this thesis were published in peer-reviewed journals, namely section 3.3 in Ref. [20], section 4.2.2 in Ref. [49], section 4.2.3 in Ref. [21] and section 4.3 in Ref. [54].

Chapter 2

Observation of Dark Matter

Our current description of the physical world relies on two theories, which have both been confirmed to remarkable precision: The *Standard Model* of particle physics, which unites three of the four known fundamental forces into the framework of quantum field theory, and which accurately describes particle-physics experiments down to distances of $\mathcal{O}(10^{-18}\,\mathrm{m})$; and General Relativity together with the ΛCDM cosmological model (the current cosmological *Concordance Model*), which describes the history of the Universe between around $\mathcal{O}(10^{-12}\,\mathrm{s})$ after the Big Bang, when electroweak symmetry breaking took place, and up to length scales of the current particle horizon around 15 Gpc.

The Concordance Model includes a non-zero cosmological constant Λ, usually referred to as *Dark Energy*, as well as a large amount of *Cold Dark Matter*. These two ingredients do not have a proper counterpart in the Standard Model, but turn out to dominate today's energy budget of the Universe. Whereas dark energy can be in principle simply parametrized as a cosmological constant in the field equations of general relativity (although also dynamical models [144] with potentially very exotic observable effects exist [145, 146]), dark matter most probably requires the introduction of a new particle to the particle zoo of the Standard Model. In this chapter, we will give a short overview over the evidence and properties of dark matter. Exhaustive reviews can be found in Refs. [1, 3]. Theoretical candidates for particle dark matter will be discussed later in chapter 3 (SUSY dark matter candidates are reviewed in Refs. [2, 147], furthermore see Ref. [6]).

Below we will firstly discuss the very basics of General Relativity in 2.1, mainly to fix notations, then the observational evidence for dark matter

in 2.2, give a short summary of the Standard Model of particle physics in 2.3, and end with a collection of particle dark matter properties in 2.4.

2.1 Basics of General Relativity

In 1915 A. Einstein presented the field equations of General Relativity, which incorporate gravity into the framework of special relativity. These equations turned out to describe the observed Universe with great accuracy and are by now the basis of any cosmological study. To fix notations we shortly give an overview of the equations that are most relevant for this work (for a good introduction to standard cosmology see Refs. [5, 30, 148, 149]).

The Einstein equations read

$$R_{\mu\nu} - \frac{1}{2} g_{\mu\nu} R = \frac{8\pi G_N}{c^4} T_{\mu\nu} + \Lambda g_{\mu\nu} \ , \tag{2.1}$$

where $g_{\mu\nu}$ is the metric tensor, R and $R_{\mu\nu}$ are, respectively, the Ricci scalar and Ricci tensor, G_N is Newton's constant, $T_{\mu\nu}$ denotes the energy-momentum tensor, and Λ is the cosmological constant. For describing the physics of the Universe one commonly considers the most general metric consistent with isotropy and homogeneity. It can be shown that this metric is of the Robertson-Walker (RW) form [148], as given by

$$ds^2 = c^2 dt^2 - a(t)^2 \left(\frac{dr^2}{1 - kr^2} + r^2 \left(d\theta^2 + \sin^2 \theta d\phi^2 \right) \right) \ . \tag{2.2}$$

Depending on the value of k, the RW metric describes a closed ($k = 1$), flat ($k = 0$) or open ($k = -1$) geometry of the Universe. Apart from that, the metric only depends on one free function, the *scale factor* $a(t)$.

The matter and energy content of the Universe can be approximated by the energy momentum tensor of a perfect fluid,

$$T_{\mu\nu} = \sum_i \mathrm{diag}(\rho_i, p_i, p_i, p_i)_{\mu\nu} \ . \tag{2.3}$$

Here, ρ_i and p_i denote, respectively, the energy and pressure of the different energy or matter components i that are present in the Universe. With these assumptions, one can derive the two independent Friedmann equations

$$H^2 \equiv \left(\frac{\dot{a}}{a} \right)^2 = \frac{8\pi G_N}{3} \sum_i \rho_i - \frac{k}{a^2} \ , \tag{2.4}$$

and

$$\frac{\ddot{a}}{a} = -\frac{4\pi G_N}{3} \sum_i \left(\rho_i + 3\frac{p_i}{c^2}\right) \ . \tag{2.5}$$

For convenience we have defined the *Hubble expansion rate* H, which is a function of the scale factor and parameterizes the expansion velocity of the Universe. The cosmological constant is here interpreted as additional energy component, with $\rho_\Lambda = -p_\Lambda = c^4/8\pi G_N \cdot \Lambda$.

The *critical density* of the Universe, which denotes the overall energy density in a Universe with a flat ($k = 0$) geometry, is now given by $\rho_c \equiv 3H^2/8\pi G_N$. Note that the two Friedmann equations imply the conservation of the energy momentum tensor, $\nabla_\mu T^{\mu\nu} = 0$. This in turn yields the equation

$$\dot{\rho} + 3H(\rho + p) = 0 \ , \tag{2.6}$$

which holds for the different ρ_i and p_i separately if the corresponding components do not interact directly. In general, ρ_i and p_i are related by the equation of state $p_i = w_i \rho_i$, with $w_i = 1/3$ for radiation and relativistic gas, $w_i = 0$ for non-relativistic matter and dust, and $w_i = -1$ for the cosmological constant.

Taking into account a radiation component ρ_R, a pressureless matter component ρ_M and the cosmological constant ρ_Λ, one can show that the Hubble expansion rate as function of redshift z is given by the simple expression

$$H(z) = H_0 \sqrt{\Omega_M (1+z)^3 + \Omega_R (1+z)^4 + \Omega_\Lambda + \Omega_K (1+z)^2} \ , \tag{2.7}$$

where we make use of the dimensionless energy densities $\Omega_i \equiv \rho_i/\rho_c$, and we defined $\Omega_K \equiv -k/(a_0 H_0)^2$. The redshift z is related to the scale factor a via $z(t) + 1 = a_0/a(t)$, where a_0 denotes the scale factor today, and H_0 denotes today's Hubble expansion rate. Subsequently we will assume a flat geometry, $k = \Omega_K = 0$, unless states otherwise. Furthermore we will mostly use natural units with $c = \hbar = k_B = 1$.

2.2 Gravitational Evidence for the Existence of Dark Matter

The very first evidence for the existence of what we know today as dark matter came from observations of the Coma Cluster. In 1933 Fritz Zwicky

deduced from an application of the virial theorem to the velocity dispersion of galaxies in this cluster that its mass must be dominated by unseen matter [7]. The observed velocities were much too large to explain the stability of the cluster with the gravitational attraction of the observed matter alone, and he inferred that at least 400 times more matter was required. His suggestion of a missing *dark matter* component did not attracting much attention until another observation took place about 40 years later. Around 1970 Vera Rubin worked on spectroscopical measurements of the rotation curves of stars in edge-on spiral galaxies (see *e.g.* Ref. [8]). She found that the velocity of stars stayed practically constant at large enough distances from the galactic center, in contrast to the expectations from the observed luminous matter. This again suggested the existence of a dark matter component capable of holding the stars together despite their large orbital velocities. Both, Zwicky's and Rubin's work was later confirmed by many other types of observations, and today the existence of dark matter is widely accepted in the scientific community (for reviews see Ref. [1, 3–5, 150]).

Rotation curves of many spiral galaxies are by now well measured. One typical example, with rotational velocities becoming constant at radii above a few kpc, is shown in Fig. 2.1 (taken from Ref. [151], where also many other examples can be found). Applying the laws of Newtonian gravity, and assuming that the dominant part of the mass is spherically distributed, this implies a matter density profile that scales like $\rho(r) \sim r^{-2}$ with the distance r from the galactic center. This cannot be understood from galactic gas and stars alone (see dashed and dotted lines of Fig. 2.1). Additional support for the requirement of dark matter on galactic scales comes from different observations, *e.g.* the measurements of the velocity dispersions of stars inside of dwarf elliptic galaxies in the Local Group, which are again larger than expected by the luminous matter alone [151, 152].

On the scale of galaxy clusters, the measurements of peculiar velocities of galaxies, as done by F. Zwicky, were later supplemented by complementary measurements of X-ray emission of intracluster gas and by weak gravitational lensing.

The gas inside of a galaxy cluster, the intracluster medium (ICM), is usually heated up during cluster formation by transforming gravitational into kinetic energy. The temperature of the hot ICM, typically of the order of $T \approx 10\,\mathrm{keV}$, can be measured by means of X-ray observations and gives indi-

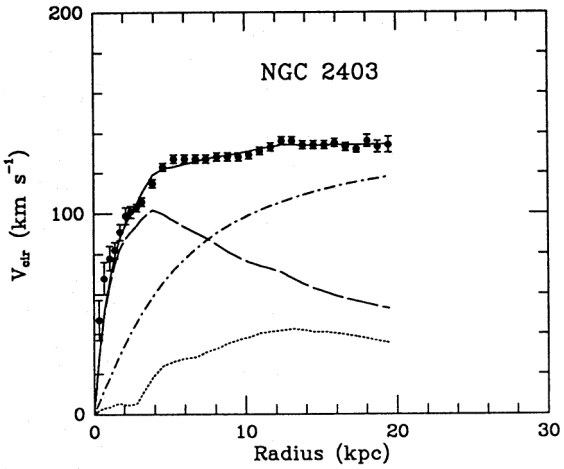

Figure 2.1: Rotation curve of NGC 6503 from Ref. [151]. The lines show the theoretical expectations from the visible component (*dashed*), the gas (*dotted*) and the fitted dark matter component (*dash-dotted*) alone, and the expectation for their sum (*solid*).

rect information about the mass of the cluster. Weak gravitational lensing, on the other hand, is a method purely based on Einstein's theory of general relativity: The images of distant galaxies are distorted by the gravitational potentials the light traverses before reaching the Earth. A statistical analysis of the distortion of a large numbers of background galaxies allows a determination of the distribution of gravitating matter lying on the line-of-sight, and hence again an indirect detection of the mass of galaxy clusters. All three types of observations, peculiar velocities, gas emission and weak gravitational lensing, turn out to support the existence of around $\Omega_M \simeq 0.2 - 0.3$ dark matter in the Universe (for details about X-ray measurements see below, see also Ref. [3]).

A spectacular observation of dark matter in a cluster merger was made in 2006, and is shown in Fig. 2.2. Due to the collision of the two galaxy clusters inside the cluster merger, the collisionless stellar component and the interacting hot ICM, as measured by X-ray observations, are spatially separated. Although the dominant part of the baryonic matter is inside the gas, gravitational lensing proved that the dominant part of the gravitating matter is actually following the stellar component, being hence spatially separated from the baryons. This is exactly what is expected if the dominant

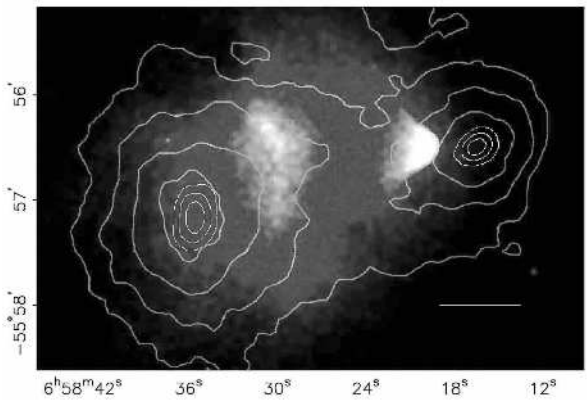

Figure 2.2: Observations of the *bullet cluster*, from Ref. [153]. The lines show the distribution of gravitating mass as inferred from weak gravitational lensing, the shaded areas show X-ray observations from Chandra, which trace the distribution of the ICM.

part of matter of the galaxy clusters resides in collisionless dark matter particles, whereas this behavior would be difficult to understand in models with modified Newton dynamics (MOND [154], see also discussion in Refs. [4, 5]).

The most precise determination of the overall size of the dark matter content of the Universe comes from observations on cosmological scales, namely the observation of SNs, the LSS of luminous and non-luminous matter and the angular anisotropies of the CMB (for recent reviews see Refs. [1, 3, 5]). Furthermore, a very important measure for the baryon density of the Universe is provided by BBN. Below we will shortly summarize the most important aspects of how to measure the different energy components in the Universe, namely the dark energy density Ω_Λ, the total matter density Ω_M, the baryon density, Ω_b, and the density of non-baryonic dark matter, $\Omega_{\rm DM} \equiv \Omega_M - \Omega_b$. The total energy density of the Universe is in our case just given by $\Omega_{\rm tot} = \Omega_M + \Omega_\Lambda$.[1]

Big Bang Nucleosynthesis allows a precise determination of the baryon density Ω_b. This is because the baryon density directly influences the interac-

[1]Relativistic particles are negligible in the energy budget of today's Universe. Photons only contribute $\Omega_\gamma h^2 = 2.480 \times 10^{-5}$, massless neutrinos would have similar energy densities. Massive neutrinos can in principle contribute to Ω_M, but are constituting hot dark matter, which is observationally problematic, see below.

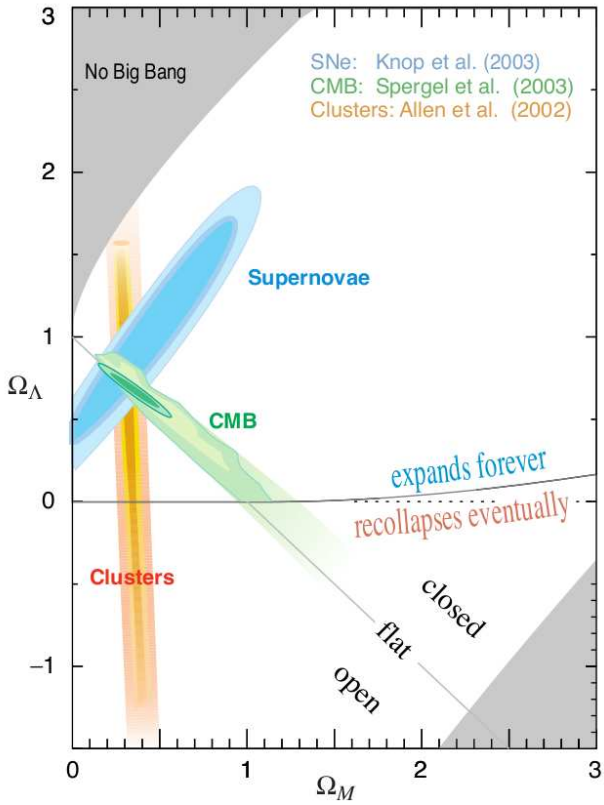

Figure 2.3: Compilation of different bounds on the preferred region in the Ω_m–Ω_Λ plane (from Ref. [1, section 21]). Shown are bounds from X-ray observations of galaxy clusters, from WMAP observations of the CMB angular anisotropies and from observations of Supernovae.

tion rate, and hence also the final abundances, of the elements formed during BBN (mainly D, ^{3}He, ^{4}He and ^{7}Li). In particular deuterium turns out to give powerful constraints. Current observations yield $0.017 \leq \Omega_b h^2 \leq 0.024$ (95% CL) [1, section 20].

Supernovae of type Ia are well known to be excellent standard candles for measuring distances in the Universe. Their peak luminosity during their explosion is well enough understood to use the observed flux as a measure for their luminous distance from our Galaxy. Together with a determination of the redshifts z of the observed supernovae, one can use the resulting luminosity-distance – redshift relations to put constraints on the time-evolution of the Hubble expansion rate, which in turn gives constraints on

the matter and radiation content of the Universe. In 1998 the first observational evidence was published that today's Universe is actually dominated by an energy component that can be well described by a non-zero cosmological constant [155–157]. Constraints on the Ω_M – Ω_Λ parameter space, coming from observations of type Ia supernovae, are shown in Fig. 2.3.

The observed angular power spectrum of the CMB allows a direct determination of the geometry of the Universe, since the position of the first acoustic peak provides a measure of the overall energy content of the Universe [4]. Hence, the CMB power spectrum can strongly constrain the sum $\Omega_\Lambda + \Omega_M$, and actual observations by WMAP [158] and older experiments [4] strongly favor values around one, consistent with a flat Universe, as shown in Fig. 2.3.

Finally, observations of rich galaxy clusters on $\mathcal{O}(10\,\mathrm{Mpc})$ scales allow a determination of the baryon-gas to mass fraction inside these clusters. As mentioned above, measurements of the X-ray emission of the ICM can be used to infer both, the overall mass of the cluster, which impacts on the temperature of the gas, as well as the gas density, which determines its emissivity. Since most baryons inside galaxy clusters actually reside in the ICM, and since one can assume that the matter composition of rich galaxy clusters provide a fair estimate for the matter composition on cosmological scales, the baryon-gas to mass fraction is actually a good measure for the overall fraction of baryonic matter to total matter in the Universe. Together with the determination of Ω_b from BBN, this yields constraints on the matter density around $\Omega_M \simeq 0.3$, as again shown in Fig. 2.3 [159] (see also Ref. [4]).

The most precise determination of the different cosmological parameters is actually obtained by global analyses that beside the CMB anisotropies also include LSS and supernovae data. However, the exact values of the resulting parameters depend on the priors and on the data sets included, and throughout this work we will for definiteness assume a ΛCDM cosmology with parameters $\Omega_\Lambda = 0.74$, $\Omega_M = 0.26$, $\Omega_{\mathrm{DM}} = 0.21$ and $h = 0.72$, as derived from the five-year WMAP data alone [160].

Particle	$\begin{pmatrix}\nu_L\\ e_L\end{pmatrix}$	$e_R^\dagger$	$\begin{pmatrix}u_L\\ d_L\end{pmatrix}$	$u_R^\dagger$	$d_R^\dagger$	$\begin{pmatrix}H_1\\ H_2\end{pmatrix}$
Spin	$1/2$	$1/2$	$1/2$	$1/2$	$1/2$	0
Charge	$(\mathbf{1},\mathbf{2})_{-1/2}$	$(\mathbf{1},\mathbf{1})_1$	$(\mathbf{3},\mathbf{2})_{1/6}$	$(\bar{\mathbf{3}},\mathbf{1})_{-2/3}$	$(\bar{\mathbf{3}},\mathbf{1})_{1/3}$	$(\mathbf{1},\mathbf{2})_{-1/2}$

Table 2.1: Summary of the spin-0 and spin-$1/2$ particles of the Standard Model and their gauge group representations. In case of the spin-$1/2$ particles, family indices for the three observed fermion generations are suppressed. Group representations are given in the form $(SU(3)_c, SU(2)_L)_Y$. Furthermore the Standard Model contains 12 spin-1 gauge bosons.

2.3 The Standard Model and Beyond

The Standard Model of particle physics, as pioneered in 1961–1968 by S. L. Glashow, S. Weinberg and A. Salam [161–163][2] is based on the gauge group pattern

$$SU(3)_c \otimes SU(2)_L \otimes U(1)_Y \to SU(3)_c \otimes U(1)_{\text{em}} \ ,$$

where electroweak sector $SU(2)_L \otimes U(1)_Y$ breaks as indicated to the electromagnetic $U(1)_{\text{em}}$. The particle content of the Standard Model is shown in Tab. 2.1: Apart from the 12 vector bosons associated with the three gauge groups, the standard model contains 9 leptonic fermions (counting two-spinors), 36 baryonic fermions, and as the Higgs sector 2 complex scalars. For review articles about the Standard Model see Refs. [1, 164, 165].

The only stable particles in the Standard Model are the electron (which is the lightest particle carrying lepton number), the photon (since it is massless), the neutrinos (also massless in the Standard Model) and the proton (the lightest particle carrying baryon number). The neutron with a lifetime around 15 min is very long-lived compared to the other particles and can be stable when bounded to atomic nuclei. As will be discussed in section 2.4, neutrinos cannot be dark matter, since they would be too hot. However, as discussed above, observations on cosmological scales also imply that $\Omega_b \ll \Omega_M$, which strongly suggests that the missing dark matter can

[2] This only concerns the electroweak theory, strong interactions were later worked out by a larger number of people around 1973–1974.

neither be baryonic [5]. If all matter of the Universe would be inside of baryons, the growth of structures before recombination (taking place around 400 000 years after Big Bang) would be strongly suppressed, in contrast to what is observed in the LSS and the CMB anisotropies. On galactic scales, microlensing searches for MACHOs as candidates of non-luminous baryonic matter in galaxies yield upper bounds on the dark matter fraction that could be due to MACHOs, ranging from 8% to 40%, and strengthening the need for non-baryonic dark matter [1, section 22].

If dark matter is explained by an additional non-baryonic component, this component requires an extension of the Standard Model. Well known examples are the lightest supersymmetric particle in R-parity conserving supersymmetric extensions of the Standard Model, the axion, or the lightest Kaluza-Klein mode in models with extra-dimensions [2, 3, 6]. Some of these candidates will be discussed in more detail in chapter 3.

2.4 Properties of Particle Dark Matter

An instructive overview of current constraints on particle dark matter properties can be found in Ref. [150]. The most common requirements for dark matter particles are that they should be *cold* and *neutral*. Furthermore, any theory of dark matter that aims to yield a consistent thermal history of the Universe should explain the observed dark matter relic density and not spoil primordial nucleosynthesis. On top of that, there exists a large number of results from indirect and direct dark matter searches, and a promising model should be in reach of this or other non-gravitational observations.

Hot dark matter (HDM) is relativistic during structure formation, and it tends to damp primordial density fluctuations below its free-streaming length. This is an effect similar to Silk damping, which is caused by free-streaming photons during the epoch of recombination [150]. Classical examples for hot dark matter candidates are massive neutrinos. For neutrino masses in the eV regime their free-streaming length is of the order of the size of superclusters. Hot dark matter predicts a top-down hierarchy of structure formation, with small structures being produced in the fragmentation of larger structures. This is in contrast to observations of galaxies older than superclusters. However, small amounts of hot dark matter are allowed by current observations. In particular observations of the Lyman-α forest

give strong bounds on the fraction of dark matter that is allowed to be hot, which can be expressed as an upper bound on the sum of the neutrino masses. Depending on the data sets included the 2σ-bounds can range from $\sum m_\nu \leq 0.17\,\mathrm{eV}$ (for all data sets, including Lyman-α) to $\sum m_\nu \leq 2.3\,\mathrm{eV}$ (for WMAP data only), see Refs. [166–168].

On the other hand, *cold dark matter* (CDM) is non-relativistic during structure formation and allows clumping even on small scales. The best predictions for the behavior of cold dark matter models come from N-body simulations, which are in general in good agreement with the observed large scale structures, like cluster abundance and galaxy-galaxy correlation functions, see *e.g.* Ref. [169]. However, there are also discrepancies with the observations, namely the "missing satellite" problem [37] and the predictions of cuspy halo profiles, which are not observed in low surface brightness galaxies [150]. Although these problems could be *e.g.* due to current technical limitations of N-body simulations, these discrepancies have also motivated consideration of alternatives to the cold dark matter paradigm, in particular models where dark matter is warm.

Dark matter with velocity dispersions between hot and cold dark matter is denoted *warm dark matter* (WDM). Prototypical examples are very light gravitinos and sterile neutrinos. Strongest upper bounds on the thermal velocity, or respectively, the free-streaming length of the particles, are again obtained when observations of the Lyman-α forest are taken into account, coming *e.g.* from an analysis of high-redshift quasar spectra from the *Sloan Digital Sky Survey* (SDSS) [32]. These bounds are typically expressed as lower bounds on the mass of sterile neutrinos, m_s, but can also be translated into constraints on the free-streaming length and superWIMP scenarios (see below). Current limits range between $m_s \gtrsim 10\,\mathrm{keV}$ (2σ) [35] and $m_s \gtrsim 14\,\mathrm{keV}$ (2σ) [36], see also Refs. [170, 171] for detailed discussions.

Other important bounds, for instance on charged or milli-charged dark matter, on strongly interacting dark matter and on self-interacting dark matter are summarized in Ref. [150].

Chapter 3

Models for Particle Dark Matter

Many theoretical models for dark matter have been proposed. In particular models where dark matter couples weaker than electroweak to the Standard Model sector often predict spectacular signals in cosmology and at colliders. In this chapter we will firstly review very shortly the common WIMP dark matter models in section 3.1, and secondly superWIMP dark matter scenarios and their typical cosmological implications in section 3.2. In section 3.3 we will work out in some detail the cosmological bounds of a superWIMP dark matter scenario with kinetically mixed hidden $U(1)_X$ gauginos. Finally, in section 3.4, we will motivate dark matter models where dark matter decays with cosmological lifetimes.

3.1 Weakly Interacting Massive Particles

The nowadays most popular class of dark matter models are the ones with *weakly interacting massive particles* (WIMPs). Their density today is due to thermal "freeze-out": After being in thermal equilibrium with the primordial plasma in the early Universe, they start to annihilate when they become non-relativistic (usually WIMPs are their own anti-particles). This annihilation process reduces the number of WIMP particles by a huge amount and stops when the particles are well in their non-relativistic regime, leaving only a tiny relic density of dark matter particles. For particles with $\mathcal{O}(100\,\mathrm{GeV})$ masses and electroweak cross-sections around $\langle\sigma v\rangle \sim \mathcal{O}(10^{-26}\,\mathrm{cm}^3\,\mathrm{s}^{-1})$ this leads to

a dark matter energy density that is in the ball-park of what is observed.

The evolution of the number density n of dark matter particles follows a simple Boltzmann equation [2, 3, 30]

$$\frac{dn}{dt} + 3Hn = -\langle\sigma v\rangle(n^2 - n_{\rm eq}^2) \ , \tag{3.1}$$

where $n_{\rm eq}$ is a function of temperature and denotes the number density of the particles in thermal equilibrium, $\langle\sigma v\rangle$ is the thermally averaged annihilation cross-section, and H is the Hubble expansion rate as function of time. Solving Eq. (3.1) one can calculate today's relic density for any self-annihilating particle. In particular, on can show [2, 3] that an order of magnitude estimate for the relic density is given by

$$\Omega_{\rm DM}h^2 \approx \frac{3\times 10^{-27}\,{\rm cm}^3\,{\rm s}^{-1}}{\langle\sigma v\rangle} \ . \tag{3.2}$$

The paradigmatic example for WIMP dark matter is the lightest neutralino of the MSSM (see Ref. [9] for an introduction) [2, 147]. Within the particle content of the MSSM, and over a large range of parameters, the LSP can be either the lightest neutralino, the lightest sneutrino or the lightest stau. Among these, only the lightest neutralino is still allowed by present experiments as a viable dark matter candidate [2, 3, 9, 172]. Note that, if supersymmetry is promoted to a local symmetry in scenarios of supergravity, the particle content of the MSSM is extended by the spin-$^3/_2$ gravitino, which is also a viable dark matter candidate [173], even if R-parity is slightly violated [39, 174]. Gravitino dark matter falls into the category of superWIMPs and will be discussed below in section 3.2.

In standard WIMP scenarios, the annihilation process that has lead to the observed relic density in the past is expected to produce today a possibly observable contribution to the measured cosmic-ray fluxes on Earth. A lot of effort has been made to study the prospects and predictions for this *indirect detection* of dark matter via its cosmic-ray signatures, namely in the gamma-ray, electron/positron and antiproton channels, see *e.g.* [50–53, 95, 122, 175–177]. Note that similar contributions to the cosmic-ray fluxes are expected if dark matter *decays* [82, 178–181]. The peculiar predictions of decaying dark matter will be discussed later in chapter 4.

3.2 SuperWIMPs

Many alternatives to the standard WIMP scenario do exist in the literature. These scenarios are motivated phenomenologically by short comings of the standard CDM models (*e.g.* warm dark matter), or theoretically by the many different possible extensions of the Standard Model (*e.g.* axions and gravitinos), leading to a zoo of dark matter models with very different implications for the different dark matter search experiments. One class of these models is known under the name *superWIMPs* [22]. The paradigmatic example is the gravitino [18, 19, 39, 40, 182–184].

SuperWIMPs are typically produced in the late decay of other particles, and their thermal production is in most cases negligible. In this case the relic density of a superWIMP X, which is produced in the decay of particle Y, is simply given by

$$\Omega_X = \frac{m_X}{m_Y}\Omega_Y \ , \tag{3.3}$$

where Ω_i and m_i denote, respectively, the relic density and the mass of the two considered particles. Hence, the superWIMP inherits in general the relic density of the parent particle. If the parent particle is *e.g.* a WIMP this can give quite naturally the correct relic density to the superWIMP particle, despite its very weak interaction with the visible world and its often tiny annihilation cross-section. As mentioned in section 1, typical collider signature of superWIMP scenarios are these parent particles, which are often quite long-lived and could lead to distinct signatures in the detector [39, 40].

If the decay of parent particles takes place during BBN, the hadronic and electromagnetic energy released in the decay can destroy the successful predictions of the standard BBN scenario [25, 185] (for more recent work see also Refs. [26, 27]). In cases where the decaying particle is electrically charged, it could additionally form bound states with ^{4}He and ^{8}Be, triggering the catalytic production of ^{6}Li and ^{9}Be [28, 29]. Catalytic enhancement of ^{6}Li and ^{9}Be production essentially requires that the lifetime of the charged particle $\tau_{\rm ch}$ is smaller than around $\tau_{\rm ch} \lesssim 2 \times 10^3\,$s [28], unless the density of parent particles is strongly suppressed. A good recent review about BBN bounds can be found in Ref. [24].

SuperWIMP particles are potentially produced with a momentum that is large enough to wash out density fluctuations on small scales with impact on structure formation, similar to scenarios with warm dark matter (for a

discussion in the context of superWIMPs see Ref. [31]). The impact on structure formation can be encoded in the free-streaming length $\lambda_{\rm FS}$, which we define as the comoving distance traveled by a particle since it was produced[1],

$$\lambda_{\rm FS} = \int_0^{z_p} dz \frac{v(z)}{H(z)} \,. \tag{3.4}$$

Here, z_p denotes the redshift at the moment of decay of the parent particle, and $v(z)$ and $H(z)$ are the redshift dependent velocity of the particle and the Hubble expansion rate, respectively. For practical purposes one can approximate z_p, which is in principle different for each individual particle, by $z_p = z(t = \tau_p)$, where τ_p is the lifetime of the parent particle. As discussed in section 2.4, in WDM scenarios and on scales below the free-streaming length of dark matter particles, density fluctuations become washed out before structure formation begins [30]. Current lower bounds on the sterile neutrino mass [35, 36] as inferred from the latest SDSS Lyman-α Forest data [32] can be translated into an upper bound on the free-streaming length of dark matter particles. This bound is roughly given by $\lambda_{\rm FS} \lesssim 0.5\,{\rm Mpc}$ [33, 34].

3.3 Hidden $U(1)_X$ Gauginos as SuperWIMPs

In this section we will study in detail the properties of a prototypic superWIMP dark matter candidate: The gaugino of a hidden $U(1)_X$ gauge group. We will assume that the only interaction with the MSSM is due to a tiny kinetic mixing with hypercharge, and we will concentrate on the case where this hidden $U(1)_X$ remains *unbroken* at low energies. After a theoretical motivation in subsection 3.3.1 and an introduction to the model in subsection 3.3.2, we will present different cosmological bounds on the parameter space and discuss phenomenological prospects in subsection 3.3.3. In subsection 3.3.4 we will finally discuss cases with extremely small kinetic mixing, which are connected to decaying dark matter. The corresponding cosmic-ray signals of this decaying dark matter scenario will be discussed in the next chapter in subsection 4.2.3.

The work presented in this section was published in Ref. [20].

[1]Note that the free-streaming length becomes typically around 10% smaller if one uses the redshift at matter-radiation equality, $z_{\rm EQ} \sim \mathcal{O}(3000)$, as a lower bound of the integral.

3.3.1 Motivation

Many extensions of the MSSM contemplate the possibility of a *hidden sector*, consisting of superfields which are singlets under the Standard Model gauge group. Hidden sector superfields usually couple very weakly to our observable sector, and thus constitute a natural arena for finding dark matter candidates. Generically, at low energies hidden sector particles couple to our observable sector only via non-renormalizable operators, presumably suppressed by a large mass scale, and with a structure that is strongly model dependent. Deriving implications on the thermal history of the Universe and for future collider experiments is thus hindered by our ignorance of the strength and the structure of these operators.

There are however three instances where the hidden sector particles can couple to the MSSM particles via *renormalizable* operators, which have a structure that is well defined by the Lorentz and gauge symmetries. Firstly, a hidden sector chiral superfield, S, could couple to the lepton and up-type Higgs doublet superfields via the Yukawa coupling SH_uL in the superpotential, or to the two MSSM Higgs doublets, via SH_uH_d, provided these terms are also invariant under the hidden sector gauge group (as well as possible discrete and global symmetries of the theory). Secondly, if one of the MSSM chiral superfields is charged under a hidden sector gauge group, it will interact with the corresponding hidden sector gauge superfield, and in turn with other hidden sector chiral superfields via the D-term. Finally, a hidden sector Abelian vector superfield, X, may couple to the hypercharge vector superfield through a kinetic mixing term, which is always allowed by the gauge symmetries [186, 187]. As mentioned above, we will here concentrate on the latter situation of kinetic mixing between hypercharge and a hidden sector $U(1)_X$ gauge group. The gauge group of our scenario is hence

$$SU(3)_c \otimes SU(2)_L \otimes \underbrace{U(1)_Y \otimes U(1)_X}_{\text{kinetically mixed}} \ .$$

Models with a hidden $U(1)_X$ extension of the SM or MSSM have been extensively studied in the literature (see *e.g.* Ref. [130], for a recent review see Ref. [134]). Some of these works take into account kinetic- and mass-mixing [131–133, 135–138], but it is typically assumed that the gauge symmetry of the additional $U(1)_X$ is broken by a Higgs or Stueckelberg mechanism.[2] In

[2]Exceptions are *e.g.* Ref. [188, 189], where constraints on, and consequences of, higher

this case, it is possible to derive bounds from high precision LEPI data if the hidden $U(1)_X$ gauge boson mass is large (namely, $\chi \lesssim 0.05$ for masses around 200 GeV [133]), and from different astronomical observations and laboratory experiments if the masses are small (namely, for *e.g.* masses around 100 eV, the observed lifetime of the Sun translates into a bound $\chi \lesssim 10^{-13}$ [128, 192]).

However, here we will study the special case where the hidden $U(1)_X$ gauge group remains *unbroken* at low energies. If this is the case, the corresponding hidden $U(1)_X$ gaugino λ_X will have in general a mass roughly comparable to the typical soft SUSY breaking masses of the observable sector particles, although the details depend on the actual mediation mechanism of SUSY breaking. In cases where it is the lightest among all supersymmetric particles, it can constitute superWIMP dark matter.

Our motivation for concentrating on unbroken hidden sector Abelian gauge groups is twofold: Firstly, in string theory compactifications hidden sector $U(1)$s are ubiquitous and some of them could remain unbroken at low energies, in complete analogy to the familiar electromagnetic $U(1)_{\rm em}$ of our observable sector. These hidden $U(1)$s can be *e.g.* realized as perturbative heterotic string states [123], as $U(1)$ gauge factors arising from space-time filling D-branes non-intersecting with the Standard Model D-branes in the extra dimensions of type-II string theories [127, 128], or as Ramond-Ramond (RR) forms under which these D-branes are charged [129]. Furthermore, in the "mini-landscape" of orbifold compactifications of the heterotic string [125] one encounters, at the compactification scale, a breaking of the gauge symmetry to a theory involving many hidden $U(1)$s, *e.g.* $\mathrm{E}_8 \times \mathrm{E}_8 \to \mathrm{G}_{\rm SM} \times \mathrm{U}(1)^4 \times [\mathrm{SO}(8) \times \mathrm{SU}(2) \times \mathrm{U}(1)^3]$ and the like. Some of these hidden $U(1)$s may remain unbroken down to very small scales [126].

Secondly, the case of a massless kinetically mixed unbroken hidden sector $U(1)_X$ is particularly intriguing, since in a non-supersymmetric world this situation is practically unconstrained by present experiments. Indeed, it was shown long ago by Holdom that in simple extensions of the Standard Model the kinetically mixed hidden $U(1)_X$ gauge boson $X_{\mu\nu}$ (the "paraphoton" [193]) completely decouples from the observable sector [194].

This decoupling of the unbroken hidden $U(1)_X$ gauge group can be gen-

dimensional operators that couple hidden and observable sector are studied. In Ref. [190] the authors study BBN and CMB constraints on the particle content of a completely decoupled hidden sector which may contain unbroken $U(1)$s. Furthermore, see Ref. [191] for a short discussion about gauge coupling unification in the presence of kinetic mixing.

eralized to unbroken supersymmetric theories. Let us consider the SUSY-invariant part of the Lagrangian,

$$\begin{aligned}\mathcal{L} &= \frac{1}{4}\int d^2\theta \left(\hat{W}_B^\alpha \hat{W}_{B\,\alpha} + \hat{W}_X^\alpha \hat{W}_{X\,\alpha} + 2\chi \hat{W}_B^\alpha \hat{W}_{X\,\alpha}\right) + \text{h.c.} + \\ &+ \int d^2\theta d^2\bar{\theta} \left(\Phi^\dagger e^{Y g_Y \hat{B}} \Phi + h^\dagger e^{q g_X \hat{X}} h\right) , \end{aligned} \tag{3.5}$$

where the field strength superfield is defined as $\hat{W}_V^\alpha = -\frac{1}{4}\bar{D}\bar{D}D^\alpha \hat{V}$, $\hat{V} = \hat{B}, \hat{X}$ being the hypercharge or the hidden $U(1)_X$ vector superfield, while Φ and h denote, respectively, any Standard Model or hidden sector chiral superfield (see Refs. [15, 195, 196] for introductions to the superfield formalism). Finally, χ is the kinetic mixing parameter, which is induced through quantum effects by chiral superfields charged under both gauge groups [123, 127, 128, 186, 197].

The gauge kinetic terms in Eq. (3.5) can be made canonical by introducing shifted vector superfields,

$$\begin{aligned} X &= \hat{X} + \chi \hat{B} , \\ B &= \sqrt{1-\chi^2}\hat{B} , \end{aligned} \tag{3.6}$$

leading to

$$\begin{aligned}\mathcal{L} &= \frac{1}{4}\int d^2\theta \, (W_B^\alpha W_{B\,\alpha} + W_X^\alpha W_{X\,\alpha}) + \text{h.c.} + \\ &+ \int d^2\theta d^2\bar{\theta} \left(\Phi^\dagger e^{Y g'_Y B} \Phi + h^\dagger e^{q g_X X - q g'_X B} h\right) , \end{aligned} \tag{3.7}$$

where $g'_Y = g_Y/\sqrt{1-\chi^2}$ and $g'_X = \chi g_X/\sqrt{1-\chi^2}$. Therefore, the canonical normalization of the kinetic terms produces an unobservable shift of the hypercharge gauge coupling and the generation of a "minihypercharge" for the hidden sector chiral superfields [186]. However, it can be read of from Eq. (3.7) that, as long as hidden sector matter h is absent or heavy enough to be phenomenologically irrelevant, the vector superfield X completely *decouples* from the visible sector and is not subject to any experimental constraint.[3]

[3]For scenarios *with* light hidden sector matter, different astrophysical observations and laboratory experiments constrain the possible values of the minihypercharge and the masses of the hidden sector particles. For instance, one obtains $\chi\, g_h/g_Y \lesssim 10^{-14}$, where g_h (g_Y) is the gauge coupling in the hidden (visible) sector, for masses below 10 keV from plasmon decay in red giants, see Ref. [128].

This situation is in particular motivated for RR $U(1)$ gauge groups in type-II string theory, where the only objects charged under these groups are non-perturbative D-brane states with masses at the string scale (for details see Ref. [129]), but it occurs generically always when all matter states charged under the hidden $U(1)_X$ are vector like and acquire large masses. Below we will concentrate on this particular situation and assume that no light matter states survive at low energies.[4]

In the next subsection we will show that the breaking of supersymmetry changes dramatically the previous picture: Although the hidden $U(1)_X$ gauge boson remains decoupled from the observable sector, kinetic mixing induces a *mass mixing* between the hidden $U(1)_X$ gaugino and the MSSM neutralinos that cannot be rotated away. In a large part of the parameter space, the hidden gaugino will then act as superWIMP dark matter.

3.3.2 Model and parameters

We will now briefly describe the model under consideration in the more familiar component formalism. In the Wess-Zumino gauge, a vector superfield can be expanded in component fields as $V = -\theta\sigma^\mu\bar{\theta}V_\mu + i\theta\theta\bar{\theta}\bar{\lambda} - i\bar{\theta}\bar{\theta}\theta\lambda + \frac{1}{2}\theta\theta\bar{\theta}\bar{\theta}D$. Then, the pure gauge part of Eq. (3.5), including supersymmetry breaking effects (the gaugino soft masses), reads

$$\begin{aligned}\mathcal{L}_{gauge} &= -\frac{1}{4}\begin{pmatrix}\hat{X}_{\mu\nu} & \hat{B}_{\mu\nu}\end{pmatrix}\mathcal{K}\begin{pmatrix}\hat{X}^{\mu\nu}\\ \hat{B}^{\mu\nu}\end{pmatrix} - i\begin{pmatrix}\hat{\lambda}_X & \hat{\lambda}_B\end{pmatrix}\mathcal{K}\sigma^\mu\partial_\mu\begin{pmatrix}\hat{\lambda}_X^\dagger\\ \hat{\lambda}_B^\dagger\end{pmatrix} \\ &\quad +\frac{1}{2}\begin{pmatrix}\hat{D}_X & \hat{D}_B\end{pmatrix}\mathcal{K}\begin{pmatrix}\hat{D}_X\\ \hat{D}_B\end{pmatrix} - \frac{1}{2}\left[\begin{pmatrix}\hat{\lambda}_X & \hat{\lambda}_B\end{pmatrix}\hat{\mathcal{M}}\begin{pmatrix}\hat{\lambda}_X\\ \hat{\lambda}_B\end{pmatrix} + \text{h.c.}\right],\end{aligned} \tag{3.8}$$

where $\mathcal{K}$ and $\hat{\mathcal{M}}$ denote, respectively, the kinetic and mass mixing matrices:

$$\mathcal{K} = \begin{pmatrix}1 & \chi\\ \chi & 1\end{pmatrix} \quad \text{and} \quad \hat{\mathcal{M}} = \begin{pmatrix}\hat{M}_X & \delta\hat{M}\\ \delta\hat{M} & \hat{M}_B\end{pmatrix}. \tag{3.9}$$

It is convenient to work in the basis where the kinetic terms are canonical, like also done above in Eq. (3.6). To this end, we will again redefine the vector

[4] However, we will include heavy hidden sector matter states in the below discussion about the running of masses and couplings.

superfields according to

$$\begin{pmatrix} \hat{X} \\ \hat{B} \end{pmatrix} = \begin{pmatrix} 1 & -\frac{\chi}{\sqrt{1-\chi^2}} \\ 0 & \frac{1}{\sqrt{1-\chi^2}} \end{pmatrix} \begin{pmatrix} X \\ B \end{pmatrix} . \tag{3.10}$$

As discussed above, the canonically normalized fields $X_{\mu\nu}$ and D_X completely decouple from the observable sector.[5] However, a mass mixing between the hidden gaugino and the bino remains in general. More precisely, in the basis where the kinetic terms are canonical, the extended neutralino (5×5) mass matrix reads, to lowest order in χ,

$$\mathcal{M}_{\mathrm{N}} = \begin{pmatrix} M_X & \delta M & 0 & 0 & 0 \\ \delta M & M_B & 0 & -M_Z c_\beta s_W & M_Z s_\beta s_W \\ 0 & 0 & M_W & M_Z c_\beta c_W & -M_Z s_\beta c_W \\ 0 & -M_Z c_\beta s_W & M_Z c_\beta c_W & 0 & -\mu \\ 0 & M_Z s_\beta s_W & -M_Z s_\beta c_W & -\mu & 0 \end{pmatrix} , \tag{3.11}$$

where, $\delta M = (\delta\hat{M} - \chi\hat{M}_X)/\sqrt{1-\chi^2}$, $M_X = \hat{M}_X$ and $M_B = \hat{M}_B + \mathcal{O}(\chi^2)$. Here, μ denotes the MSSM μ-term, M_Z the mass of the Z gauge boson, s_W the sine of the Weinberg angle and s_β is related to the ratio of the two Higgs VEVs [9]. The mixing between the hidden and hypercharge gauginos only vanishes when $\delta\hat{M} = \chi\hat{M}_X$.

Without additional symmetries, the *kinetic mixing* χ is generically generated on one-loop level by integrating out chiral superfields charged under both, visible and hidden sector. In this case it acquires values typically around $\chi \sim 10^{-4}$–10^{-2}, corresponding to one-loop suppression [186, 197]. However, *e.g.* in compactifications of heterotic [123, 124] and type II [126–128, 198–200] strings, much smaller mixings are possible. A lower bound around $\chi \gtrsim 10^{-16}$ was argued to hold in cases of gauge mediated supersymmetry breaking in heterotic string models [123], whereas in type-II models with warped extra dimensions or with RR $U(1)$s the kinetic mixing parameter can be parametrically smaller [127, 129]. Below we will treat the mixing as a free parameter and concentrate on the regime $10^{-16} \lesssim \chi \lesssim 10^{-2}$.

The size of the *gaugino mass terms* $\hat{\mathcal{M}}$ in the Lagrangian, Eq. (3.8), is very model dependent. For example, in models with *gravity mediation* [9],

[5] Note that, since we neglect matter in the hidden sector, $\hat{D}_X \equiv 0$.

gaugino masses would arise from the term

$$\mathcal{L} \supset \int d\theta^2 d\bar{\theta}^2 \frac{1}{M_P}(\hat{Z}_1^\dagger \hat{W}_B \hat{W}_B + 2\chi \hat{Z}_2^\dagger \hat{W}_B \hat{W}_X + \hat{Z}_3^\dagger \hat{W}_X \hat{W}_X) + \text{h.c.} \,, \quad (3.12)$$

where coefficients of order one have been dropped. In this equation $\hat{Z}_i$ are three spurion superfields, which will eventually acquire a vacuum expectation value, $\langle \hat{Z}_i \rangle = M_P + \theta^2 F_i$, by some unspecified mechanism[6], yielding $\hat{M}_B = F_1/M_P$, $\delta\hat{M} = \chi F_2/M_P$, $\hat{M}_X = F_3/M_P$, where $M_P \simeq 2.4 \times 10^{18}\,\text{GeV}$ denotes the reduced Planck mass.

The simplest case consists on assuming just one spurion superfield which couples universally to all vector superfields, namely $Z_i \equiv Z$ for all i. If this is the case, at the scale M_P, the different soft terms satisfy the relations $\hat{M}_B = \hat{M}_X = \sqrt{3} M_{\tilde{G}}$ and $\delta\hat{M} = \sqrt{3}\chi M_{\tilde{G}}$, $M_{\tilde{G}}$ being the gravitino mass. Therefore, after the canonical normalization of the gaugino kinetic terms, the mass mixing term $\delta M \propto \delta\hat{M} - \chi\hat{M}_X = 0$ in Eq. (3.11) vanishes. However, the universality of the gaugino mass terms is broken by quantum effects, thus inducing a non-vanishing δM at low energies as long as there exist some heavy hidden sector matter states (which are irrelevant for low-energy phenomenology but have impact on the running of the parameters at high energies). Using the renormalization group equations for the gaugino mass matrix as shown in appendix A.1, we find, starting at the Planck scale M_P for definiteness, that the mass mixing at the electroweak scale reads

$$\delta M_{\text{EW}} \simeq \frac{1}{8\pi^2} g_X^2 B_{XX} \ln\left(\frac{M_P}{M_{\text{hid}}}\right) \chi_{\text{EW}} M_X \,, \quad (3.13)$$

where g_X is the gauge coupling of the hidden $U(1)_X$ gauge group, M_{hid} is the mass scale of hidden sector matter, and $B_{XX} = \sum_i Q_i^2$ is the sum, for all the particles in the theory, of all the hidden $U(1)_X$ charges squared. The index "EW" denotes that these quantities have to be evaluated at the electroweak scale. Furthermore, the renormalization group evolution will also make the hidden gaugino mass smaller at low energies. If there is an enough number of heavy matter states in the hidden sector, the hidden gaugino will become the lightest supersymmetric particle.

[6] We assume that breaking of supersymmetry takes place in a sector that is distinct from the hidden $U(1)_X$ under consideration, hence the D-terms are zero and kinetic mixing has no effect on the MSSM mass spectrum, see Ref. [123].

In more general gravity mediation scenarios like in Eq. (3.12), where several spurion fields contribute to the breaking of supersymmetry, a tree level mixing between the bino and the hidden gaugino will usually remain after canonical normalization of the kinetic terms. The nature of the lightest supersymmetric particle, whether it is the visible sector bino or the hidden gaugino, or even the gravitino, depends then on the details of the model. Below we will mostly assume that the LSP is the hidden gaugino.

The most natural scenarios with a light hidden $U(1)_X$ gaugino are probably those with *gauge mediated supersymmetry breaking* [9, 201]. Assuming that the messenger fields are not charged under the hidden $U(1)_X$ gauge group, the soft mass of the hidden gaugino will entirely come from gravity effects. If this is the case, the gravitino and the hidden $U(1)_X$ gaugino will acquire similar masses, which are naturally much smaller than the masses of the supersymmetric particles of the MSSM. Again, whether the LSP is the gravitino or the hidden gaugino depends on the particle content of the hidden sector, which will drive the hidden gaugino mass to smaller values at low energies through radiative effects.

Below we will study the hidden gaugino scenario independently of the mechanism responsible for the mediation of SUSY breaking, and we will treat the mass of the hidden gaugino, as well as the mixing χ, as free parameters. An important quantity in our analysis will be the *mixing angle* Θ between the bino and the hidden $U(1)_X$ gaugino mass and interaction eigenstates[7]. The diagonalization of Eq. (3.11) yields the approximate expression

$$\Theta \simeq \frac{\delta M^{\rm EW}}{M_B^{\rm EW} - M_X^{\rm EW}} \ , \tag{3.14}$$

where we have emphasized that all the quantities should be evaluated at the electroweak scale. In the scenarios of supersymmetry breaking proposed in this section with hidden $U(1)_X$ gaugino as LSP, the mixing angle Θ can be typically written as

$$\Theta \simeq C \cdot \chi_{\rm EW} \frac{M_X^{\rm EW}}{M_B^{\rm EW} - M_X^{\rm EW}} \ , \tag{3.15}$$

where C is a constant that can roughly vary between $10^{-2} \lesssim C \lesssim 1$, depending on whether $\delta M^{\rm EW}$ is already present at tree level or is generated

[7]Note that we assume that $M_B < M_W < \mu$ throughout this section, see Eq. (3.11).

radiatively, and on the particle content of the hidden sector. For definiteness we will choose $C = 1$ in the subsequent analysis.

3.3.3 Bounds

In this subsection we will discuss bounds on the hidden $U(1)_X$ gaugino scenario, mostly concentrating on cases where the hidden gaugino is the LSP. We will discuss bounds from thermal overproduction and bounds from BBN and structure formation. Finally we will discuss a mechanism that allows to reconcile gravitino dark matter with thermal leptogenesis in certain parameter regimes of our model, in which case the hidden $U(1)_X$ gaugino is assumed to be the NLSP.

The least model dependent bound on the hidden $U(1)_X$ gaugino LSP scenario is the bound that comes from its potential *thermal overproduction* in the early Universe. After reheating of the visible sector (which we conservatively assume does not produce a sizeable amount of hidden gauginos), hidden $U(1)_X$ gauginos can be produced in the hot primeval plasma through mixing with the MSSM neutralinos, potentially resulting in an abundance that is above the one currently observed. This mechanism is similar to the thermal production of gravitinos or axions, see *e.g.* Ref. [184, 202, 203]. However, in contrast to these cases, the final abundance of the hidden $U(1)_X$ gaugino does not depend on the reheating temperature of the Universe, T_R. Instead, it is determined by physics at the electroweak scale. This behavior is a direct consequence of the fact that mass- and kinetic-mixings appear already at the *renormalizable* level of the Lagrangian, whereas gravitino and axion couplings are mass-suppressed. Note that just very recently, the possibility of dark matter production via renormalizable operators was emphasized in Ref. [139], where the corresponding dark matter particle was dubbed *feebly interacting massive particle* (FIMP).

Since the thermal production is most efficient at low temperatures an exact calculation of the hidden $U(1)_X$ gaugino abundance is extremely complicated. This is because at temperatures around $T \sim 100\,\mathrm{GeV}$ the QCD coupling constant g_s is of the order of one, which precludes a sharp separation between hard, T, and soft, $g_s T$, momenta as required for a proper treatment of screening effects with the hard thermal loop approximation [204]. How to deal with this situation is an open problem even in the milder case of gravitino production (see, however, Ref. [184]), and we will make no attempt

Process	$\overline{\lvert\mathcal{M}\rvert^2}/\Theta^2(g'g_s)^2\lvert T^j_{ba}\rvert^2 Y^2_{L,R}$
1) $qg \to \tilde{q}\lambda_X$	$-2\frac{u}{s}$
2) $\tilde{q}\tilde{g} \to \tilde{q}\lambda_X$	$-2\left(\frac{t}{s}+\frac{s}{t}\right)$
3) $\tilde{q}g \to q\lambda_X$	$2\frac{u}{t}$
4) $q\tilde{g} \to q\lambda_X$	4
5) $q\bar{\tilde{q}} \to g\lambda_X$	$-4\frac{s}{u}$
6) $q\bar{q} \to \tilde{g}\lambda_X$	8
7) $\tilde{q}\bar{\tilde{q}} \to \tilde{g}\lambda_X$	$4\left(\frac{t}{u}+\frac{u}{t}\right)$

Table 3.1: Squared matrix elements for inelastic two-body scatterings with a hidden $U(1)_X$ gaugino in the final state. Here, T^i_{ba} denotes the generators of the fundamental representation of the $SU(3)$ gauge group, $Y_{L,R}$ the hypercharges of the (s)quarks, and g' and g_s the gauge couplings of the electroweak and strong interactions, respectively. We averaged over initial and summed over final spins.

to solve this problem here. For our purposes it is enough to derive an order of magnitude estimate on the hidden $U(1)_X$ gaugino abundance.

To this end, we have calculated the collision integral in the relativistic superQCD plasma, taking into account $2 \to 2$ scattering processes with a bino in the final state, and limiting ourself to the dominant processes with one QCD and one hypercharge vertex (*e.g.* processes like $qg \to \tilde{q}B$). Since binos mix with hidden $U(1)_X$ gauginos according to the mixing angle Θ, the production rate of hidden $U(1)_X$ gauginos can be straightforwardly calculated by simply multiplying the above result for thermal bino production by the factor Θ^2. The relevant scattering processes and our results for the corresponding squared matrix elements are listed in Tab. 3.1. Details about the calculation can be found in appendix A.2.

Finally, requiring that $\Omega_X h^2 \lesssim 0.1$ gives the overproduction bound

$$\Theta \lesssim 5 \times 10^{-12} \sqrt{\frac{M_B}{M_X}}\,, \tag{3.16}$$

where we assume implicitly that squark- and gluino masses are around $3M_B$. For other values the bound scales roughly like $\sim \sqrt{M_{\text{squarks/gluinos}}}$.

In Fig. 3.1, where we fixed $M_B = 180\,\text{GeV}$, and Fig. 3.2, with $M_B = 150\,\text{GeV}$, we show the region in the (χ, M_X) parameter space where the hidden $U(1)_X$ gaugino is overproduced (apart from the bino mass both figures differ mainly in the nature of the NLSP, which will become relevant below).

Remarkably, a large part of the parameter space suggested by string theory is excluded by the constraint Eq. (3.16).[8]

The overproduction bound Eq. (3.16) also implies that for mixing parameters around $\chi \sim \mathcal{O}(10^{-12}\text{–}10^{-10})$ the observed relic density can be reproduced. However, even for much smaller mixings, when the thermal hidden gaugino production becomes too inefficient to produce the observed abundance, the hidden gaugino can still be generated in the late decay of other particles, namely the NLSP. This NLSP would often be the visible-sector stau or a neutralino, and we will concentrate on these two cases. In general, when the hidden $U(1)_X$ gaugino is produced thermally and non-thermally via late NLSP decay simultaneously, its abundance today is given by $\Omega_X = \Omega_X^{\text{th.}} + (M_X/M_{\text{NLSP}})\Omega_{\text{NLSP}}^{\text{th.}}$, where $\Omega_{\text{NLSP}}^{\text{th.}}$ and $\Omega_X^{\text{th.}}$ refer to the thermal abundance of the NLSP and the hidden gaugino X, respectively, and M_i are the corresponding masses. If the direct thermal production of the hidden gaugino is negligible, $\Omega_X^{\text{th.}} \ll 1$, we have a prototypic superWIMP scenario, as described in section 3.2.

Below, we will apply all typical bounds that hold for general super-WIMP scenarios, namely bounds from hadrodissociation and catalysis of BBN, and bounds from free-streaming and structure formation (for details see section 3.2) to the case of a hidden $U(1)_X$ gaugino. For the sake of definiteness, we will concentrate on the four typical spectra of SUSY particles shown in Tab. 3.2. In the latter two cases, where the gravitino is part of the spectra, also bounds on mixed cold/warm dark matter models, so-called ΛCWDM scenarios, will become relevant. Note that, following the super-WIMP paradigm, the relic abundance of the neutralino or the slepton is always fixed by the requirement that the LSP constitutes all dark matter today, hence we always assume that $\Omega_{\text{NLSP}}^{\text{th.}} \simeq 0.1\, M_{\text{NLSP}}/M_X$.

Scenario i) Here, the hidden $U(1)_X$ gaugino λ_X is the LSP, and a slepton $\tilde{l}$ is the NLSP. The NLSP decays after its freeze-out into the LSP. Here, the

[8] A sizable annihilation rate between hidden $U(1)_X$ gauginos would allow to circumvent this bound. This can either happen when the mixing angle Θ is of order one and the hidden gaugino approaches the behavior of the visible sector bino, with annihilation cross-sections of the same order, or when additional light matter states would be present in the hidden sector that can mediate the annihilation. Other ways to circumvent the bound are outlined in Ref. [129], which however always requires additional particles or non-standard cosmology.

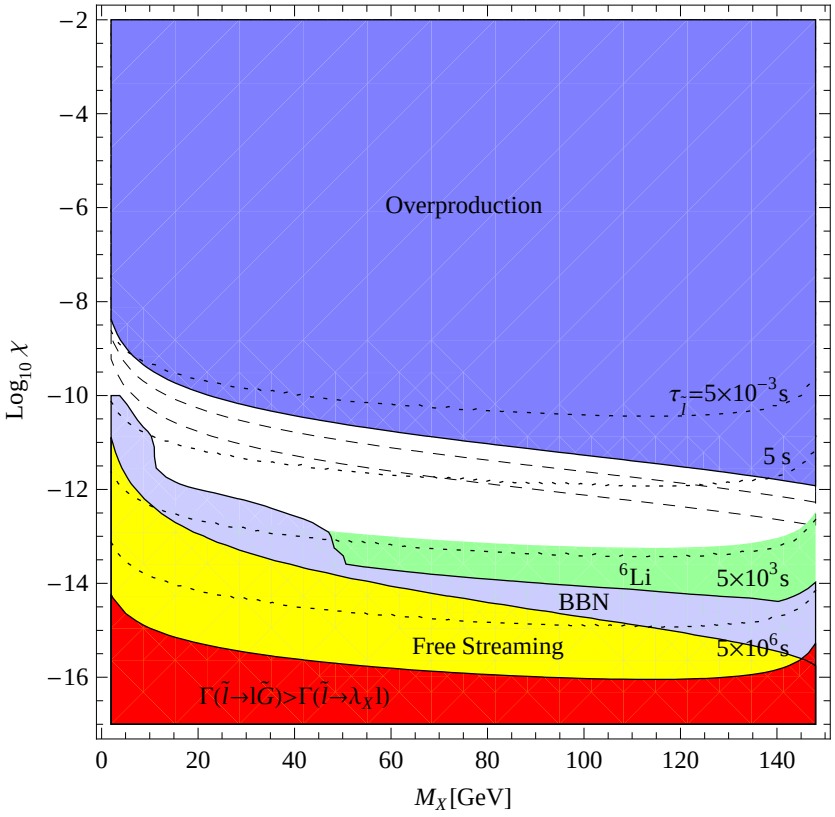

Figure 3.1: Summary of bounds on the hidden $U(1)_X$ gaugino parameter space for the case of a slepton NLSP. We use $M_{\tilde{l}} = 150\,\mathrm{GeV}$ and $M_B = 180\,\mathrm{GeV}$. The upper dark blue region is excluded by thermal overproduction. Below this region, the hidden $U(1)_X$ gaugino is dominantly produced via late decaying sleptons. The light blue region is excluded by energy injection during BBN [25], whereas the light green region is excluded by catalysis of ^{6}Li production [28]. We also show the region which would be excluded solely by free-streaming arguments. The dotted lines show the slepton lifetime. In the presence of a gravitino with $M_{\tilde{G}} = 100\,\mathrm{GeV}$ the slepton would dominantly decay into the hidden $U(1)_X$ gaugino, except in the red lower region. See also Ref. [20].

predominant channel is $\tilde{l} \to \lambda_X l$, the two-body decay into a lepton and the hidden gaugino, and the corresponding decay width is given by

$$\Gamma_{\tilde{l}\to\lambda_X l} \simeq \frac{g'^2}{8\pi}\Theta^2 Y_{\tilde{l}}^2 M_{\tilde{l}} \left(1 - \frac{M_X^2}{M_{\tilde{l}}^2}\right)^2 , \tag{3.17}$$

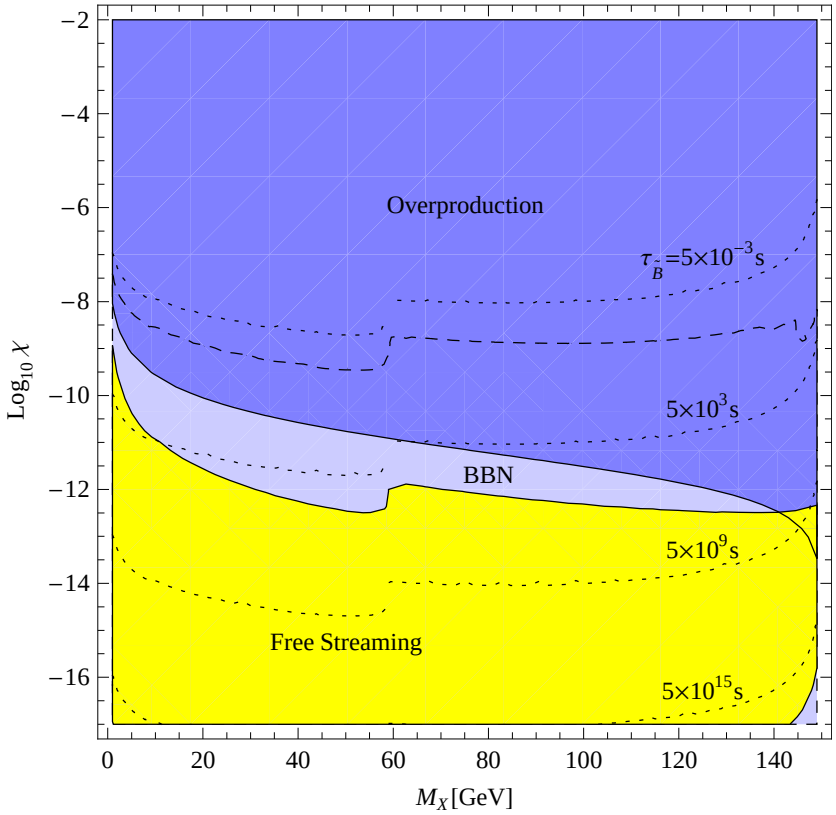

Figure 3.2: Summary of bounds on the hidden $U(1)_X$ gaugino parameter space for the case of a bino-like neutralino NLSP. We take $M_B = 150\,\text{GeV}$. The dark blue region is excluded by thermal overproduction. Below this region, the hidden $U(1)_X$ gaugino would be dominantly produced via late decaying neutralinos. This scenario is totally excluded by BBN [25] (light blue region). The bound actually strongly overlaps with the overproduction region (dashed line). We also show the region (in yellow) that would be solely excluded by free-streaming arguments. The dotted lines show the lifetime of the neutralino. (We used $M_{\text{sf}} = 400\,\text{GeV}$ and $\mu = 300\,\text{GeV}$ for the branching ratios).

where $Y_{\tilde{l}}$ and $M_{\tilde{l}}$ denote, respectively, the hypercharge and the mass of the slepton NLSP. The decay induces electromagnetic cascades in the primordial plasma during BBN (for a definition of parameters and discussion of the BBN bounds see Refs. [25, 183]). The corresponding branching fraction into *electromagnetic energy* is close to one, $B^{\tilde{l}}_{\text{EM}} \simeq 1$, and the corresponding energy release is approximately given by $\epsilon^{\tilde{l}}_{\text{EM}} \approx (M^2_{\tilde{l}} - M^2_X)/(2M_{\tilde{l}})$.

Scenario	*i)*	*ii)*	*iii)*	*iv)*
NNLSP	·	·	slepton	slepton
NLSP	slepton	neutralino	gravitino	λ_X
LSP	λ_X	λ_X	λ_X	gravitino

Table 3.2: The different scenarios that we will investigate in this work.

Contributions to the *hadronic energy* release stem, if kinematically allowed, from three-body decays with Z, $W^\pm$ and Higgs bosons in the final state. The corresponding branching ratios are all of the order of, or smaller than, $\alpha'/(16\pi s_{\rm w}^2) \sim 10^{-2}$, whereas the hadronic branching fractions of the subsequent boson fragmentation are all of the order of one. If these decay channels are kinematically closed, the dominant contribution to hadronic energy release comes from the strongly suppressed four-body decay $\tilde{l} \to \lambda_X l q \bar{q}$, with a branching ratio of the order of 10^{-6}. Hence, the overall hadronic branching fraction is $B^{\tilde{l}}_{\rm had} \sim 10^{-6}$ for large masses of the hidden $U(1)_X$ gaugino ($M_X \gtrsim M_{\tilde{l}} - M_Z$) and $B^{\tilde{l}}_{\rm had} \sim 10^{-2}$ for small masses ($M_X \lesssim M_{\tilde{l}} - M_Z$). Variations in the corresponding hadronic energy release, $\epsilon^{\tilde{l}}_{\rm had}$, are subdominant because $B^{\tilde{l}}_{\rm had}$ varies by several orders of magnitude, and we simply take $\epsilon^{\tilde{l}}_{\rm had} = (1/3)(M_{\tilde{l}} - M_X)$ [183].

Applying the BBN bounds from Ref. [25] to this scenario, a considerable part of the hidden $U(1)_X$ gaugino parameter space can be excluded, as shown in Fig. 3.1 by the light blue region.[9] We also show the region (in light green) that is excluded by the catalytic enhancement of ^{6}Li and ^{9}Be production. The region in the parameter space of the hidden $U(1)_X$ gaugino that is excluded by free-streaming arguments is also shown (yellow) and lies completely in the region already ruled out by BBN (for details see section 3.2).

Scenario ii) In this scenario, the often dominant two-body decays of the neutralino NLSP into the hidden $U(1)_X$ gaugino LSP are accompanied either

[9] In Ref. [25] the bounds are shown for the cases $B_{\rm had} = 1$, 10^{-3} and zero. We just interpolate between $B_{\rm had} = 1$ and $B_{\rm had} = 10^{-3}$ linearly in $\log_{10}(B_{\rm had})$ and use $B_{\rm had} = 0$ as a cutoff. Note that also newer analyses of the BBN bounds exist, namely Refs. [26, 27]. The results from Ref. [26] are similar to the bounds from Ref. [25], but show in some cases also $\mathcal{O}(1)$ or larger differences, whereas Ref. [27] is mainly concentrating on gravitino decay and difficult to compare. However, since in our scenario the strongest bounds come typically from catalytic ^{6}Li production, these differences will not impact our conclusions.

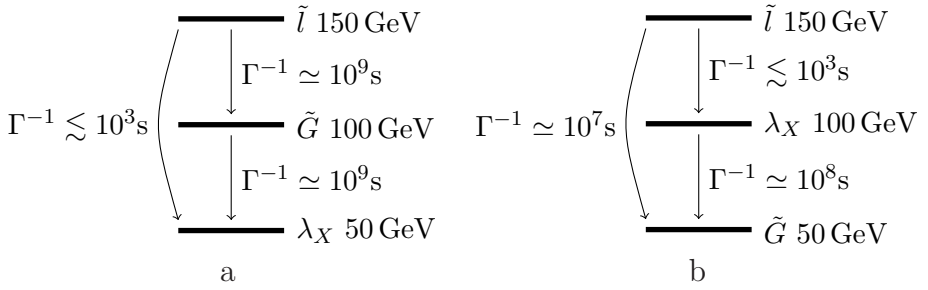

Figure 3.3: Spectra for (a) gravitino NLSP and (b) gravitino LSP (*cf.* last two cases in Tab. 3.2). We show the widths for the different decay processes for typical particle masses. The mixing parameter is assumed to lie in the allowed region of Fig. 3.1.

by a Z or Higgs boson, which in general leads to large hadronic branching fractions. On the other hand, when the decay into Z or Higgs bosons is kinematically forbidden, the NLSP predominantly decays via $\lambda_B \to \lambda_X f \bar{f}$. The always possible radiative two-body decay into LSP-photon pairs is negligible in most cases. For the most common case of a bino-like neutralino, we have summarized all relevant decay widths in appendix A.3. The hadronic branching fraction for the decay of a bino-like neutralino is of $\mathcal{O}(1)$ for hidden $U(1)_X$ gaugino masses that are large enough to allow the decay into Z bosons, and it can range between $\mathcal{O}(10^{-2})$ and $\mathcal{O}(1)$ otherwise (depending on the squark masses). For definiteness we choose a hadronic branching fraction $B_{\rm had}^{\lambda_B} \sim \mathcal{O}(1)$ for all masses M_X, which does not affect our conclusions. For the corresponding energy release we again simply take $\epsilon_{\rm had} = 1/3(M_B - M_X)$.

Applying the BBN bounds of Ref. [25] to this scenario yields the excluded light blue region in Fig. 3.2 (the boundaries of the excluded region are visualized by the dashed line). Together with the overproduction bounds (dark blue region), this scenario is excluded in the whole (χ, M_X) parameter space suggested by string theory, namely $\chi \sim \mathcal{O}(10^{-16}$–$10^{-2})$.[10]

Scenario iii) In this and the next scenario (see Tab. 3.2) we will discuss the typical effects that occur when a light gravitino is included into the spectrum.

[10]Note that in calculating the BBN bounds we assume pure non-thermal production of the LSP, and we neglect possible thermal production for simplicity. The above bounds hold as long as the non-thermal production is not strongly suppressed.

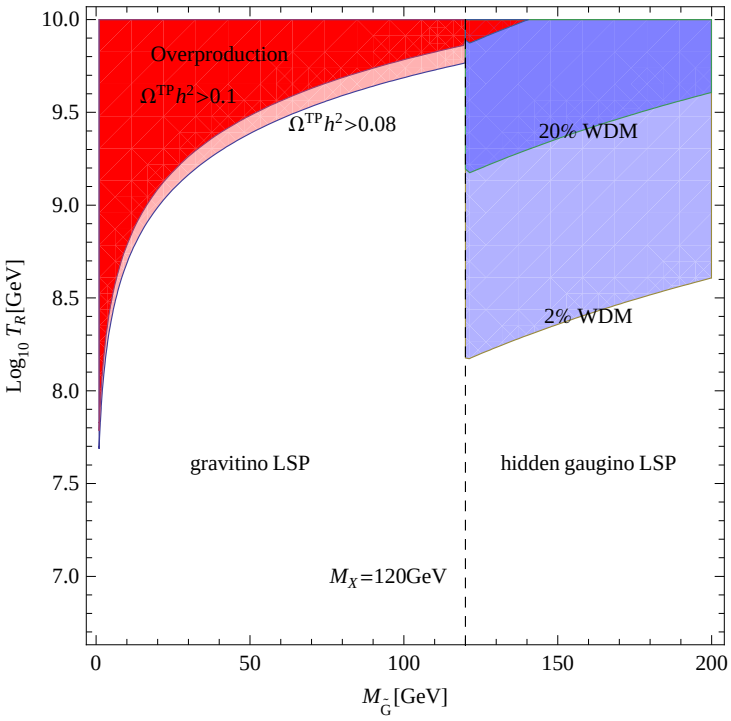

Figure 3.4: Bounds on the reheating temperature as function of the gravitino mass, using Eq. (3.18) with $m_{\tilde{g}} = 800\,\mathrm{GeV}$. The mass of the hidden $U(1)_X$ gaugino is fixed to $M_X = 120\,\mathrm{GeV}$. If the gravitino is the LSP (left part), the reheating temperature is only bounded by overproduction arguments (dark red region), which are only slightly strengthened when, say, 20% of the gravitino abundance is due to non-thermal production (light red region). A gravitino NLSP (right part) would late decay into the hidden $U(1)_X$ gaugino, yielding a warm dark matter component. If only a fraction of 2% or 20% of dark matter is allowed to be warm, the corresponding blue regions are excluded.

To this end, we will concentrate on the spectra illustrated in Fig. 3.3, where we also show typical values for the decay widths. As apparent from this figure, very long lifetimes up to around $\mathcal{O}(10^9\,\mathrm{s})$ are possible in scenarios with light gravitinos, corresponding to large free-streaming lengths around and above $\mathcal{O}(10\,\mathrm{Mpc})$. We will see below that this will make bounds on mixed dark matter with a warm and with a cold component relevant.

If the hidden $U(1)_X$ gaugino is the LSP (see Fig. 3.3a), it can be produced

in three different ways: Thermally, via slepton decay, and via gravitino decay. For mixings and masses that are allowed in Fig. 3.1, the decay of sleptons into gravitinos is strongly suppressed, whereas the decay of gravitinos into hidden $U(1)_X$ gauginos is only accompanied by hidden $U(1)_X$ gauge bosons and hence invisible to MSSM particles. Therefore, bounds from BBN and overproduction are essentially the same than in case *i*). However, this does not hold for the free-streaming bounds, since, in contrast to hidden $U(1)_X$ gauginos which are produced thermally or via slepton decay, hidden $U(1)_X$ gauginos that stem from the decay of gravitinos can have a quite large free streaming length, of the order of several Mpc. This leads to a dark matter scenario with a warm component (hidden gauginos coming from the gravitino decay) and a cold component (hidden gauginos from the other two sources), so-called ΛCWDM models.

Constraints on ΛCWDM models were recently studied in Refs. [170, 205–207]. In general, a warm dark matter component would induce a step in the power spectrum of density fluctuations in the early Universe, with a size which depends on the fraction of the dark matter that is warm and a position which is roughly given by the corresponding free-streaming length as $k_{\rm FS} \sim 2\pi/\lambda_{\rm FS}$. Although models with mixed cold/warm dark matter arise quite naturally in many situations, a full general analysis with all the latest data is still lacking (but see Ref. [170]). However, typical bounds on scenarios with free-streaming lengths in the $\mathcal{O}(10\,\mathrm{Mpc})$ regime are around $f \lesssim 10\%$, where f denotes the fraction of dark matter that is warm, $\Omega_{\rm DM} = f\Omega_{\rm WDM} + (1-f)\Omega_{\rm CDM}$.[11] Bearing in mind this limitation, we will simply show the corresponding bounds on the reheating temperature and mixing parameter for the two reference cases $f \leq 0.2$ and $f \leq 0.02$.

[11] In Ref. [207] a consideration of the uncertainty of the power spectrum from WMAP 1-yr data [158] bounds the fraction f of dark matter that is allowed to have $\lambda_{\rm FS} \simeq 6\,\mathrm{Mpc}$ to be $f \lesssim 0.2-0.4$. This seems to be consistent with a hydrodynamical analysis in Ref. [205], where the bound on the fraction of dark matter that can be made out of thermal light gravitinos with a mass of $M_{\tilde{G}} \approx 16\,\mathrm{eV}$ is stated as $f \lesssim 0.12$, since the corresponding free-streaming length (using Eq. (3.4)) is around $\lambda_{\rm FS} \sim 40\,\mathrm{Mpc}$. However, both analyses do not take into account the latest Lyman-α-forest data [32]. An analysis in Ref. [206] which incorporates these data, and where lower bounds on the mass of sterile neutrino dark matter from Ref. [36] are rescaled for the case of ΛCWDM models, suggests that even a component with a free-streaming lengths around $\lambda_{\rm FS} \sim 4\,\mathrm{Mpc}$ is bounded strongly with $f \lesssim 0.1$. In the more recent analysis in Ref. [170], using the VHS Lyman-α data [208] and WMAP5 results, 2σ-bounds around $f \lesssim 0.05$ were found for a warm fraction with free-streaming lengths around $\mathcal{O}(10\,\mathrm{Mpc})$, corresponding to $\mathcal{O}(1\,\mathrm{km/s})$ thermal velocities.

As explained above, the warm component of hidden $U(1)_X$ gaugino dark matter comes from the late decay of gravitinos. Since, the thermal abundance of gravitinos directly depends on the reheating temperature T_R like [184, 202, 203]

$$\Omega_{\tilde{G}} h^2 \simeq 0.27 \left(\frac{T_R}{10^{10}\,\mathrm{GeV}}\right) \left(\frac{100\,\mathrm{GeV}}{M_{\tilde{G}}}\right) \left(\frac{m_{\tilde{g}}}{1\mathrm{TeV}}\right)^2 , \tag{3.18}$$

where $m_{\tilde{g}}$ denotes the gluino mass, the bounds on ΛCWDM models translate into a bound on the reheating temperature. For the present scenario of a gravitino NLSP these bounds are shown in the right part of Fig. 3.4. As apparent from this figure, reheating temperatures around $10^9\,\mathrm{GeV}$, which are required for successful leptogenesis (see next paragraph), are problematic in this scenario.

Scenario iv) In this scenario the gravitino constitutes dark matter, and the hidden $U(1)_X$ gaugino is the NLSP, whereas the NNLSP is assumed to be the stau. Most interestingly, this special scenario exhibits a mechanism that allows to reconcile gravitino dark matter with thermal leptogenesis.

Thermal leptogenesis is a promising mechanism for the generation of the baryon asymmetry in the Universe [140–142], and the gravitino is a generic prediction of supergravity theories and a well motivated dark matter candidate. But leptogenesis generically requires high reheating temperatures around $10^9\,\mathrm{GeV}$, which, together with forbidding thermal overproduction of a gravitino LSP, translate into an lower bound on the gravitino mass of around $M_{\tilde{G}} \gtrsim 5\,\mathrm{GeV}$ (if the gluino mass is around 500 GeV) [19, 39, 183, 209, 210]. Furthermore, scenarios with a gravitino LSP and a slepton NLSP (often the right-handed stau) are constrained by the fact that the presence of long-lived charged particles during BBN can trigger catalytic production of ^{6}Li and ^{9}Be, as discussed above. The crucial point is now, that the corresponding upper BBN bound on the lifetime of stau translates into an upper bound on the gravitino mass of around $M_{\tilde{G}} \lesssim 1\,\mathrm{GeV}$. Hence there is a generic inconsistency in scenarios with gravitino dark matter and leptogenesis, and different ways to circumvent this problem were discussed in the literature.

One way to relax the tension between leptogenesis and gravitino dark matter is to assume that the production of entropy between the freeze-out of staus and BBN dilutes the stau abundance sufficiently to evade the bounds

[209, 211]. Another way is to impose a small violation of R-parity [39], which allows the stau to decay fast into standard model particles. In this case, the gravitino becomes unstable and decays with a lifetime which is typically longer than the age of the universe. In this case it is a well motivated candidate for decaying dark matter, which will be discussed more in section 3.4. A third way to circumvent the tension between leptogenesis and gravitino dark matter is to assume that the configuration of the MSSM particle spectrum is such that the stau abundance is extremely diluted, as discussed in Refs. [212, 213].

Most interestingly, another way of solving these problems opens up in the presence of a hidden $U(1)_X$ gaugino, as long as the SUSY particle spectra is of the form depicted in the right panel of Fig. 3.3. The essential point of our mechanism is that in presence of the hidden gaugino the lifetime of the stau and the gravitino mass become decoupled, allowing larger gravitino masses and hence larger reheating temperatures. For mixings and masses of the hidden $U(1)_X$ gaugino that lie in the allowed region of Fig. 3.1, the lifetime of the stau is compatible with all BBN bounds, independent of the existence of a gravitino LSP. In this case, we could have a scenario with gravitino dark matter and a stau as the lightest SUSY particle in the MSSM sector, and at the same time reheating temperatures as large as $T_R \sim 10^9\,\mathrm{GeV}$, as shown in Fig. 3.4.

In this scenario, the potentially problematic warm component of gravitino dark matter, with a free-streaming length of the order of several Mpc, comes from the late decay of hidden $U(1)_X$ gauginos. As long as their thermal production is negligible, bounds on the fraction of dark matter that is allowed to be warm in ΛCWDM models directly translate into bounds on the stau abundance, whose decay produces the non-thermal component of the hidden $U(1)_X$ gaugino. The stau abundance is hence bounded like $Y_{\mathrm{stau}} \equiv n_{\mathrm{stau}}/s \lesssim (10^{-13} - 10^{-12})(M_{\tilde{G}}/100\,\mathrm{GeV})^{-1}$ if we allow a fraction $f \leq 0.02 - 0.2$ of dark matter to be warm.[12] Since in the CMSSM with gravitino dark matter the typical relic abundance of stau NLSPs is around $Y_{\mathrm{stau}} \sim \mathcal{O}(10^{-14}\text{–}10^{-13})$ [212, 213], bounds on the fraction of warm dark matter can pose relevant, but not very strong constraints on the particle spectrum and parameters of compatible CMSSM models.

To summarize, the left part of Fig. 3.4 shows the essential bounds on the reheating temperature in our scenario with a gravitino LSP, and as ob-

[12] Here, $s = 2889\,\mathrm{cm}^{-3}$ denotes today's entropy density [1, section 2].

vious from this figure reheating temperatures around 10^9 GeV and therefore leptogenesis are well allowed. A more detailed analysis of the influence of a weakly interacting hidden sector on constraints on the reheating temperature would require more reliable bounds for general ΛCWDM models and is left for future work.

Discussion. Recently, kinetically mixed hidden $U(1)_X$ gauginos were pointed out as being a prototypic examples for FIMP dark matter, which per definition couples to the Standard Model sector via renormalizable couplings [139]. One feature of FIMP dark matter models is that the thermal production is actually strongest at low temperatures, leading to "freeze-in" instead of the freeze-out common in WIMP scenarios. We calculated this thermal production mechanism for the hidden $U(1)_X$ gaugino scenario and derived the corresponding overproduction bounds on the parameter space. Furthermore, we derived different constraints from cosmological observations, namely bounds coming from BBN and structure formation. When the hidden gaugino is the LSP, the actual bounds depend on the nature of the NLSP: If the NLSP is a stau, an allowed band in the parameter space remains, for mixings $\chi \sim 10^{-13}$–10^{-10}; if the NLSP is a bino-like neutralino, the whole parameter space down to $\chi \sim 10^{-16}$ can be excluded for typical mass parameters. A collider signature of the stau NLSP scenario would be the observation of long-lived charged particles, as typical for superWIMP dark matter [39, 40]. Furthermore, we found that in scenarios with a gravitino LSP, a hidden gaugino NLSP and a stau NNLSP, bounds on the reheating temperature that typically hold in case of gravitino dark matter can be considerably relaxed, allowing us to reconcile gravitino dark matter with thermal leptogenesis. The underlying mechanism is expected to be generalizable to other hidden sector models.

3.3.4 Anomalously small mixing

We have shown in the previous sections that constraints from overproduction, BBN and structure formation exclude the scenario with a neutralino NLSP and hidden $U(1)_X$ gaugino for values of the mixing parameter $\chi \sim 10^{-16}$–10^{-2} (see Fig. 3.2). However, these strong constraints could be evaded in more elaborated models yielding a smaller χ. Our interest in exploring the region with small χ is that the neutralino lifetime could become larger than the age of the Universe, thus constituting a viable dark matter candidate

by itself.[13] Nevertheless, in contrast to the standard neutralino dark matter case, in this scenario the neutralino NLSP would be unstable and decay with very long lifetimes into the hidden $U(1)_X$ gaugino LSP and Standard Model particles.

The required tiny mixing parameters for phenomenologically interesting models, typically around $\chi \sim 10^{-24}$ (see Eq. (4.21) below), could be generated in different ways. In scenarios with significant warping, such as KKLT [214], the standard model stack of branes, notably the brane featuring the hypercharge $U(1)_Y$, is placed at a special position—at the tip of a warped throat—while the hidden brane with the $U(1)_X$ is separated from it by a certain distance along the throat. In this case kinetic mixing between hypercharge and the $U(1)_X$ may be exponentially suppressed as discussed in Refs. [21, 127].

Also in heterotic string scenarios, with mixing parameters χ ranging between 10^{-16} and 10^{-2}, one can construct plausible models that effectively yield even much smaller mixings (for details see Ref. [21]). To this end, let us consider a model with *two* hidden $U(1)$ gauge groups, $U(1)_X$ and $U(1)_{X'}$, and vector superfields denoted by $\hat{X}$ and $\hat{X}'$, respectively. We will assume that the hidden sector particles that generate the kinetic mixing are charged either under $U(1)_Y$ and $U(1)_{X'}$, or under $U(1)_X$ and $U(1)_{X'}$, but not under $U(1)_Y$ and $U(1)_X$ simultaneously. If this is the case, the kinetic mixing terms $\chi_1 \hat{W}_B^\alpha \hat{W}_{X'\,\alpha}$ and $\chi_2 \hat{W}_X^\alpha \hat{W}_{X'\alpha}$ will be generated, but not terms proportional to $\hat{W}_B^\alpha \hat{W}_{X\,\alpha}$. Then, after the canonical normalization of the kinetic terms, an effective mass mixing term between the bino and the hidden gaugino λ_X will be generated, $\delta M_{12} \simeq \chi_1\,\chi_2\,(M_X + M_{X'}) - \chi_2\,\delta\hat{M}_1 - \chi_1\,\delta\hat{M}_2$, which is doubly suppressed by χ_1 and χ_2. If λ_X is the LSP and λ_B is the NLSP, the decay rate of the bino NLSP is then very strongly suppressed, thus yielding a very long lifetime for neutralino dark matter. Assuming that the kinetic mixing between the observable sector and the hidden sector is $\chi_1 \sim 10^{-16}$ (the lower limit of what is plausible in heterotic scenarios) a mixing between the two hidden sector $U(1)$s of $\chi_2 \sim 10^{-7}$ would be necessary in order to render a neutralino lifetime of $\mathcal{O}(10^{26}\,\mathrm{s})$.

The above discussions suggest that it is well possible to obtain mixing parameters small enough to cause NLSP decay with lifetimes relevant for

[13] Clearly, the scenario with charged slepton NLSP is excluded for very small values of χ, since it would yield an abundance of anomalously heavy hydrogen in conflict with the experimental constraints [150].

cosmic-ray experiments, hence making it an interesting decaying dark matter candidate. Other examples for decaying dark matter models are discussed next in section 3.4, the cosmic-ray predictions for the above scenario with neutralino dark matter decaying into hidden $U(1)_X$ gauginos, or vice versa, are worked out in section 4.2.3.

3.4 Decaying Dark Matter

A number of theoretically well motivated models predict the decay of dark matter particles on cosmological time scales, namely with lifetimes around and above $\tau_{\rm DM} \simeq \mathcal{O}(10^{26}\,{\rm s})$, which are typically required to be not in conflict with, but still in reach of, current cosmic-ray observations.

Among these models is the gravitino with a small violation of R-parity and lepton number, as can be caused by spontaneous B-L breaking [39]. In this scenario the gravitino decays with a decay widths that is doubly suppressed by the Planck-mass and by the small R-parity violation, leading to lifetimes order of magnitudes larger than the age of the Universe, with potentially observable effects on the cosmic-ray fluxes, see *e.g.* Refs. [41, 83, 92, 215, 216]. Hence it is an example for decaying dark matter, which in addition is attractive because it allows a consistent thermal history of the Universe, including thermal leptogenesis as source of the baryon asymmetry [39]: As discussed above (scenario iv of subsection 3.3.3), gravitinos with R-parity conservation often are in conflict with the BBN if the reheating temperature is high, due to the late Planck-mass suppressed NLSP decay. This problem is generically resolved if a small violation of R-parity is allowed that opens additional and less suppressed decay channels for the NLSP.

A different example for decaying dark matter, though in a completely different mass range of $\mathcal{O}(10\,{\rm keV})$, are sterile neutrinos. In particular the minimalistic setup reviewed in Ref. [217] is attractive, where the Standard Model is simply extended by three sterile neutrinos. This setup, called νMSM, can account for dark matter, neutrino oscillation and can explain the baryon asymmetry of the Universe. At the same time the dark matter particle, which is the lightest sterile neutrino, has cosmological lifetimes due to tiny Yukawa couplings. Its mass lies in the range $1\,{\rm keV} \lesssim m_s \lesssim 50\,{\rm keV}$, for lower or higher masses it is in conflict with phase-space density constraints on fermionic dark matter or in conflict with X-ray constraints, respectively.

The X-ray constraints follow from the two-body decay of the sterile neutrino into a neutrino and a gamma-ray line, $\nu_s \to \nu\gamma$, which makes this model accessible to, and actually strongly constrained by, indirect searches.

But even in models where dark matter is stable in the first place, the consideration of higher-dimensional operators often renders the dark matter particle unstable with cosmological lifetimes. This is in particular the case when the symmetry that is protecting the dark matter particle from decaying on the renormalizable level of the Lagrangian is violated by dimension-six operators suppressed by some high mass scale M_*. This mass scale would be often close to the GUT scale $M_{\rm GUT} \simeq 2\times10^{16}\,\text{GeV}$ [9]. A simple dimensional estimate of the dark matter lifetime yields[14]

$$\tau_{\rm DM} \sim 8\pi\frac{M_*^4}{M_{\rm DM}^5} \simeq 3\times10^{27}\,\text{s}\left(\frac{M_*}{2\times10^{16}\,\text{GeV}}\right)^4\left(\frac{1\,\text{TeV}}{M_{\rm DM}}\right)^5\,, \tag{3.19}$$

which, for $M_* \approx M_{\rm GUT}$ and for characteristic dark matter masses in the TeV regime, is well in the ball park of lifetimes interesting for cosmic-ray experiments, as will be discussed below. An explicit example for this situation is hidden $SU(2)$ vector dark matter as developed in Refs. [44, 45]: In this scenario dark matter is identified with the massive vector bosons of a hidden sector $SU(2)$ gauge group which extends the Standard Model particle content. On the renormalizable level of the Lagrangian the stability of the gauge bosons is ensured by a $SO(3)$ custodial symmetry, which however can be violated by dimension-six operators, leading to dark matter decay which is potentially observable in the cosmic-ray fluxes. For other examples with dimension-six operators in context of cosmic-rays see *e.g.* Refs. [42, 43].

Lastly, another interesting model of decaying dark matter is the kinetically mixed hidden $U(1)_X$ gaugino with exponentially suppressed couplings, as discussed above in section 3.3.4.

Since the indirect detection signals from decay differ in general from the ones of annihilation, a dedicated study of cosmic-ray signals from decaying dark matter is mandatory. We will outline different aspects of these indirect signals in chapter 4, with emphasis on the $e^\pm$- and the gamma-ray channels. In section 4.2.3, we will, as a concrete example, also study the cosmic-ray signatures from the hidden $U(1)_X$ gaugino dark matter scenario.

[14] See Ref. [43] for details. Note that dimension-five operators would lead to lifetimes of the order of seconds, with possible impact on BBN.

Chapter 4

Indirect Searches for Decaying Dark Matter

As outlined in chapter 3, the most popular type of dark matter candidate, the WIMP, can naturally reproduce the observed dark matter abundance due to effective self-annihilation in the early Universe, after being in thermal equilibrium with the baryons before. Today, this same annihilation process is expected to produce a possibly observable contribution to the measured cosmic-ray[1] fluxes on Earth. Detection of such an indirect signal would be the first non-gravitational evidence for dark matter, with paramount importance to the understanding of its nature. A lot of effort has been made to study the prospects and predictions of cosmic-ray signatures from annihilating dark matter [50–53, 122]. However, this is not the only possibility for the indirect detection of dark matter. Many dark matter models predict that the dark matter particle is unstable and *decays* with very long lifetimes [21, 39, 43, 45, 84, 96, 217], see also section 3.4. If the decays occur at a sufficiently large rate, the decay products could be observable as an exotic contribution to the high energy cosmic ray fluxes of gamma rays, electrons, positrons, antiprotons, neutrinos or antideuterons [82, 105, 177–181]. Among these, the gamma-ray channel is probably the most important to study, due to its sensitivity to far-distant sources and its potential to discriminate between signals from annihilating or decaying dark matter and astrophysical sources.

Any interpretation of cosmic-ray observations in terms of dark matter re-

[1] As mentioned in the introduction, *cosmic rays* will denote high-energetic nuclei, electrons and positrons as well as gamma rays throughout this work.

quires a detailed and reliable understanding of the astrophysical backgrounds. In this chapter we will firstly give a short overview over recent cosmic-ray observations and discuss their astrophysical understanding in terms of propagation models. We will then discuss the recent measurement of the positron fraction of cosmic rays by the PAMELA experiment in light of decaying dark matter. Lastly, we will present a detailed study of the peculiar gamma-ray predictions for decaying dark matter scenarios.

4.1 Cosmic-Ray Observations

Cosmic-ray measurements were pioneered by Nobel-laureate Victor Hess, who conducted the first dedicated balloon measurements of ionizing radiation in 1912. The term "cosmic rays" was later introduced by Robert Millikan, who proved their extraterrestrial origin. Today a large variety of different cosmic-ray observations exists. In this section we will give a short overview over the cosmic-ray observations that are relevant for our analysis. Firstly we will discuss gamma-ray observations, secondly electrons and positrons and finally antiprotons.

The first direct observations of Galactic *gamma-rays* were performed by the satellite *Explorer XI*, and they date back to 1961. Much later in the 1990s, and as already discussed in the introduction, a full-sky observation of gamma rays up to energies of 10 GeV was undertaken by the *Energetic Gamma Ray Experiment Telescope* (EGRET). The gamma-ray sky measured by EGRET was highly anisotropic, and it showed a number of resolved sources [55], such as blazars, as well as an unresolved diffuse component [56, 57]. This diffuse component is almost entirely due to Galactic emission, and the corresponding production mechanisms (inverse Compton scattering, π^0 production and bremsstrahlung) are by now well understood. The different production mechanisms are all related to charged cosmic-ray that propagate through our Galaxy. Remarkably, the same propagation models that can reproduce the observed abundances of charged cosmic-rays at Earth can also predict the full-sky gamma-ray map with rather good accuracy [56, 60]. However, apart from the Galactic emission, there exists also an isotropic extragalactic diffuse gamma-ray component, the EGBG, which is expected to come mainly from unresolved extragalactic point sources [61].

The most recent and accurate observation of the gamma-ray sky is cur-

rently undertaken by the *Large Area Telescope* (LAT) on the *Fermi Gamma-ray Space Telescope*. The Fermi collaboration is taking data since June 2008, and some preliminary results for the overall diffuse flux were already presented [218–220]. Furthermore, since around July 2009, the photon event data is publicly available and can be used for full-sky analyses, although the available data is still plagued with large background contamination at high energies. We will discuss the observational prospects of the Fermi LAT gamma-ray measurements with regard to decaying dark matter in more detail below.

Among all different kinds of charged cosmic rays, one particular channel raised a lot of interest and attention in the astro- and particle-physics communities in the last year: *electrons and positrons* with energies between around 10 GeV and a few TeV. Different experiments reported a wealth of new results pointing to the existence of a new local $e^{\pm}$-source. Rather than measuring the positron and electron fluxes separately, present experiments often measure either the positron fraction or the overall electron plus positron flux. This is due to technical reasons, since in the former case most sources of systematic errors, such as detector acceptance or trigger efficiency, cancel out by computing the ratio of particle fluxes, whereas in the latter case experiments often cannot distinguish between electrons and positrons.

End of 2008 the PAMELA collaboration reported evidence for a sharp rise of the positron fraction at energies $7 - 100$ GeV [75], possibly extending toward even higher energies. This result confirmed previous hints about the existence of a positron "excess" from HEAT [221], CAPRICE [222] and AMS-01 [223]. Almost at the same time, the balloon-borne experiments ATIC [224] and PPB-BETS [225] reported the discovery of a peak in the total electron plus positron flux at energies $600 - 700$ GeV. However, the existence of this peak was later not confirmed by the Fermi LAT, when the collaboration published measurements of the electron plus positron flux from 20 GeV to 1 TeV with unprecedented accuracy [76]. Instead, Fermi LAT revealed an energy spectrum that roughly follows a power law $\propto E^{-3.0}$ without prominent spectral features, in conflict with the ATIC/PPB-BETS measurements. Simultaneously, the H.E.S.S. collaboration reported a measurement of the cosmic-ray electron plus positron spectrum at energies larger than 340 GeV up to several TeV, confirming the Fermi result of a power-law spectrum with spectral index of around 3.0, which however furthermore steepens at about 1 TeV [80, 81]. Below, we will furthermore include results for the electron plus

positron flux that come from the experiments BETS [226], AMS-01 [227] and HEAT94/95 [228].

The measured energy spectrum, together with the observed rise in the positron fraction, suggests indeed the existence of new local sources of primary high-energetic electrons and positrons. This is mainly based on the fact that state-of-the-art propagation models fail to reproduce the PAMELA measurements of the positron fraction above energies of 10 GeV. As summarized in the introduction, these results have led to many proposals trying to explain this excess, including nearby pulsars and more exotic explanations like dark matter annihilation or decay. Below, we will discuss in detail the interpretation in terms of decaying dark matter.

Another cosmic-ray channel which is very sensitive to possible dark matter contributions is constituted by the antiprotons, since the astrophysical background is purely secondary and relatively low. In the past the absolute antiproton flux was measured by many different experiments, like BESS95 [229], BESS95/97 [230], CAPRICE94 [231], CAPRICE98 [232] and IMAX [233]. Furthermore, some experiments only determined the antiproton-to-proton ($\bar{p}/p$) ratio. Most recently this was done by PAMELA [112], other results come from *e.g.* BESS [234] and HEAT [235]. The observations turn out to be consistent with the expectations from conventional propagation models, which excludes the possibility of a large antiproton flux coming from dark matter annihilation or decay [175, 236]. The antiproton measurements put strong constraints on the dark matter interpretation of the PAMELA positron excess (note that pulsars do not produce antiprotons). Further, however subdominant, constraints from other antimatter channels like antideuterons can be found in *e.g.* Refs. [179, 180].

4.2 Antimatter Signals

Due to CP-conservation, dark matter decay or annihilation usually produces the same amount of particles as anti-particles. Together with the observed low astrophysical antimatter backgrounds, cosmic-ray antimatter fluxes—most importantly positrons, antiprotons and antideuterons—provide a sensitive indirect probe of different dark matter models.

In this section we will discuss indirect searches for decaying dark matter, concentrating on the $e^{\pm}$- and antiproton-channels in light of the recent ob-

servations by PAMELA and the Fermi LAT. After a short introduction we will discuss the diffusion equations that govern the cosmic-ray propagation in the Galaxy in section 4.2.1. In section 4.2.2 we will analyze the decaying dark matter interpretation of the rise in the positron fraction as observed by PAMELA in general, and in section 4.2.3 in the special case of hidden $U(1)_X$ gaugino dark matter.

4.2.1 Cosmic-ray propagation

Charged primary cosmic-rays, like p, e^-, ^{4}He and ^{12}C, are presumably produced in supernova remnants, which are concentrated in the Galactic disk. After production, they propagate through the tangled Galactic magnetic field, following the average magnetic field lines and scattering on random field irregularities. On scales of around 100 pc and larger, the random components are comparable to the average field, and the propagation, which is strongly anisotropic on smaller scales, becomes approximately isotropic. This aspect of the cosmic-ray propagation is commonly modeled by a diffusion equation, with a diffusion coefficient that is determined by comparison with the observations. Besides diffusion, also convection and reacceleration can play a significant role: Convection occurs as consequence of strong Galactic winds, reacceleration denotes the stochastic acceleration of cosmic rays by scattering on randomly moving magneto-hydrodynamic waves. Spallation of primary cosmic rays on the ISM generate furthermore secondary cosmic-ray species, like Li, Be, B, e^+ and $\bar{p}$. These can be used to determine the correct propagation parameters, in particular by considering secondary-to-primary ratios like the Boron-to-Carbon ratio (B/C). See Ref. [60] for a recent review about the astrophysics of cosmic-ray production and propagation.

The diffusive propagation of charged cosmic rays is commonly described using a stationary two-zone diffusion model with cylindrical boundary conditions [77].[2] Under this approximation, the differential number density of antiparticles, $n(p, \vec{r}, t)$, being a function of momentum p, position $\vec{r}$ and time t, satisfies the following transport equation (we loosely follow the treatment of Ref. [237] and concentrate only on the effects that are later relevant for

[2] At the energies in the GeV–few TeV range, which are relevant for this work, only antimatter created within the Galaxy is of importance, extragalactic sources can be neglected.

the semi-analytical solutions of the transport equation):

$$\begin{aligned} \frac{\partial n}{\partial t} &= \nabla \cdot [D(p,\vec{r})\nabla n] + \\ &\quad + \frac{\partial}{\partial p}[b(p,\vec{r})n] - \nabla \cdot [\vec{V_c}(\vec{r})n] - 2h\delta(z)\Gamma_{\rm ann} n + Q(p,\vec{r}) \ . \end{aligned} \tag{4.1}$$

We assume free escape conditions and require that the antimatter density n vanishes at the boundary of the diffusion zone, which is approximated by a cylinder with a variable half-height $L = 1$–15 kpc and a fixed radius $R = 20$ kpc. Concentrating on steady-state solutions furthermore implies $\partial n/\partial t \equiv 0$. Note that in Eq. (4.1) we already neglected reacceleration which is only relevant at low energies, the full expression can be found in Ref. [60].

The first term on the right-hand side of Eq. (4.1) accounts for the diffusive motion through the Galactic magnetic field. The diffusion coefficient $D(p,\vec{r})$ is commonly assumed to be a constant scalar throughout the whole diffusion zone, and it is parameterized as

$$D(p) = D_0 \ \beta \ \mathcal{R}^{\delta} \ , \tag{4.2}$$

where $\beta = v/c$ is the velocity in units of the speed of light c, and $\mathcal{R}$ is the magnetic rigidity of the particle, which is defined as the momentum in GeV per modulus of unit charge, $\mathcal{R} \equiv p[\mathrm{GeV}]/|Z|$ (for antiprotons and positrons simply $|Z| = 1$). The normalization D_0 and the spectral index δ of the diffusion coefficient are directly related to the irregularities of the Galactic magnetic field and must be inferred from observations, see below. The second term accounts for energy losses, which are, at energies above a few GeV and in case of positrons, mainly due to inverse Compton scattering on the interstellar radiation field (ISRF) and synchrotron radiation from interaction with the Galactic magnetic field, but include in principle also energy losses due to interaction with the ISM [60]. The third term is the convection term, which accounts for the drift of charged particles away from the disk as induced by the Galactic wind. It usually has axial direction, pointing away from the Galactic disk. The fourth term accounts for antimatter annihilation due to interactions with the ISM in the Galactic disk.

The transport equations for antiprotons and positrons can be approximated by different limits of Eq. (4.1). By exploiting the cylindrical symmetry of the problem, it is possible to find semi-analytical solutions to the approximate transport equation in each case, and we will use these semi-analytical

solutions later for calculating the propagated positron and antiproton spectra. Instead, one could also use numerical codes like GalProp.[3]

Positron Flux. For the case of the positrons (or electrons), Galactic convection and annihilation in the disk can be neglected in the transport equation at high energies, which is then simplified to [237, 238]:

$$\nabla \cdot [D(E,\vec{r})\nabla n_{e^+}] + \frac{\partial}{\partial E}[b(E,\vec{r})n_{e^+}] + Q_{e^+}(E,\vec{r}) = 0 \,, \tag{4.3}$$

where, following Ref. [237, 238], the rate of energy loss, $b(E,\vec{r})$, is approximated by a spatially constant function parameterized by $b(E) = \frac{E^2}{E_0 \tau_E}$, with $E_0 = 1$ GeV and $\tau_E = 10^{16}$ s (which is a reasonable but rough approximation to the true value at energies above 10 GeV at the position of the Sun, *cf.* Ref. [70, Fig. 1]). As said above, the energy losses are mainly due to ICS with the ISRF and synchrotron radiation, and the adopted approximation is required for finding semi-analytical solutions to the propagation equation. Lastly, $Q_{e^+}(E,\vec{r})$ is the source term of positrons as in general given by

$$Q_i(E,\vec{r}) = \frac{\rho(\vec{r})}{M_{\rm DM}\,\tau_{\rm DM}} \frac{dN_i}{dE} \,, \tag{4.4}$$

where $i = e^+, \bar{p}, \ldots$ denotes the particle species, dN_i/dE is the differential number of particles i produced in the decay with energies in the range $E \ldots E + dE$, and $\rho(\vec{r})$ is the density profile of dark matter particles in the Galactic dark matter halo halo.

Together with the above cylindrical boundary conditions, the propagation of positrons can be described by just three parameters, the normalization D_0 and the spectral index δ of the diffusion coefficient, and the height of the diffusion zone, L. The solution to this equation at position of the Sun, $r = R_\odot$, $z = 0$, is then formally given by the convolution

$$n_{e^+}(E) = \frac{1}{M_{\rm DM}\tau_{\rm DM}} \int_0^{E\max} dE'\, G_{e^+}(E,E')\, \frac{dN_{e^+}(E')}{dE'} \,. \tag{4.5}$$

Here the explicit form of the Green's function is [237, 238]

$$G_{e^+}(E,E') = \sum_{n,m=1}^{\infty} B_{nm}(E,E') J_0\left(\zeta_n \frac{R_\odot}{R}\right) \sin\left(\frac{m\pi}{2}\right) , \tag{4.6}$$

[3] See `http://galprop.stanford.edu/`, Ref. [108] for an example, and Refs. [60, 176] for comments about the differences between the approaches.

where J_0 is the zeroth-order Bessel function of the first kind, whose successive zeros are denoted by ζ_n. We also defined the quantity

$$B_{nm}(E,E') = \frac{\tau_E E_0}{E^2} C_{nm} \times \times \exp\left\{ \left(\frac{\zeta_n^2}{R^2} + \frac{m^2\pi^2}{4L^2} \right) \frac{D_0 \tau_E}{\delta - 1} \left[\left(\frac{E}{E_0} \right)^{\delta-1} - \left(\frac{E'}{E_0} \right)^{\delta-1} \right] \right\}, \tag{4.7}$$

with

$$C_{nm} = \frac{2}{J_1^2(\zeta_n) R^2 L} \int_0^R r' dr' \int_{-L}^{L} dz' \rho(\vec{r}\,') J_0\left(\zeta_n \frac{r'}{R} \right) \sin\left[\frac{m\pi}{2L}(L - z') \right] , \tag{4.8}$$

where J_1 is the first-order Bessel function.

The interstellar flux (particles per unit area, solid angle, unit time and unit energy) of primary positrons, produced by the source term in Eq. (4.4), is then finally given by:

$$\Phi_{e^+}^{\rm DM}(E) = \frac{c}{4\pi} n_{e^+}(E) \, . \tag{4.9}$$

Since in all practical cases the decay spectrum of electrons and positrons is identical, we furthermore have $\Phi_{e^-}^{\rm DM} = \Phi_{e^+}^{\rm DM}$.

Antiproton flux. Energy losses are negligible for antiprotons at higher energies, since due to their large mass they do not suffer ICS and synchrotron losses, and their propagation is typically dominated by diffusion, see Ref. [239, Fig. 1]. Then the transport equation for the antiproton density, $n_{\bar{p}}(p, \vec{r}, t)$, is given by (we are following the treatment in Refs. [83, 237], more details can be found in Refs. [236, 239, 240]):

$$\nabla \cdot (D(p,\vec{r}) \nabla n_{\bar{p}}) - \nabla \cdot (\vec{V_c}(\vec{r}) n_{\bar{p}}) - 2h\delta(z) \Gamma_{\rm ann} n_{\bar{p}} + Q_{\bar{p}}(p,\vec{r}) = 0 \, , \tag{4.10}$$

where the annihilation rate $\Gamma_{\rm ann}$ is determined by the ISM density and the proton-antiproton annihilation cross-sections, for which we use the parameterization of Ref. [241] as discussed in Refs. [83, 237]. At lower energies, antiprotons are affected by convection, and we will assume that the Galactic wind has axial direction $\vec{k}$ and that it is constant inside the diffusion region: $\vec{V_c}(\vec{r}) = V_c \, \mathrm{sign}(z) \, \vec{k}$.

As for the case of electrons and positrons, the solution of the transport equation at position of the Sun can now be formally expressed by the convolution

$$n_{\bar{p}}(T) = \frac{1}{M_{\rm DM}\,\tau_{\rm DM}} \int_0^{T_{\rm max}} dT'\; G_{\bar{p}}(T,T')\;\frac{dN_{\bar{p}}(T')}{dT'}\;, \tag{4.11}$$

where $T_{\rm max} = M_{\rm DM} - m_p$ and m_p is the proton mass, and $n_{\bar{p}}$ is given as function of the kinetic energy T. Finally, the interstellar flux of primary antiprotons is given by

$$\Phi_{\bar{p}}^{\rm DM}(T) = \frac{v}{4\pi} n_{\bar{p}}(T)\;, \tag{4.12}$$

where v is the velocity of the antiprotons.

The analytic expression for the Green's function reads [237]:

$$\begin{aligned} G_{\bar{p}}(T,T') &= \sum_{i=1}^{\infty} \exp\left(-\frac{V_c L}{2D(T)}\right) \times \\ &\quad \times \frac{y_i(T)}{A_i(T)\sinh(S_i(T)L/2)} J_0\left(\zeta_i \frac{R_\odot}{R}\right) \delta(T-T')\;, \end{aligned} \tag{4.13}$$

where

$$\begin{aligned} y_i(T) &= \frac{4}{J_1^2(\zeta_i)R^2} \int_0^R r'\,dr'\; J_0\left(\zeta_i \frac{r'}{R}\right) \times \\ &\quad \times \int_0^L dz' \exp\left(\frac{V_c(L-z')}{2D(T)}\right) \sinh\left(\frac{S_i(L-z')}{2}\right) \rho(\vec{r}\,')\;, \end{aligned} \tag{4.14}$$

and

$$A_i(T) = 2h\Gamma_{\rm ann}(T) + V_c + D(T)S_i(T)\coth\frac{S_i(T)L}{2}\;, \tag{4.15}$$

$$S_i(T) = \sqrt{\frac{V_c^2}{D(T)^2} + \frac{4\zeta_i^2}{R^2}}\;. \tag{4.16}$$

Propagation Model Parameters. The free parameters of the propagation equation can be gauged by comparing predicted and observed ratios of secondary cosmic rays to primary cosmic rays. The typical example is the B/C ratio, since B is entirely secondary, and the B/C ratio is better measured than other ratios, up to energies around 1 TeV [242].

Model	δ	$D_0\,[\mathrm{kpc}^2/\mathrm{Myr}]$	$L\,[\mathrm{kpc}]$
M2	0.55	0.00595	1
MED	0.70	0.0112	4
M1	0.46	0.0765	15

Table 4.1: Astrophysical parameters as found in Ref. [238] to be compatible with the B/C ratio that yield the minimum (M2), median (MED) and maximal (M1) flux of positrons.

In our numerical analysis of the electron and positron fluxes we will, if not stated otherwise, adopt the propagation model parameters of the MED propagation model defined in Refs. [176, 238]: $\delta = 0.70$, $D_0 = 0.0112\,\mathrm{kpc}^2/\mathrm{Myr}$ and $L = 4\,\mathrm{kpc}$, see also Tab. 4.1. The other two models shown in Tab. 4.1, M1 and M2, are tuned to maximize or minimize the positron flux within the observationally allowed set of propagation models. However, our results for the electron and positron flux are rather insensitive to the choice of the concrete propagation model, since the propagation is dominated by energy losses, as we will demonstrate below (see Fig. 4.7).

Model	δ	$D_0\,[\mathrm{kpc}^2/\mathrm{Myr}]$	$L\,[\mathrm{kpc}]$	$V_c\,[\mathrm{km/s}]$
MIN	0.85	0.0016	1	13.5
MED	0.70	0.0112	4	12
MAX	0.46	0.0765	15	5

Table 4.2: Astrophysical parameters as found in Ref. [176] to be compatible with the B/C ratio that yield the minimal (MIN), median (MED) and maximal (MAX) flux of antiprotons.

On the other hand, the prediction of the antiproton flux from dark matter decay is very sensitive to the choice of propagation parameters. Therefore, we will show in this case results for the three different propagation models that are consistent with the observed B/C ratio and that give the maximal (MAX), median (MED) and minimal (MIN) antiproton flux [240]. The relevant parameters are summarized in Tab. 4.2.

Solar Modulation. When charged cosmic rays come into the vicinity of the Sun they suffer from energy loss due to interaction with the outgoing solar wind. This mechanism is called solar modulation and becomes severe if the energy of the observed cosmic rays is small, in the few GeV region and below. Using the force-field approximation [243] to account for solar modulation, the modulated fluxes at top-of-atmosphere (TOA) are related to the unmodulated local interstellar (IS) flux at the heliospheric boundary by the relation [240, 244]

$$\Phi_i^{\rm TOA}(E_{\rm TOA}) = \frac{p_{\rm TOA}^2}{p_{\rm IS}^2}\,\Phi_i^{\rm IS}(E_{\rm IS})\,. \tag{4.17}$$

Here, i denotes the particle species, $E_{\rm IS} \equiv E_{\rm TOA} + \phi_F$, with $E_{\rm IS}$ and $E_{\rm TOA}$ being the energies of the particle before and after solar modulation, respectively, $p_{\rm IS}$ and $p_{\rm TOA}$ denote the corresponding momenta, and ϕ_F is the phenomenological solar modulation parameter, which varies between around 500 MV and 1.3 GV over the eleven-year solar cycle [237]. In order to compare our predictions with the AMS-01 and HEAT data we will take $\phi_F = 550$ MV.

4.2.2 Positron excess from decaying dark matter

As outlined above, the rise in the positron fraction above 10 GeV, as measured by PAMELA, strongly suggests the existence of a new local primary source of positrons and electrons. Different interpretations of this observation have been proposed in the recent past, and after a short introduction we will concentrate on the interpretation in terms of decaying dark matter. In the next section we will also discuss related prospects and predictions for the currently ongoing gamma-ray observations by the Fermi LAT experiment.

The most common astrophysical explanation of the electron/positron excesses is the electron-positron pair production by the interactions of high-energy photons in the strong magnetic field of local *pulsars* [113–121]. These pulsars could be nearby [113, 115, 120, 121], such as Geminga or Monogem, requiring that around 40% of their spin-down power is ejected in the form of electron-positron pairs. Or, alternatively, the observations could be explained by the combined emission of a larger set of nearby and distant pulsars, requiring a smaller fraction around 10%–30% of spin-down power going into electrons and positrons [114]. In both cases the electron/positron energy spectrum has to extend up to energies around 1 TeV. Another alternative

which was proposed is that the positrons could be originating from the decay of charged pions, which are in turn produced by the hadronic interactions of high-energy protons accelerated by nearby sources [245].

An arguably more exciting explanation of the cosmic-ray electron/positron excesses is the possibility that the electrons and positrons are produced in the annihilation [103–111] or the decay [21, 43, 48, 49, 82–102] of *dark matter* particles. The interpretation of the PAMELA excess in terms of dark matter is subject to constraints from the flux measurements of other cosmic-ray species. As already mentioned above, these include antiprotons, but also gamma rays, which will be discussed later in section 4.3 in more detail.

Below we will discuss the PAMELA positron excess in terms of decaying dark matter, independently of a concrete particle-physics model. Some recent works on the indirect detection of decaying dark matter can be found in Refs. [41, 43, 48, 82, 84–88, 91, 92, 94, 95, 105, 216, 246].

Model independent analysis in terms of dark matter decay

The work presented in this section was published in Ref. [49].

In light of the PAMELA, Fermi LAT and H.E.S.S. data, we will analyze the predictions for the cosmic-ray positron fraction and the total electron plus positron flux when contributions from dark matter decay are included. To keep the analysis as model-independent as possible with respect to particle physics, we will analyze several scenarios of decaying dark matter, computing the predictions for the positron fraction and the total electron plus positron flux for either a fermionic or a bosonic particle, which decays via different channels with a branching ratio of 100%. We calculate for each of these channels the energy spectrum of electrons and positrons using the event generator PYTHIA 6.4 [247], and we compare our final results with the observations by PAMELA and Fermi LAT. Thus, from the particle-physics point of view the only free parameters are the dark matter mass and lifetime. However, from the astrophysics point of view there are a number of uncertainties, such as the choice of propagation parameters and the choice of the background fluxes of electrons and positrons, as discussed above.

As discussed above, the background to the positron flux from dark matter decay is constituted by a secondary positron flux originating from the collision of primary protons and other nuclei on the ISM. We will adopt for the background fluxes of electrons and positrons the ones corresponding to

the "Model 0" presented by the Fermi collaboration in Ref. [114], which fits well the low-energy data points of the total electron plus positron and the positron fraction. The interstellar background fluxes can be parametrized as:

$$\Phi_{e^-}^{\rm bkg}(E) = \left(\frac{82.0\,\epsilon^{-0.28}}{1+0.224\,\epsilon^{2.93}}\right)\,{\rm GeV}^{-1}\,{\rm m}^{-2}\,{\rm s}^{-1}\,{\rm sr}^{-1}\,, \tag{4.18}$$

$$\Phi_{e^+}^{\rm bkg}(E) = \left(\frac{38.4\,\epsilon^{-4.78}}{1+0.0002\,\epsilon^{5.63}}+24.0\,\epsilon^{-3.41}\right)\,{\rm GeV}^{-1}\,{\rm m}^{-2}\,{\rm s}^{-1}\,{\rm sr}^{-1}\,, \tag{4.19}$$

where $\epsilon = E/1\,{\rm GeV}$. In the energy regime between 2 GeV and 1 TeV these approximations are better than 5%. However, we will allow for a possible shift in the normalization of the background flux of electrons, k, which is dominated by primaries, due to our ignorance of the amount of electrons injected in the interstellar medium.

The production rate of particles is defined in Eq. (4.4) and a function of the energy spectrum of particles and the dark matter halo density profile. In this section we will, for definiteness, adopt the spherically symmetric Navarro-Frenk-White halo density profile [248]:

$$\rho(r) = \frac{\rho_0}{(r/r_c)[1+(r/r_c)]^2}\,, \tag{4.20}$$

with $\rho_0 \simeq 0.26\,{\rm GeV/cm}^3$ and $r_c \simeq 20$ kpc, although our conclusions are not very sensitive to the choice of the density profile. Eq. 4.20 implies a density of $\rho_\odot \simeq 0.3\,{\rm GeV\,cm}^{-3}$ at position of the Sun $R_\odot = 8.5\,{\rm kpc}$.

In our analysis we will sample several dark matter masses and treat the dark matter lifetime and the normalization of the background flux of electrons as free parameters which will be determined to provide a qualitatively good fit to the PAMELA and Fermi measurements for standard propagation models and backgrounds. In light of the large uncertainties related to the actual astrophysical electron and positron background (and in contrast to other recent work [48, 73, 74, 109]) we do not attempt to fit the data with some kind of quantitative χ^2-fits. Furthermore, we neglect the finite energy resolution of the different experiments for simplicity.[4] Note that below energies of 10 GeV

[4]For instance, for Fermi LAT the 68% (95%) containment energy width is relatively small and always $\Delta E/E \lesssim 0.2$ ($\lesssim 0.6$), except at the very highest energies [76]. This would only becomes important for very sharp spectral features and should not change our conclusions qualitatively.

the data is best fitted for normalizations $k \simeq 1$. In our plots, we always used normalization factors $1 \geq k \geq 0.8$ to leave some room for dark matter. Let us now discuss the cases of fermionic and scalar dark matter particles separately.

Fermionic dark matter decay. In the case where the dark matter particle is a fermion $\psi_{\rm DM}$, we consider the following decay channels[5]:

$$\begin{aligned} \psi_{\rm DM} &\to Z\nu \,, \\ \psi_{\rm DM} &\to W^{\pm}\ell^{\mp} \,, \\ \psi_{\rm DM} &\to \ell^{+}\ell^{-}\nu \,, \end{aligned}$$

where the three-body decay into charged leptons and a neutrino is assumed to be mediated by the exchange of a scalar particle.

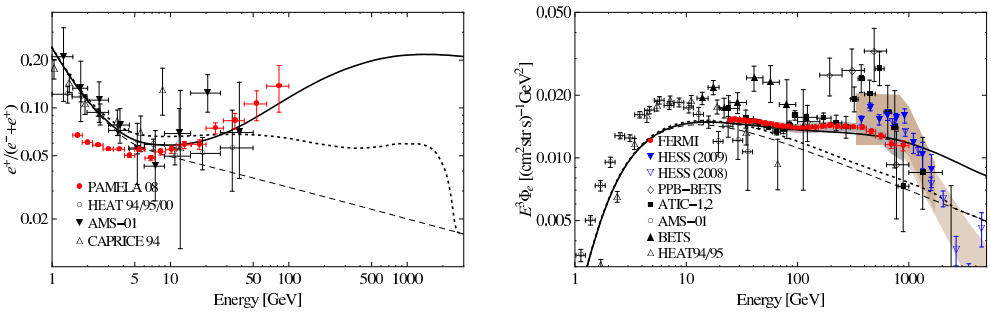

Figure 4.1: Positron fraction (*left panel*) and total electron plus positron flux (*right panel*) for the decay channel $\psi_{\rm DM} \to Z\nu$ with $M_{\rm DM} = 100\,\text{TeV}$ (solid) and 5 TeV (dotted). The dashed line shows the background fluxes as discussed in the text, the dotted line demonstrates results with minimal dark matter mass fitting the PAMELA data only. Solar modulation is taken into account using the force field approximation with $\phi_F = 550\,\text{MV}$.

The predicted positron fraction in the case where the dark matter particles decay via $\psi_{\rm DM} \to Z\nu$ is shown in the left panel of Fig. 4.1, compared to the PAMELA, HEAT, CAPRICE and AMS-01 data, for the exemplary

[5]We do not include quarks or Higgs bosons in the list, since they yield similar signatures to gauge boson fragmentation. Furthermore, we restrict our analysis to decay channels with two or three final-state particles.

dark matter masses $M_{\rm DM} = 5$ and 100 TeV. In the right panel we show the corresponding positron plus electron flux compared to the Fermi LAT and H.E.S.S. data, showing also the H.E.S.S. systematic error bands (for other data sets see above). The dark matter lifetimes and the normalization factors k of the primary electron flux have been chosen in each case to provide a reasonable fit to the PAMELA and Fermi data points (solid line) or to the PAMELA data only (dotted line, using smaller dark matter masses). In this decay channel, the only source of electrons and positrons is the fragmentation of the Z boson, which produces relatively soft particles. As a result, even though this decay mode can produce a visible excess in the positron fraction, the energy spectrum is in general too flat to explain the steep rise observed by PAMELA. An exception occurs if the dark matter mass is very large, $M_{\rm DM} \gtrsim 50\,{\rm TeV}$. In this case, the electrons and positrons from dark matter decay are boosted to high enough energies to produce the steep rise in the positron fraction. However, these large dark matter masses seem to be in conflict with the H.E.S.S. observations, which require a fall-off in the total electron plus positron spectrum at $\sim 1\,{\rm TeV}$. Note that other important constraints on this channel would actually come from the observed antiproton flux.

In Fig. 4.2 we show the predictions for the cosmic-ray electron and positron fluxes when a fermionic dark matter particle decays as $\psi_{\rm DM} \to W^{\pm}\ell^{\mp}$ for different dark matter masses, and for $\ell = e, \mu, \tau$. The electrons and positrons created in the fragmentation of the $W^{\pm}$ gauge bosons produce a rather flat contribution to the positron fraction. However, the harder electrons and positrons resulting from the decay of the $\mu^{\pm}$ and $\tau^{\pm}$ leptons or directly from the decay into $e^{\pm}$ produce a rise in the total energy spectrum and in the positron fraction, so that the PAMELA measurements can in principle be explained by these decay modes. However, the decay mode $\psi_{\rm DM} \to W^{\pm}e^{\mp}$ also produces a steep rise and a sharp fall-off in the total electron plus positron flux, which is not observed by Fermi, and is thus problematic. On the other hand, the decay mode $\psi_{\rm DM} \to W^{\pm}\tau^{\mp}$ predicts, for a wide range of dark matter masses, an electron plus positron flux that are too flat to explain the anomalies observed by PAMELA and Fermi.

On the contrary, the decay mode $\psi_{\rm DM} \to W^{\pm}\mu^{\mp}$ can nicely accommodate the PAMELA and Fermi observations when the dark matter mass is $M_{\rm DM} \simeq 3\,{\rm TeV}$ and the lifetime is $\tau_{\rm DM} \simeq 2.1 \times 10^{26}\,{\rm s}$. However, the fragmentation of the $W^{\pm}$ gauge bosons also produces fluxes of primary antiprotons

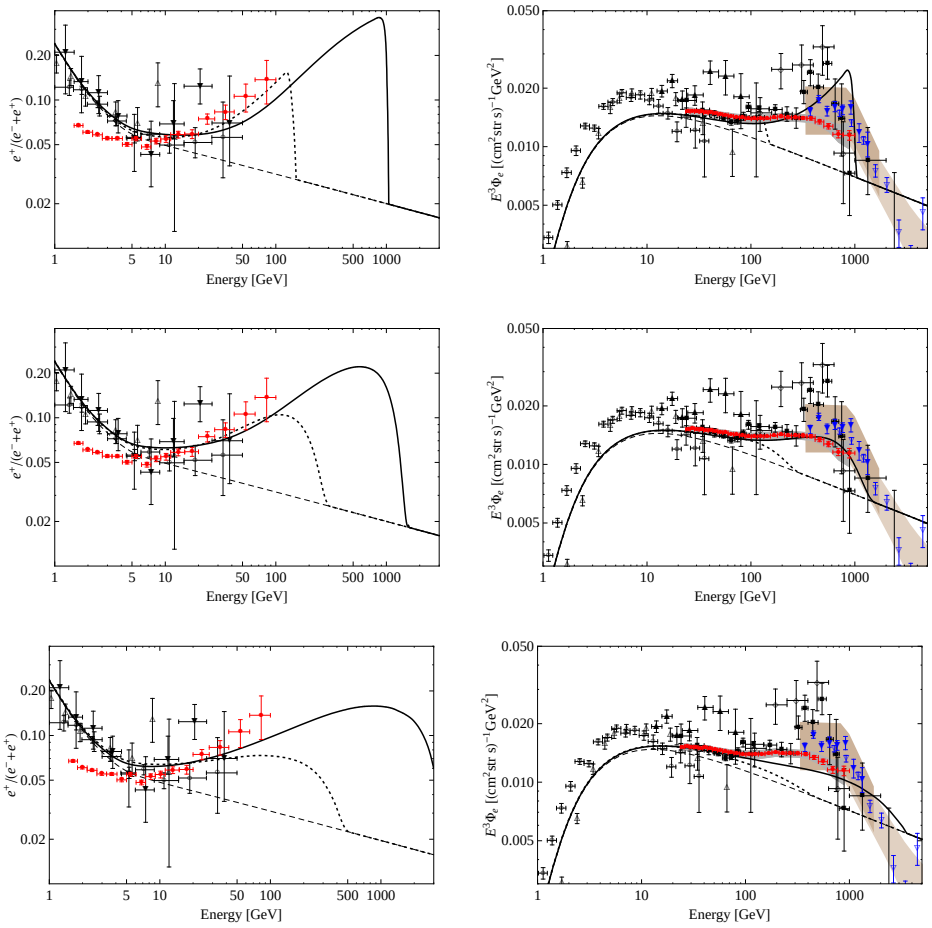

Figure 4.2: Same as Fig. 4.1, but for the decay channels $\psi_{\rm DM} \to W^\pm \ell^\mp$. *Upper panels:* $\psi_{\rm DM} \to W^\pm e^\mp$ with $M_{\rm DM} = 2000\,\text{GeV}$ (solid) and $300\,\text{GeV}$ (dotted). *Middle panels:* $\psi_{\rm DM} \to W^\pm \mu^\mp$ with $M_{\rm DM} = 3000\,\text{GeV}$ (solid) and $600\,\text{GeV}$ (dotted). *Lower panels:* $\psi_{\rm DM} \to W^\pm \tau^\mp$ with $M_{\rm DM} = 8000\,\text{GeV}$ (solid) and $1000\,\text{GeV}$ (dotted).

and gamma rays, which are severely constrained by present experiments. Figure 4.3 shows the prediction for the antiproton flux with an uncertainty band corresponding to the MAX, MED and MIN models in Tab. 4.2, compared to different measurements like PAMELA and CAPRICE (for details see above). While the absolute flux (left panel) is compatible with existing measurements, it is apparent from the figure that the $\bar{p}/p$-ratio (right panel) is in some tension with the results at the highest energies explored by

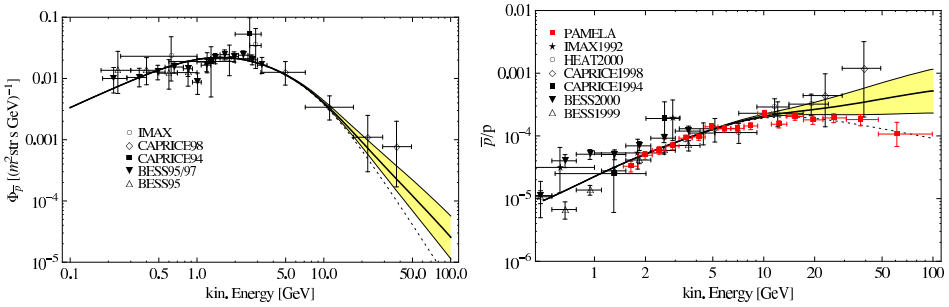

Figure 4.3: Antiproton flux (*left panel*) and the corresponding $\bar{p}/p$-ratio (*right panel*) for $\psi_{\rm DM} \to W^{\pm}\mu^{\mp}$ with $M_{\rm DM} = 3000\,{\rm GeV}$ and $\tau_{\rm DM} = 2.1 \times 10^{26}\,{\rm s}$. For the antiproton flux we adopt the background from Ref. [249], while the $\bar{p}/p$-ratio is plotted using the background from Ref. [250], and the yellow band indicates the uncertainties from the propagation model. The solid black line corresponds to the MED model of Tab. 4.2.

PAMELA [112].

The dark matter particles could also decay into three fermions, namely into a lepton-antilepton pair and a neutrino via $\psi_{\rm DM} \to \ell^+\ell^-\nu$ with $\ell = e, \mu, \tau$. In this case many possibilities could arise depending on the specific particle-physics scenario. We will just concentrate on the case where the lepton and the antilepton carry the same flavour and the decay is mediated by a heavy scalar[6]. The results for the positron fraction and the total electron plus positron flux are shown in Fig. 4.4.

The spectrum produced in the decay into electron-positron pairs and neutrinos is flatter in this case than in the two-body decay $\psi_{\rm DM} \to W^{\pm}e^{\mp}$, although it still predicts a rather prominent bump in the electron spectrum at high energies, which is not observed by Fermi. On the other hand, decays into tau flavour can also qualitatively reproduce the steep rise in the positron fraction for dark matter masses above $\sim 2.5\,{\rm TeV}$, although the resulting electron plus positron spectrum has an energy dependence much steeper than $E^{-3.0}$ at high energies, again in conflict with the Fermi measurements.

However, the decay channel $\psi_{\rm DM} \to \mu^-\mu^+\nu$ can nicely reproduce the Fermi electron plus positron spectrum and the steep rise in the positron frac-

[6]Our results are not very sensitive to the mass splitting between dark matter particle and virtual scalar.

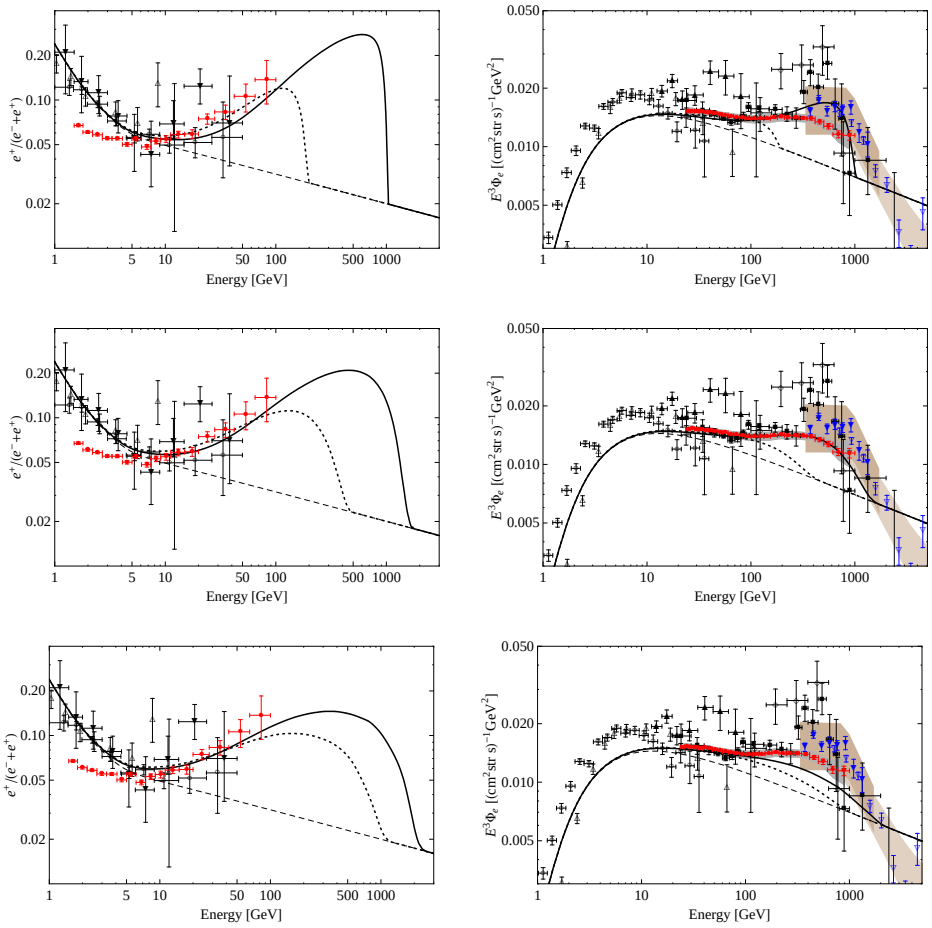

Figure 4.4: Same as Fig. 4.1, but for the decay channels $\psi_{\rm DM} \to \ell^{\pm}\ell^{\mp}\nu$. *Upper panels:* $\psi_{\rm DM} \to e^{-}e^{+}\nu$ with $M_{\rm DM} = 2000\,{\rm GeV}$ (solid) and $400\,{\rm GeV}$ (dotted). *Middle panels:* $\psi_{\rm DM} \to \mu^{-}\mu^{+}\nu$ with $M_{\rm DM} = 3500\,{\rm GeV}$ (solid) and $1000\,{\rm GeV}$ (dotted). *Lower panels:* $\psi_{\rm DM} \to \tau^{-}\tau^{+}\nu$ with $M_{\rm DM} = 5000\,{\rm GeV}$ (solid) and $2500\,{\rm GeV}$ (dotted).

tion observed by PAMELA when the dark matter mass is $M_{\rm DM} \simeq 3500\,{\rm GeV}$ and the lifetime is $\tau_{\rm DM} \simeq 1.1 \times 10^{26}\,{\rm s}$.

Note that the dark matter particle could also decay into charged fermions with different flavor simultaneously. Such a situation arises for example when the decay is mediated by the flavour-blind kinetic mixing as in the hidden $U(1)_X$ gaugino scenario, see section 4.2.3. For now, we just illustrate this case by showing in Fig. 4.5 the predictions for the positron fraction and

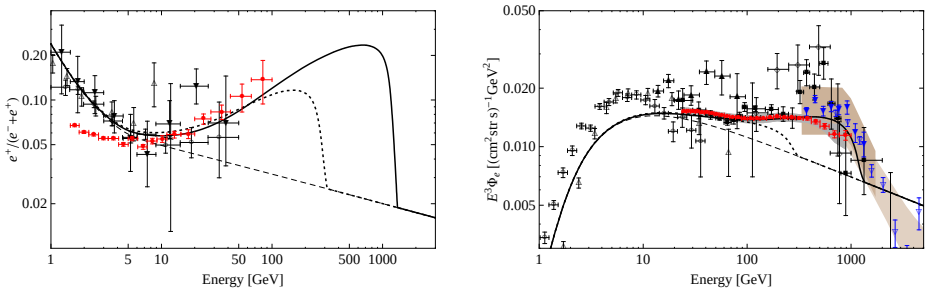

Figure 4.5: Same as Fig. 4.1, but for the democratic decay $\psi_{\rm DM} \to \ell^\pm \ell^\mp \nu$ with equal branching ratios into the three charged lepton flavours, with $M_{\rm DM} = 600\,{\rm GeV}$ (dotted) and 2500 GeV (solid).

the total electron plus positron flux when the dark matter particles perform three-body decay democratically into the three flavors. We show results for a dark matter mass of 2500 GeV (solid), which can well fit the observations, and for $M_{\rm DM} = 600\,{\rm GeV}$ (dotted).

Scalar dark matter decay. For a scalar dark matter particle, we will discuss the following decay channels[7]:

$$\begin{aligned} \phi_{\rm DM} &\to ZZ, \\ \phi_{\rm DM} &\to W^+W^-, \\ \phi_{\rm DM} &\to \ell^+\ell^-. \end{aligned}$$

In the first two cases, and as generically expected from decays into weak gauge bosons, the electrons and positrons produced are relatively soft, resulting in a positron fraction which is too flat to explain the steep rise in the spectrum observed by PAMELA, unless the mass of the dark matter particle is very high. The conclusions are similar to what we already discussed above in the fermionic dark matter case, see Fig. 4.1.

On the other hand, we show in Fig. 4.6 the predictions for the positron fraction and the total electron plus positron flux when the scalar dark matter particle decays into fermion pairs of the same generation, for dark matter masses between $M_{\rm DM} = 300\,{\rm GeV}$ and 5 TeV. The decay $\phi_{\rm DM} \to e^+e^-$ can explain the steep rise in the positron fraction observed by PAMELA, but it

[7] Again, we do not include quarks and Higgs bosons in the list. Three-body decay modes like $\phi_{\rm DM} \to \ell^+\ell^-\gamma$ are expected to give results similar to the fermionic dark matter case.

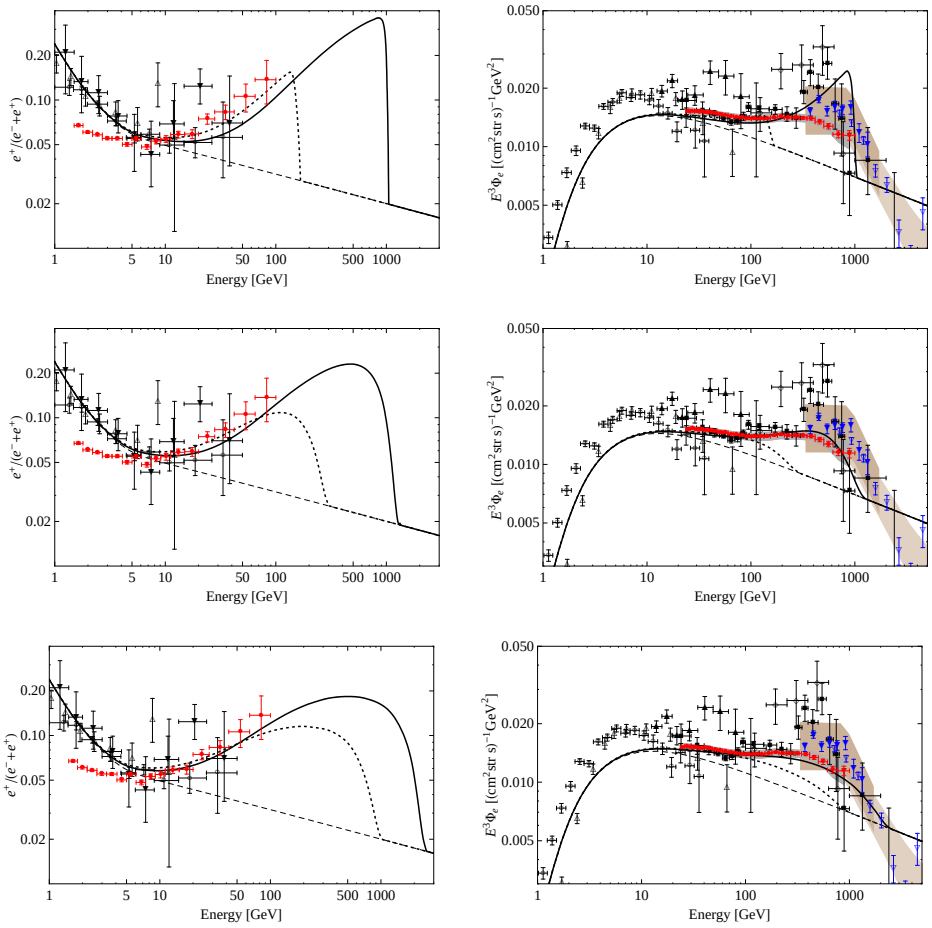

Figure 4.6: Same as Fig. 4.1, but for the decay channels $\phi_{\rm DM} \to \ell^+\ell^-$. *Upper panels:* $\phi_{\rm DM} \to e^+e^-$ with $M_{\rm DM} = 2000\,{\rm GeV}$ (solid) and $300\,{\rm GeV}$ (dotted). *Middle panels:* $\phi_{\rm DM} \to \mu^+\mu^-$ with $M_{\rm DM} = 2500\,{\rm GeV}$ (solid) and $600\,{\rm GeV}$ (dotted). *Lower panels:* $\phi_{\rm DM} \to \tau^+\tau^-$ with $M_{\rm DM} = 5000\,{\rm GeV}$ (solid) and $2000\,{\rm GeV}$ (dotted).

is apparent from Fig. 4.6 that the dark matter decay into this channel is not compatible with the Fermi LAT electron+positron data.

On the other hand, a scalar dark matter particle with a mass $M_{\rm DM} \simeq 2500\,{\rm GeV}$ and a lifetime $\tau_{\rm DM} \simeq 1.8 \times 10^{26}\,{\rm s}$, which decays exclusively into $\mu^+\mu^-$ pairs, can reproduce both the steep rise in the spectrum observed by PAMELA and the total electron plus positron spectrum measured by Fermi. The same holds true for decay into tau flavours, with $M_{\rm DM} \simeq 5000\,{\rm GeV}$ and $\tau_{\rm DM} \simeq 0.9 \times 10^{26}\,{\rm s}$.

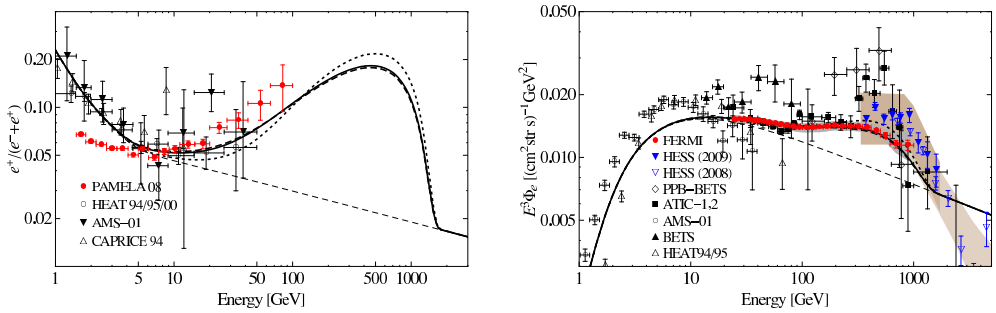

Figure 4.7: Illustration of the dependence on the choice of transport parameters. Same as Fig. 4.4, middle panels, but only for a dark matter mass of 3500 GeV. The solid, dashed and dotted lines correspond to the MED, MAX and MIN model parameters, respectively. The results for the MED and MAX model are very similar because the height of the diffusion zone becomes irrelevant above a few kpc for high-energy electrons from local sources.

Discussion. Our results for the dark matter lifetime and mass only mildly depend on the propagation model, as illustrated in Fig. 4.7 for the decay mode $\psi_{\rm DM} \to \mu^+\mu^-\nu$, where the impact of choosing other sets of propagation parameters is shown. The MED and MAX models give essentially identical results for the fluxes, only the MIN model (which has a thin diffusion zone $L = 1\,\text{kpc}$) predicts fluxes that are somewhat steeper. The impact of using different halo profiles is furthermore negligible. On the other hand, changing the slope of the primary electron background (which we kept fixed in our analysis) or the approximation made for the energy loss time τ_E (which were required for finding semi-analytical solutions of the propagation equations), could have up to an $\mathcal{O}(1)$ impact on the best-fit dark matter lifetimes, as well as impact on the best-fit mass. Since our goal was to present working reference scenarios for decaying dark matter explanations of the PAMELA positron excess, and in light of the large uncertainties related to the primary electron background, we did not attempt to quantify these uncertainties further.

We summarize our results for fermionic and bosonic dark matter scenarios which well fit the observations, together with the corresponding dark matter masses and lifetimes, in Tab. 4.3. As obvious from this table, leptonic decay, in particular the ones into second generation leptons, are strongly preferred by the data. Two- and three-body decays involving electrons in the final

Decay Channel	$M_{\rm DM}$ [GeV]	$\tau_{\rm DM}$ [10^{26}s]
$\psi_{\rm DM} \to \mu^+\mu^-\nu$	3500	1.1
$\psi_{\rm DM} \to \ell^+\ell^-\nu$	2500	1.5
$\phi_{\rm DM} \to \mu^+\mu^-$	2500	1.8
$\phi_{\rm DM} \to \tau^+\tau^-$	5000	0.9
$\psi_{\rm DM} \to W^\pm\mu^\mp$	3000	2.1

Table 4.3: Decay channels for fermionic and scalar dark matter, $\psi_{\rm DM}$ and $\phi_{\rm DM}$, respectively, that best fit the Fermi and PAMELA data. Note that the decay into $W^\pm\mu^\mp$ is in conflict with the measurements of the $\bar{p}/p$-ratio.

states produce usually a too hard spectrum, decays involving taus often a too soft spectrum. However, we also showed a flavour-democratic decay mode which nicely fits the observations. This particular decay mode is a possible prediction of hidden $U(1)_X$ gaugino decaying dark matter models, which will be discussed in detail next.

4.2.3 Hidden $U(1)_X$ gauginos and the positron excess

The work presented in this section was published in Ref. [21].

In this section, we will present predictions for cosmic-ray signatures of decaying dark matter particles in scenarios with a kinetically mixed hidden $U(1)_X$ gaugino. These scenarios are interesting, since they can give automatically rise to dominantly leptonic decay, as suggested by the PAMELA positron excess. The kinetic mixing parameter is assumed to be of the order of $\chi \sim \Theta \sim \mathcal{O}(10^{-24})$, giving rise to the required long cosmological dark matter lifetimes. This can be seen from the approximate formula

$$\tau_{X,\chi_1^0} \sim \mathcal{O}(10^{-2} - 10) \times 10^{26}\,\mathrm{s} \left(\frac{M_{X,\chi_1^0}}{100\,\mathrm{GeV}}\right)^{-1} \left(\frac{\Theta}{10^{-24}}\right)^{-2} , \qquad (4.21)$$

where the precise prefactor depends on the actual decay channel. The model and theoretical motivation is outlined in detail in section 3.3, motivation for the required tiny mixing parameters is in particular discussed in section 3.3.4.

Throughout this section we will often assume that the lightest MSSM neutralino is the LSP and the hidden gaugino is the NLSP, or vice versa. Then either the neutralino or the hidden gaugino NLSP becomes unstable

Neutralino / hidden gaugino decay modes

$M_{\chi_1^0} > M_X$	$M_{\chi_1^0} < M_X$
$\chi_1^0 \to \begin{cases} f\bar{f}\tilde{\bar{f}}^*_{L/R} \to f\bar{f}\lambda_X \\ \lambda_X h \\ \lambda_X Z \end{cases}$	$\lambda_X \to \begin{cases} f\bar{f}\tilde{\bar{f}}^{(*)}_{L/R} \to f\bar{f}\chi_i^0 \\ \chi_i^0 h \\ \chi_i^0 Z \\ \chi_j^\pm W^\mp \end{cases}$

Table 4.4: Dominant decay modes. Depending on the masses of the hidden gaugino, M_X, and the lightest neutralino, $M_{\chi_1^0}$, one of the two particles becomes unstable with a lifetime roughly given by Eq. (4.21). Since the three-body decay into fermion pairs $f\bar{f}$ is mainly mediated by virtual sfermions, $\tilde{f}^*$, we show this explicitly. Furthermore, when a sfermion is lighter than the decaying particle, the corresponding three-body decay crosses over to a cascade decay. The subsequent decay and fragmentation of the Higgs and gauge bosons, charginos and neutralinos is not shown. Note that the letter f represents any lepton or quark.

and decays into the LSP. The corresponding relevant decay modes are summarized in Tab. 4.4. Below, we will study both possible scenarios separately. In particular, we will present an analysis of the cosmic-ray predictions when the visible sector is described by a certain reference point in the mSUGRA parameter space. Our reference point will lie in the coannihilation region, which ensures a consistent cosmology in the visible sector, since all free parameters of the MSSM are fixed. Furthermore, branching ratios and hence details about dark matter decay can be calculated exactly in this fixed reference scenario, which is very convenient to illustrate typical features of the adopted model. However, we will also go beyond the mSUGRA scenario and discuss shortly how the cosmic-ray signatures can change in more general set-ups.

Decaying Neutralinos. All relevant decay modes for the case $M_X < M_{\chi_1^0}$, where the lightest neutralino can decay into the hidden gaugino, are summarized in the left part of Tab. 4.4. Beside three body decays, which produce fermion/anti-fermion pairs, we also have to take into account the decay into

M_X [GeV]	Branching Ratios for $\chi_1^0 \to$				
	$e^-e^+\lambda_X$	$\mu^-\mu^+\lambda_X$	$\tau^-\tau^+\lambda_X$	$h\lambda_X$	$Z\lambda_X$
1	28%	28%	32%	8.8%	2.6%
50	27%	27%	30%	13%	2.4%
100	24%	24%	28%	21%	2.4%
150	21%	21%	24%	32%	2.6%
200	30%	30%	36%	—	3.7%

Table 4.5: Branching ratios for the decay of a neutralino χ_1^0 into a lighter hidden gaugino λ_X, for different hidden gaugino masses M_X. In the visible sector, masses and mixing parameters are fixed by a mSUGRA scenario in the coannihilation region as described in the text. The lightest neutralino has a mass of 301 GeV. Branching ratios of three-body decays into neutrinos, $\chi_1^0 \to \nu\bar{\nu}\lambda_X$, and quarks, $\chi_1^0 \to q\bar{q}\lambda_X$, are smaller than 0.3% and 0.02%, respectively. The two-body decay into photons, $\chi_1^0 \to \gamma\lambda_X$, is one-loop suppressed and neglected.

Higgs and Z bosons. Throughout the analysis we will assume that the lightest neutralino χ_1^0 makes up the dominant part of the dark matter, $\rho_{\chi_1^0} \simeq \rho_{\rm DM}$, whereas the hidden gaugino abundance is negligible. The latter is indeed the case for the small mixing parameters $\chi \sim \mathcal{O}(10^{-24})$ that we are considering in this section, see Eq. (3.16).

As mentioned above, our exemplary *mSUGRA model* lies in the so-called coannihilation region. The defining parameters are $m_0 = 150\,\text{GeV}$, $m_{1/2} = 720\,\text{GeV}$, $A_0 = 0$, $\tan\beta = 10$ and $\text{sign}\,\mu = +1$. In this model the lightest neutralino has a mass of 301 GeV and the correct relic density to be dark matter, $\Omega h^2 \simeq 0.104$ (the mass spectrum and relic abundance were calculated with DarkSUSY 5.0.4 [251]). As typical for models in the coannihilation region, the three right-handed sleptons have masses around $304 - 307\,\text{GeV}$, close to the mass of the lightest neutralino. The left-handed sleptons have masses around 500 GeV.

For the case of our reference mSUGRA scenario, and for hidden gaugino masses between 1 and 200 GeV, the branching ratios of the dominant neutralino decay channels are summarized in Tab. 4.5. The calculations of all relevant Feynman graphs as well as the corresponding matrix elements, the phase-space integration and the diagonalization of neutralino mass matrices were done with help of FeynArts 3.4 and FormCalc 5.4 [252, 253]. Most interestingly, the overall branching ratio into charged leptonic final states

(into $\ell^+\ell^-\lambda_X$ for $\ell = e, \mu, \tau$) is never below $\sim 65\%$. Beside the small masses of the right-handed sleptons, which mediate the three-body decay, the underlying reason for the large leptonic branching ratio is the large μ-term, $\mu = 865\,\text{GeV}$ in our reference scenario, which suppresses the mixing between the bino-like lightest neutralino χ_1^0, the hidden gaugino and the higgsinos like $\sim \mathcal{O}(M_Z/\mu)$, and hence decay into higgs and gauge bosons. Furthermore, for large enough masses of the hidden gaugino, the decay into $h\lambda_X$ becomes kinematically forbidden. Note that although we present a concrete mSUGRA model for definiteness, the branching ratios shown here are typical for mSUGRA models in the coannihilation region, provided that the μ-term is large enough. If the latter is the case, three-body decays into charged leptons dominate generically over two-body decays into Higgs and gauge bosons.

To obtain the energy distribution of gamma rays, positrons and antiprotons that are produced in the neutralino decay, we used the event generator PYTHIA 6.4 [247]. From these spectra, the contribution to cosmic-ray fluxes as measurable at Earth is derived as described above in section 4.2. Note that in the plots the lifetime of the neutralino is always fixed by requiring a qualitatively good agreement with the positron fraction as measured by PAMELA. We do not attempt to fit the Fermi LAT or HESS electron plus positron data in case of our mSUGRA reference model, which would require larger dark matter masses. Instead, we consider the mSUGRA reference model as an interesting example for a fully defined model that gives naturally rise to dominantly leptonic decay modes. Scenarios with larger dark matter masses are discussed below.

Our results are shown in Fig. 4.8. We find that in principle the model can generate an observable excess in the positron fraction around $10 - 100\,\text{GeV}$ if the hidden gaugino is light with a mass $M_X \lesssim 50\,\text{GeV}$, although the predicted peak seems to rise too slowly to fully match the PAMELA data. This slow rise is due to the two-body decay into Higgs bosons, whose subsequent fragmentation produces rather soft positrons. From the lower left panel of Fig. 4.8 it is apparent that the model is compatible with the EGRET and preliminary Fermi LAT results for the extragalactic gamma-ray background up to 100 GeV.[8] Here, gamma rays with energies below $\sim 10\,\text{GeV}$ stem from the fragmentation of the Higgs boson, whereas gamma rays at higher energies mainly come from τ decay. Furthermore, as can be see from the lower

[8] We only include prompt radiation in the plots in this section, ICS radiation is neglected, see also Ref. [21]. For more details about gamma-ray observations see section 4.3.

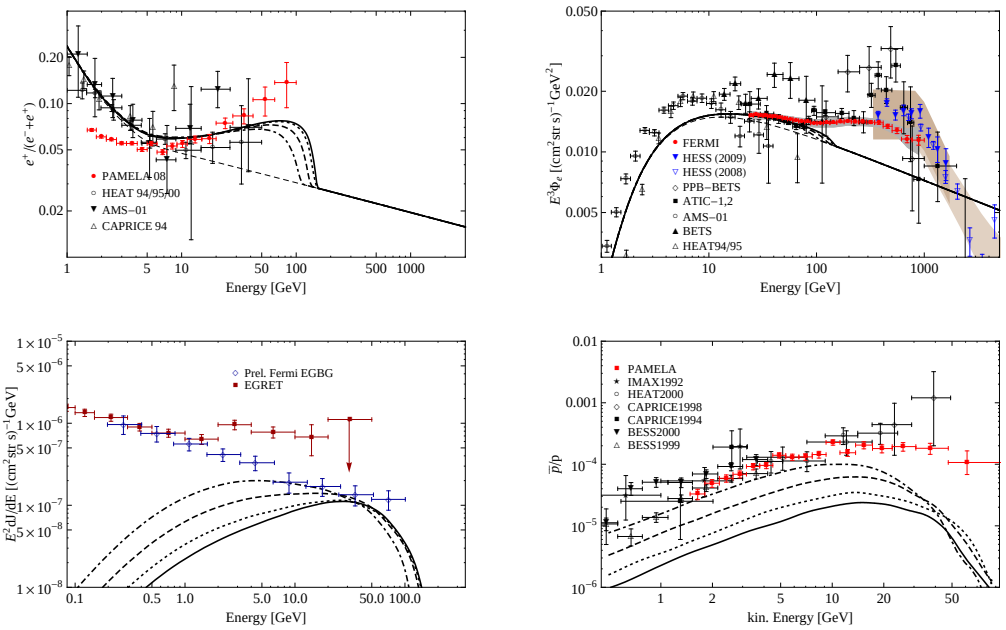

Figure 4.8: Positron fraction, total electron+positron, extragalactic gamma-ray and antiproton flux of a decaying neutralino χ_1^0 as predicted for our exemplary mSUGRA scenario. The used branching ratios are shown in Tab. 4.5. The mass of the decaying neutralino is 301 GeV, the hidden gaugino mass varies between 1 GeV (solid), 50 GeV (dotted), 100 GeV (dashed) and 150 GeV (dot-dashed). In the lower left plot, we only show the signal without astrophysical background, including prompt Galactic and extragalactic gamma rays (see below), averaged over regions with $|b| \geq 10^\circ$. In the lower right plot, we show the $\bar{p}/p$ fraction as in Fig. 4.3, but neglecting astrophysical antiprotons and only for the MED model.

right panel, the contribution to the antiproton flux is in general agreement with the observations, although it can be potentially problematic for hidden gaugino masses above ~ 100 GeV. Note however that the uncertainty in the antiproton flux at Earth from dark matter decay is of $\mathcal{O}(1)$ [176], due to our ignorance of the precise propagation parameters (*cf.* Fig. 4.3).

For different parameters of the underlying MSSM model, the above plots can mainly change in two ways. Firstly, a larger value of the μ-parameter would reduce the branching ratio into Higgs and Z bosons. As a result, the rise in the positron fraction would be steeper, and the contribution to the antiproton flux smaller. Secondly, a higher mass of the decaying neutralino

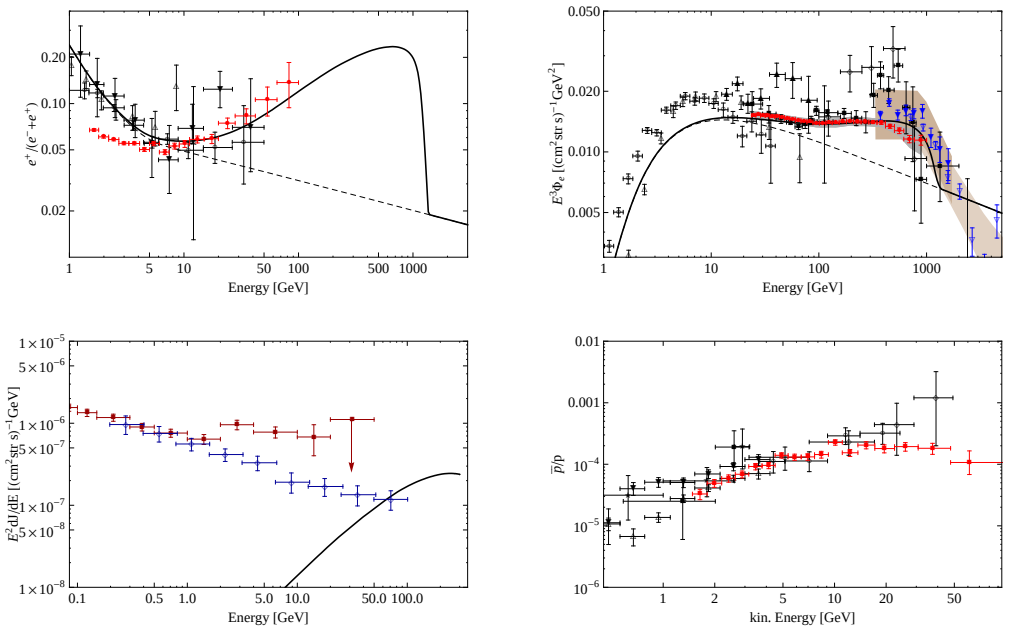

Figure 4.9: Positron fraction and total electron+positron flux for an idealized, three-body decaying bino-like neutralino with mass 2500 GeV, decaying into a light hidden gaugino.

would shift the peak to higher energies.

In Fig. 4.9 we show the results for an *idealized three-body decaying* bino-like neutralino where the mass of the neutralino is 2500 GeV, whereas the hidden gaugino has a small mass $\sim \mathcal{O}(100\,\text{GeV})$. In the plots we assume that the decay is only mediated by right-handed sleptons with a mass close to the neutralino mass, and that the decay goes entirely into $e^+e^-\lambda_X$, $\mu^+\mu^-\lambda_X$ and $\tau^+\tau^-\lambda_X$ with equal branching ratios. All other supersymmetric particles must be heavy enough to make their effects on the branching ratios negligible. Note that in any case the production and decay of taus will lead to a visible bump in the extragalactic gamma-ray flux, which is still compatible with the preliminary Fermi LAT results, but could show up in the near future at higher energies.

Although the above idealized scenario works phenomenologically, it requires some non-standard cosmology, since heavy bino-like neutralinos with masses above a few hundred GeV are typically overproduced, even when

coannihilation with sleptons is taken into account, see *e.g.* Ref. [254]. At the same time, wino- and higgsino-like lightest neutralinos do not exhibit the desired leptophilic decay.[9] However, these problems are absent if one considers scenarios where the hidden gaugino is heavier than the lightest neutralino, $M_X > M_{\chi_1^0}$. Firstly, due to the mixing with the bino, the interactions of the hidden gaugino are automatically "bino-like". Secondly, for the small mixings that we consider bounds from overproduction arguments are irrelevant.

Decaying Hidden Gauginos. We will again assume that the lightest neutralino makes up most of the dark matter, whereas the hidden gaugino contributes only a subdominant part $\rho_X \ll \rho_{\chi_1^0}$ to the overall matter density of the Universe. The production mechanism of the hidden gaugino is left unspecified and can *e.g.* proceed via inflaton decay, which is in any case very model dependent. Note that in this scenario the lifetime of the hidden gaugino can be as small as $\tau_X \sim 10^{17}\,\mathrm{s}$, the current age of the Universe, provided that its relic abundance is small enough, since cosmic-ray observations only constrain the factor ρ_X/τ_X, and not τ_X separately.

We will now show the cosmic-ray predictions for the cascade decaying hidden gaugino scenario in case of our reference mSUGRA model. Depending on the mass of the hidden gaugino its decay can produce fermions, neutralinos, charginos, Higgs and gauge bosons as depicted in the right part of Tab. 4.4. For hidden gaugino masses between 600 and 1600 GeV, the corresponding branching ratios are summarized in Tab. 4.6, where we do not show the subsequent decays of the neutralinos $\chi^0_{2,3,4}$ and charginos $\chi^\pm_{1,2}$ for simplicity.[10]

As apparent from Tab. 4.6, the decay into charged lepton/slepton pairs is dominant in the whole considered mass range. The decay into quarks is suppressed by the large squark masses, $m_{\tilde{q}} \gtrsim 1.1\,\mathrm{TeV}$, whereas decay into h, Z and $W^\pm$ bosons is mainly suppressed by the small mixing between higgsinos and the hidden gaugino. However, this mixing can become enhanced when

[9] Winos only couple to left-handed sleptons, which are typically heavier than the right-handed ones, whereas higgsinos can easily decay into the Higgs boson.

[10] These subsequent decays are taken into account in our calculations. We singled out the dominant decay modes in our reference mSUGRA model and used them in the PYTHIA code: $\lambda_X \to h\chi_4^0$, $\lambda_X \to Z\chi_3^0$, $X \to W^\mp\chi_2^\pm$, $\chi_3^0 \to \chi_1^0 Z$, $\chi_4^0 \to \chi_1^0 h$ and $\chi_2^\pm \to \chi_1^\pm Z(28\%)$, $\chi_1^\pm h(27\%)$, $\chi_2^0 W^\pm(36\%)$. The decay of χ_2^0 and $\chi_1^\pm$ only produces leptons and is neglected.

M_X [GeV]	Branching Ratios for $\lambda_X \to$					
	$\nu\tilde{\nu}$	$l\tilde{l}$	$q\tilde{q}$	$h\chi_i^0$	$Z\chi_i^0$	$W^\pm\chi_i^\mp$
600	1.8%	98.2%	—	0.1%	0.0%	—
700	5.6%	92.9%	—	0.6%	0.0%	0.9%
800	5.6%	84.6%	—	3.5%	0.2%	6.1%
850	0.7%	49.8%	—	17.3%	1.2%	31.0%
900	15.3%	53.7%	—	10.7%	0.9%	19.4%
1000	14.1%	81.1%	—	1.4%	1.0%	2.4%
1200	13.3%	76.8%	—	2.7%	2.5%	4.7%
1400	13.2%	74.1%	1.6%	2.9%	2.8%	5.4%
1600	12.5%	68.5%	8.4%	2.7%	2.7%	5.2%

Table 4.6: Branching ratios of the dominant decay modes of a hidden gaugino that is cascade-decaying into the MSSM particle zoo. The underlying scenario is our chosen mSUGRA reference point as described in the text. The decay into neutrinos and charged leptons is essentially democratic in all three flavours.

the masses of the higgsinos become comparable to the mass of the hidden gaugino, which happens around $M_X \sim 870\,\text{GeV}$, see Tab. 4.6.

Our results for the cosmic-ray fluxes are shown in Fig. 4.10 for some exemplary masses between 600 GeV and 1200 GeV, where we adjusted the lifetime of the hidden gaugino again to fit the PAMELA data. For all masses of the hidden gaugino that we consider, the predictions for the positron fraction are in qualitatively good agreement with the PAMELA data. At the same time, the contribution to the antiproton flux lies well below the measurements and hence is safe in all cases. Furthermore, we obtain sizeable contributions to the extragalactic gamma-ray flux, which are mainly due to τ decays. They are marginally consistent with the preliminary Fermi LAT results for the EGBG and could show up in the near future at higher energies. However, the total electron plus positron flux exhibits a sharp step, which comes from the direct decay into e^+e^--pairs, and which is not seen in the Fermi LAT/HESS data, making this scenario problematic.

Discussion. Kinetically mixed hidden $U(1)_X$ gauginos can give rise to leptophilic dark matter decay, which was shown both for decaying hidden gauginos and decaying neutralinos in a reference mSUGRA model. A central points in this setup is that our mSUGRA model lies in the coannihilation

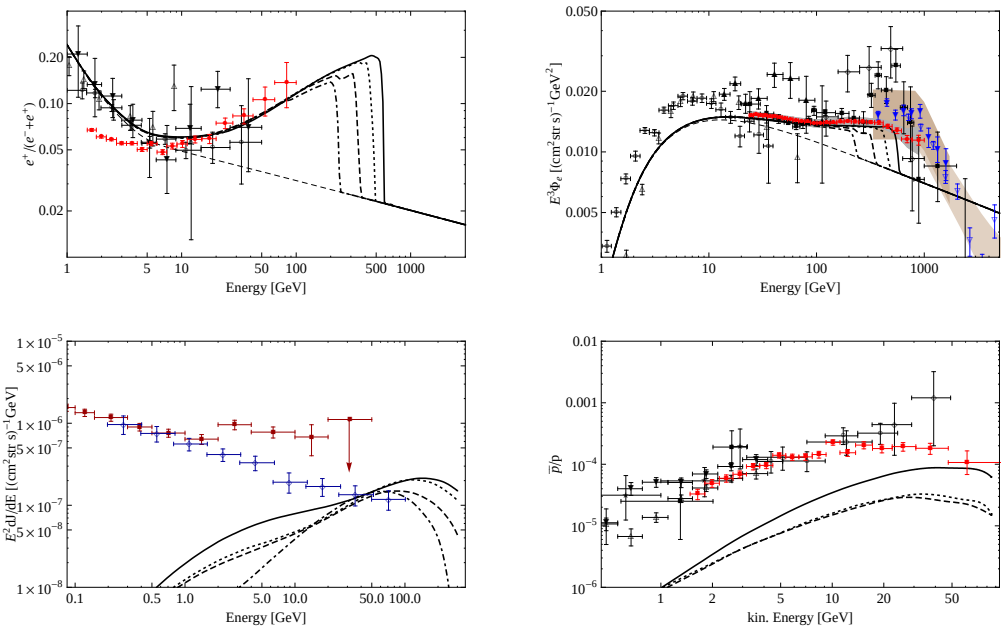

Figure 4.10: Positron fraction, extragalactic gamma-ray flux, antiproton flux and total electron + positron flux from the decay of a hidden gaugino as predicted by our mSUGRA scenario. The branching ratios are shown in Tab. 4.6. The mass of the hidden gaugino varies between 600 GeV (solid), 800 GeV (dotted), 1000 GeV (dashed) and 1200 GeV (dot-dashed).

region, which typically features very light right-handed sleptons as necessary for three-body decay into leptons when the hidden gaugino is light. Another important point is the relatively high mass of the squarks as necessary for suppressing two-body decay into quark pairs in cases where the hidden gaugino is heavy.

In case of the cascade-decaying heavy hidden gaugino a sharp step is predicted in the electron plus positron spectrum at energies of half the dark matter mass, see Fig. 4.10. This sharp step is a generic prediction of the model but problematic phenomenologically, since it is not seen by Fermi LAT or HESS. On the other hand, one can find idealized (though cosmologically problematic) scenarios with three-body decaying very heavy binos, like the one shown in Fig. 4.9, which well fit the data. In any case a sizeable contribution to the gamma-ray fluxes is predicted, which comes mainly from the tau decay, and which is only barely compatible with current preliminary

Fermi LAT results for the EGBG and hence could show up or be excluded in future data releases. Details about gamma-rays from decaying dark matter will be discussed in the next section.

4.3 Gamma Rays from Dark Matter Decay

The observation of gamma-rays is radically different from observations of other cosmic-ray species, since they propagate on straight trajectories and are not absorbed on Galactic scales. Hence, gamma rays carry information about the spatial distribution of their sources, and they could contain narrow lines in the energy spectrum if they are produced by exotic sources like dark matter. Gamma rays are an invaluable channel for the indirect detection of dark matter.

In this section we will discuss gamma-ray signals from decaying dark matter in some detail. In subsection 4.3.1 we will shortly discuss the different dark matter related sources of Galactic and extragalactic gamma rays and in subsection 4.3.2 we will discuss where in the sky these gamma rays are expected to show up. In subsection 4.3.3, we will then discuss the dipole-like anisotropy of the prompt halo component of the gamma rays from decaying dark matter as tool to distinguish it from the EGBG, and give predictions for the dark matter scenarios that we found above can explain the PAMELA positron excess.

Part of the work presented in this section was published in Ref. [54].

4.3.1 The different gamma-ray components

Gamma rays can be produced directly by the dark matter decay itself (as prompt radiation), or indirectly by inverse Compton scattering of electrons and positrons from dark matter decay on the interstellar or extragalactic radiation field. We will outline both production mechanisms below.[11]

The *prompt radiation* from dark matter decay can be divided in two components. The first one stems from the decay of dark matter particles

[11] A third source of gamma rays is Bremsstrahlung of electrons and positrons from dark matter decay due to their interaction with the ISM. This component is negligible in all practical cases and will be neglected in the subsequent discussion.

inside the Galactic halo and reads

$$\frac{dJ_{\rm halo}}{dE_\gamma}(l,b) = \frac{1}{4\pi\, M_{\rm DM}\, \tau_{\rm DM}} \frac{dN_\gamma}{dE_\gamma} \int_0^\infty ds\; \rho_{\rm halo}[r(s,l,b)]\;, \tag{4.22}$$

where dN_γ/dE_γ is the energy spectrum of gamma rays produced in the decay of a dark matter particle and $\rho_{\rm halo}(r)$ is the density profile of dark matter particles in our Galaxy, as a function of the distance from the Galactic center r. The received gamma-ray flux depends on the Galactic coordinates, longitude l and latitude b, and is given by a line-of-sight integral over the parameter s, which is related to r by

$$r(s,l,b) = \sqrt{s^2 + R_\odot^2 - 2sR_\odot \cos b \cos l}\;. \tag{4.23}$$

Here, $R_\odot = 8.3\,{\rm kpc}$ denotes the distance of the Sun to the Galactic center [255].

Uncertainties of this Galactic component come mainly from the uncertainties of the actual halo profile $\rho_{\rm halo}(r)$ and the exact determination of the local dark matter density $\rho_\odot$. The latest N-body simulations favor the Einasto density profile [53, 256, 257]

$$\rho_{\rm halo}^{\rm Einasto}(r) \propto \exp\left[-\frac{2}{\alpha}\left(\left(\frac{r}{r_s}\right)^\alpha - 1\right)\right]\;, \tag{4.24}$$

which we will use throughout this section when not stated otherwise, and for which we adopt $\alpha = 0.17$ and the scale radius $r_s = 20\,{\rm kpc}$. For comparison we will also show results for the much shallower isothermal profile

$$\rho_{\rm halo}^{\rm isothermal}(r) \propto \frac{1}{r^2 + r_s^2} \tag{4.25}$$

with $r_s = 3.5\,{\rm kpc}$. In this section we use the local dark matter density as determined in Ref. [258], $\rho_\odot = 0.385\,{\rm GeV\,cm^{-3}}$, to normalize the profiles at the position of the Sun.[12]

In addition to the gamma-ray fluxes that originate from the decay of dark matter particles in the Galactic halo, there exists a largely isotropic contribution generated by the prompt radiation of decays of dark matter particles

[12]Note that this normalization, and the Sun's position, differs somewhat from the parameters we that adopted in the preceding sections, see Eq. (4.20).

at cosmological distances. The corresponding gamma-ray flux received at Earth is given by

$$\frac{dJ_{\rm eg}}{dE_\gamma} = \frac{\Omega_{\rm DM}\rho_{\rm c}}{4\pi M_{\rm DM}\tau_{\rm DM}} \int_0^\infty dz \frac{1}{H(z)} \frac{dN_\gamma}{dE_\gamma}\left[(z+1)E_\gamma\right] \, e^{-\tau(E_\gamma,z)} \,, \qquad (4.26)$$

where $H(z) = H_0\sqrt{\Omega_\Lambda + \Omega_{\rm m}(z+1)^3}$ is the Hubble expansion rate as a function of redshift z, and $\rho_{\rm c} = 5.5 \times 10^{-6}\,{\rm GeV/\,cm^3}$ denotes the critical density of the Universe.

In Eq. (4.26) we included an attenuation factor for the gamma-ray flux, which incorporates the effects of electron-positron pair production by collisions of gamma rays from dark matter decay with the extragalactic background light emitted by galaxies in the ultraviolet, optical and infrared frequencies [259]. The attenuation factor is determined by the optical depth $\tau(E_\gamma, z)$, for which we will use the results from Ref. [260].[13] In Fig. 4.11 we show isocontours of the optical depth in the redshift vs. energy plane. It is apparent from the plot that gamma rays with high energies around 1 TeV are strongly attenuated and come mainly from redshifts $z \lesssim 0.05$. On the other hand, the flux of gamma rays originating from the decay of dark matter particles in the Galactic halo is barely attenuated by pair production on the ISRF at energies below 10 TeV [262].

As mentioned above, electrons and positrons produced in the dark matter decay also generate a contribution to the total gamma-ray flux through their *inverse Compton scattering* on the interstellar radiation field (ISRF), which includes the CMB, thermal dust radiation and starlight. Recently, ICS radiation in connection with the PAMELA excess was discussed in Refs. [63–68]; a pedagogical review can be found in Ref. [263]. Furthermore, we mention that the interactions of energetic electrons and positrons with the Galactic magnetic field produce synchrotron radiation in the radio band with frequencies $\mathcal{O}(0.1-100\,{\rm GHz})$, which could also be observed (see *e.g.* Ref. [264, 265]). Here we will shortly review the basics formulas relevant for the calculation of inverse Compton scattering radiation.

The production rate of gamma rays with energy E_γ at the position $\vec{r}$ of the Galaxy, due to inverse Compton scattering of dark matter electrons

[13] In Ref. [260] the optical depth is calculated for redshifts $z < 5$. Following Ref. [261], we assume that the optical depth does not increase beyond $z = 5$ and set $\tau(E_\gamma)_{z>5} = \tau(E_\gamma)_{z=5}$.

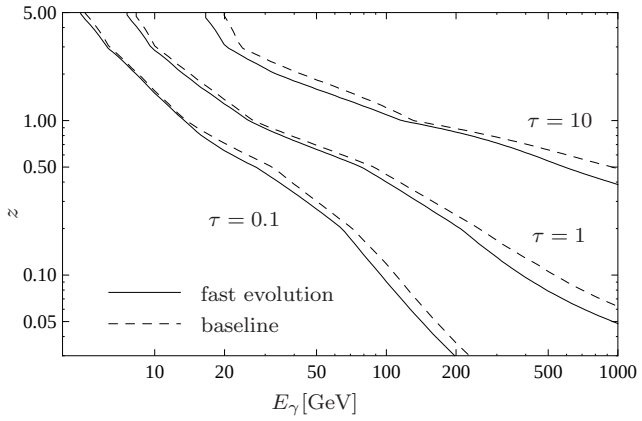

Figure 4.11: Isocontours of the optical depth $\tau(E_\gamma, z)$ of gamma-ray photons, emitted at redshift z and observed at Earth with energy E_γ. We show results for two different models of the intergalactic background light [260]. Throughout this work, we will adopt the "fast evolution" model.

(or positrons) with number density $n_{e^\pm}(E_e, \vec{r})$ on photons of the ISRF with number density $n_{\rm ISRF}(\epsilon, \vec{r})$, is given by

$$\frac{dR_\gamma^{\rm IC}(\vec{r})}{dE_\gamma} = \int_0^\infty d\epsilon \int_{m_e}^\infty dE_e \, \frac{d\sigma^{\rm IC}(E_e, \epsilon)}{dE_\gamma} n_{e^\pm}(E_e, \vec{r}) n_{\rm ISRF}(\epsilon, \vec{r}) \, . \tag{4.27}$$

Here, $d\sigma^{\rm IC}/dE_\gamma$ denotes the differential cross-section of inverse Compton scattering of an electron with energy E_e, where an ISRF photon with energy ϵ is up-scattered to energies between E_γ and $E_\gamma + dE_\gamma$. It can be derived from the Klein-Nishina formula and is given by

$$\frac{d\sigma^{\rm IC}(E_e, \epsilon)}{dE_\gamma} = \frac{3}{4} \frac{\sigma_{\rm T}}{\gamma_e^2 \, \epsilon} \left[2q \ln q + 1 + q - 2q^2 + \frac{1}{2} \frac{(q\Gamma)^2}{1 + q\Gamma} (1 - q) \right] , \tag{4.28}$$

where $\sigma_{\rm T} = 0.67\,{\rm barn}$ denotes the Compton scattering cross section in the Thomson limit, $\gamma_e \equiv E_e/m_e$ is the Lorentz factor of the electron, $m_e = 511\,{\rm keV}$ is the electron mass, and we have defined $\Gamma \equiv 4\gamma_e \epsilon / m_e$ and $q \equiv E_\gamma / \Gamma(E_e - E_\gamma)$. Eq. (4.28) holds in the limit where $\epsilon, m_e \ll E_e$, and kinematics and the neglect of down-scattering require that $\epsilon \leq E_\gamma \leq (1/E_e +$

$1/4\gamma_e^2\epsilon)^{-1} \equiv E_\gamma^{\max}$.[14] The gamma-ray flux from ICS that is received at Earth reads then

$$\frac{dJ_{\text{halo-IC}}}{dE_\gamma}(l,b) = 2 \cdot \frac{1}{4\pi} \int_0^\infty ds \, \frac{dR_\gamma^{\text{IC}}[r(s,l,b)]}{dE_\gamma} \,, \tag{4.29}$$

where the factor of 2 takes into account the fact that both dark matter electrons and positrons contribute equally to the total flux of gamma rays.

For the number density of ISRF photons we will use results from Ref. [267]. The number density of electrons and positrons follows in principle from the diffusion equations as discussed above in section 4.2.1. However, the calculations can be simplified when it is taken into account that at higher energies above a few 10 GeV the transport equation is dominated by the energy loss terms. Then, diffusion and particle motion can be neglected in first approximation and the number density of electrons and positrons is simply given by

$$n_{e^\pm}(E_e, \vec{r}) = \frac{1}{b(E_e, \vec{r})} \frac{\rho_{\text{halo}}(\vec{r})}{M_{\text{DM}}\,\tau_{\text{DM}}} \int_{E_e}^\infty d\tilde{E}_e \, \frac{dN_{e^\pm}}{d\tilde{E}_e} \,. \tag{4.30}$$

Here, $b(E_{\text{e}}, \vec{r})$ accounts for the energy losses and contains a part that comes from ICS on the ISRF, and a part that comes from synchrotron losses in the Galactic magnetic field, $b = b_{\text{ICS}} + b_{\text{syn}}$.[15] We set $n_{e^\pm} = 0$ outside of the diffusion zone, which we model by a cylinder of half-height $L = 3\,\text{kpc}$ and radius $R = 20\,\text{kpc}$.[16] The part of the energy loss that is due to ICS is given by

$$b_{\text{ICS}}(E_e, \vec{r}) = \int_0^\infty d\epsilon \int_\epsilon^{E_\gamma^{\max}} dE_\gamma \, (E_\gamma - \epsilon) \, \frac{d\sigma^{\text{IC}}(E_e, \epsilon)}{dE_\gamma} f_{\text{ISRF}}(\epsilon, \vec{r}) \,. \tag{4.31}$$

For electron energies $E_e = 1\,\text{GeV}$, b_{ICS} ranges between $4.1 \times 10^{-17}\,\text{GeV}\,\text{s}^{-1}$ and $1.9 \times 10^{-15}\,\text{GeV}\,\text{s}^{-1}$, depending on $\vec{r}$. At higher energies b_{ICS} approxi-

[14] In the calculations we assume that the photon and electron fields are isotropic. However, taking into account the anisotropy of the photons, which are mainly produced in the Galactic disk, would give $\mathcal{O}(10\% - 20\%)$ corrections to the ICS fluxes [266].

[15] Note that, in contrast to the semi-analytical treatment in section 4.2.1, we here use a non-approximated expression for the energy-loss rate.

[16] For some sample decay channels we have cross-checked with GalProp v50p, using appropriately modified versions of the model 50p_599278 and of the annihilation package, that the adopted approximations give correct ICS gamma-ray sky maps at the 30% level everywhere in the sky for gamma-ray energies above 1 GeV. Good agreement was obtained when setting $L = 3\,\text{kpc}$ in our calculations.

mately scales like $\sim E_e^2$. On the other hand, the synchrotron loss part reads

$$b_{\rm syn}(E_e, \vec{r}) = \frac{4}{3}\sigma_{\rm T}\gamma_e^2\frac{B^2}{2}\,, \tag{4.32}$$

where $B^2/2$ is the energy density of the Galactic magnetic field, and we set $B = 6\,\mu{\rm G}\exp(-|z|/5\,{\rm kpc} - r/20\,{\rm kpc})$ for definiteness [264]. At position of the Sun this yields an energy loss of $b_{\rm syn} \simeq 4.0\times10^{-17}(E_e/\,{\rm GeV})^2\,{\rm GeV\,s^{-1}}$. Substituting Eq. (4.30) into Eq. (4.27), the flux from inverse Compton scattering of dark matter electrons and positrons on the Galactic radiation field can be calculated.

The extragalactic part of the ICS radiation from dark matter electrons and positrons is expected to come mainly from scattering on the CMB [64]. Note that there is a similar component that comes from electrons and positrons produced in the Milky Way halo, but outside of the diffusion zone (see Ref. [65] for the analogous case of annihilation). For dark matter particles with masses below $3-5\,{\rm TeV}$ these components are all expected to become relevant only for gamma-ray energies $E_\gamma \lesssim 10\,{\rm GeV}$ and will be neglected subsequently. Note, however, that this radiation is essentially isotropic and would somewhat reduce the overall anisotropy of the ICS radiation, which will be discussed below, at these lower energies.

4.3.2 Where to look for decaying dark matter

We will now briefly discuss in which part of the sky the different components of the gamma-ray signals from dark matter decay can be potentially best observed. To this end, we will make use of signal-to-noise and signal-to-background skymaps.

To start, we first compare the sizes and angular distribution of the halo and the extragalactic component of the prompt radiation from decaying dark matter. We show in Fig. 4.12 the predicted photon flux from dark matter decay as a function of the angular distance ψ from the Galactic center. In this figure it is assumed that dark matter decays like $\psi_{\rm DM}\to\nu\gamma$, producing a monoenergetic photon with an energy in the range $E'_\gamma \simeq 10\,{\rm GeV} - 1\,{\rm TeV}$.

As apparent from the figure, the cosmological contributions decrease with energy due to attenuation effects (inelastic scattering between the intergalactic background light and the prompt gamma rays, see above), while the radiation profile from decaying particles in the halo is independent of energy.

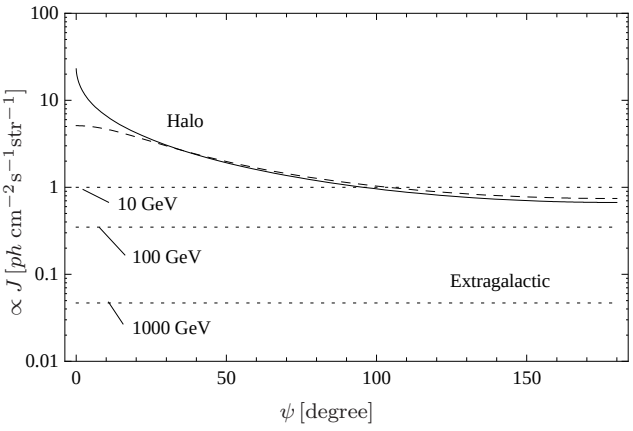

Figure 4.12: Angular profile of the gamma-ray signal from dark matter decay as function of the angle ψ to the center of the Galaxy. The *solid* (*dashed*) line shows the contribution from decay in the Milky Way halo, assuming the Einasto (isothermal) profile. Extragalactic contributions are shown in *dotted* lines for the case that dark matter decay produces a monoenergetic line with energies between $E'_\gamma = 10$ and 1000 GeV. The fluxes are integrated over energy and normalized to the size of the extragalactic component when absorption is neglected.

The halo contribution typically dominates the total flux independently of the halo profile, except at low energies $E'_\gamma \lesssim 10\,\mathrm{GeV}$ in the hemisphere pointing to the direction of the Galactic anticenter. The differences in the two dark matter profiles become only relevant near the Galactic center when $\psi \lesssim 10°$, and at the Galactic center the flux predicted for the Einasto profile is almost one order of magnitude larger than the corresponding flux from the isothermal profile.

In general, signal-to-noise ratios quantify the significance of a signal against statistical noise. The signal-to-noise ratio S/N of a dark matter signal with respect to the background is given by

$$\frac{S}{N} = \frac{N_{\gamma,\mathrm{s}}}{\sqrt{N_{\gamma,\mathrm{s}} + N_{\gamma,\mathrm{bg}}}}\ , \tag{4.33}$$

where $N_{\gamma,\mathrm{s}}$ and $N_{\gamma,\mathrm{bg}}$ denote the number of detected signal and background photons, respectively, that are observed in a given sky region $\Delta\Omega$ and energy band $E_\gamma = E_0 \ldots E_1$. Signal photons are all photons from dark matter decay,

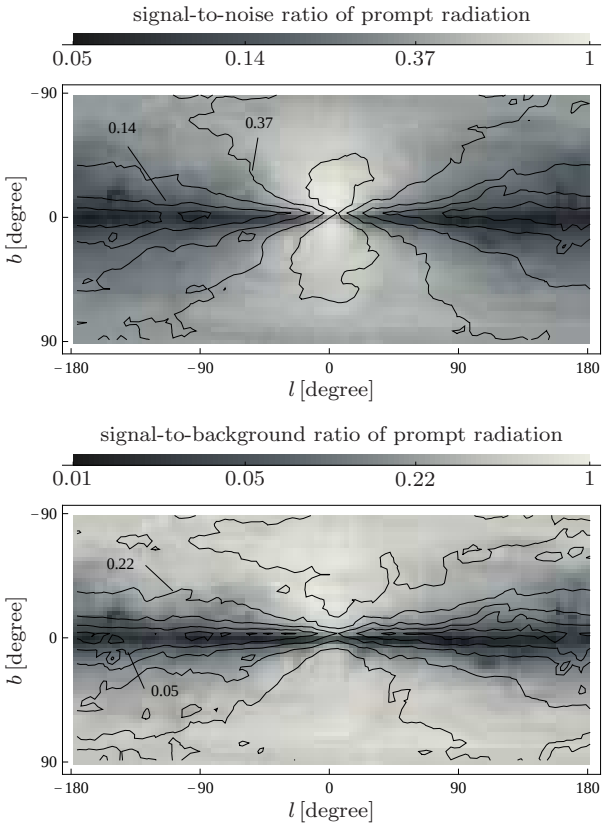

Figure 4.13: *Upper panel:* Relative signal-to-noise ratio of gamma-ray signal from dark matter decay as a function of the Galactic longitude l and latitude b, normalized to one at the Galactic center. *Lower panel:* Relative signal-to-background ratio for the same process. ICS radiation is neglected, and as background we take the predictions of the conventional GalProp model at 100 GeV.

background photons are in principle all other observed photons, including the astrophysical part of the EGBG and the Galactic foreground. Since the number of detected photons scales like $N_{\gamma,i} \propto \int_{\Delta\Omega} d\Omega \int_{E_0}^{E_1} dE\, dJ_i/dE_\gamma \equiv \Delta\Omega\, \bar{J}_i$, the signal-to-noise ratio in the limit $\Delta\Omega \to 0$ is proportional to

$$\frac{S}{N} \propto \frac{\bar{J}_\mathrm{s}}{\sqrt{\bar{J}_\mathrm{s} + \bar{J}_\mathrm{bg}}}\,, \tag{4.34}$$

where $\bar{J}_\mathrm{s}$ and $\bar{J}_\mathrm{bg}$ denote the appropriately averaged and integrated signal

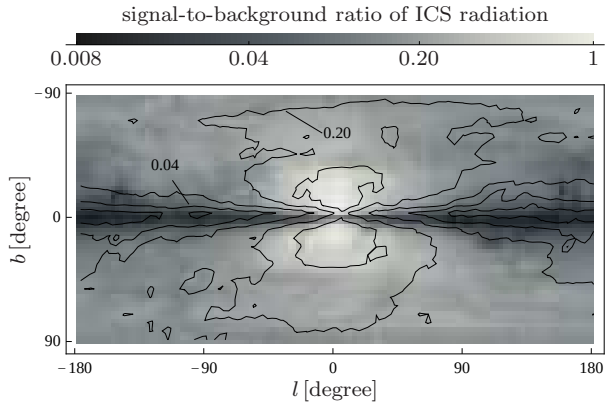

Figure 4.14: Relative signal-to-background ratio of pure ICS radiation from dark matter decay at $E_\gamma = 10\,\mathrm{GeV}$. We assume that $M_{\mathrm{DM}} = 1\,\mathrm{TeV}$ and that the dark matter is decaying into e^+e^- pairs. As background we take the fluxes from the conventional GalProp model.

and background gamma-ray fluxes, respectively.

In the upper panel of Fig. 4.13 we plot the relative signal-to-noise ratio (with arbitrary normalization), assuming that the background completely dominates the signal, $\bar{J}_{\mathrm{s}} \ll \bar{J}_{\mathrm{bg}}$, and neglecting ICS and extragalactic radiation. As background we take the predictions of the conventional GalProp model at $E_\gamma = 100\,\mathrm{GeV}$ (from Ref. [56], see below), but the results do not change qualitatively for other energies. It is apparent that, from the perspective of statistical noise, the sky regions that are most sensitive to decaying dark matter signals lie close above and below the Galactic center, with say $|l| \lesssim 25^\circ$ and $5^\circ \lesssim |b| \lesssim 35^\circ$.

To determine the best observational strategy in light of the systematics that are related to the determination of the Galactic foreground, it is more useful to consider the signal-to-background ratio $J_{\mathrm{s}}/J_{\mathrm{bg}}$ (we assume that systematic uncertainties scale roughly like $\sim J_{\mathrm{bg}}$). We show the signal-to-background ratio as a function of the Galactic coordinates in the lower panel of Fig. 4.13. It is apparent that concerning systematics the best strategy is to avoid regions near the Galactic plane and to observe fluxes only at higher latitudes, $|b| \gtrsim 20^\circ$. However, at these high latitudes also the EGBG is expected to dominate, making it possible that an exotic contribution from dark matter decay could be misidentified as part of the EGBG. Note that

furthermore an anisotropy of the dark matter flux as function of l, with largest fluxes at smaller values of $|l|$, is clearly visible in the plot. This anisotropy will be used in the next section as a method to distinguish between the completely isotropic EGBG and gamma rays from dark matter decay.

In contrast to prompt gamma rays that come directly from the dark matter decay itself, the gamma rays that stem from inverse Compton scattering of dark matter positrons or electrons on the ISRF are mostly coming from the region near the Galactic center. This can be seen in Fig. 4.14, where we plot the signal-to-background ratio of the pure ICS signal of dark matter decaying into an e^+e^- pair (with $M_{\rm DM} = 1\,\text{TeV}$) as a function of the Galactic coordinates. The gamma-ray energy is $E_\gamma = 10\,\text{GeV}$ in this plot. As background we again use the predictions from the conventional GalProp model. From the figure it is apparent that the relative size of the signal peaks at regions very close below and above the Galactic center, with $|l| \lesssim 20^\circ$ and $5^\circ \lesssim |b| \lesssim 30^\circ$. This suggests that concentrating the observation on these regions is most promising for the search for ICS radiation from dark matter decay. However, in light of the large underlying uncertainties related to the predictions of ICS radiation we will neglect these subtleties, and we consider ICS radiation only in how far it affects the anisotropies and fluxes in the sky regions that are most promising for the search for prompt gamma rays (see Ref. [70] for the opposite approach).

4.3.3 The dipole-like anisotropy

As shown in the previous section, the decay of dark matter particles can produce gamma rays that could be detected as an exotic contribution to the diffuse extragalactic gamma-ray background. The diffuse extragalactic background at high energies is believed to be dominated by the emission from unresolved point sources like active galactic nuclei and is expected to approximately follow a simple power law, with an intensity and index that has to be determined by fitting to the data [58, 59, 61]. Thus, if dark matter particles decay at a sufficiently fast rate, one generically expects to observe a deviation from a simple power law in the gamma-ray energy spectrum, which could show up in experiments like Fermi LAT.

A complementary signature of dark matter decay is the observation of anisotropies in the EGBG. It is well known that the offset between Sun and Galactic center causes a peculiar angular dependence in the gamma-ray signal from dark matter decaying [41] (or annihilating [143, 268]) in the

Milky Way halo, even if the halo profile itself is isotropic. The halo signal is largest in direction of the Galactic center and smallest in direction of the Galactic anticenter (*cf.* Fig. 4.12). The observation of an anisotropy that is aligned in this way would be a strong signal for a possible contribution from dark matter, and, on the other hand, its non-observation could provide important constraints. Gamma rays from the decay of dark matter particles at cosmological distances are isotropic and tend to reduce the anisotropy of the overall signal. This attenuation effect is however always small, due to the relative weakness of the extragalactic component.

From the theoretical point of view, the search for anisotropies in the gamma-ray flux is a cleaner method for the indirect detection of dark matter than the search for an excess in the spectrum of the EGBG. As mentioned above, the genuinely extragalactic flux from active galactic nuclei and other extragalactic sources is very poorly understood. Thus, it is difficult to make firm predictions for the total gamma-ray flux in scenarios with decaying dark matter, even when the particle-physics model is specified (namely, the dark matter mass, lifetime and decay modes). Moreover, there are other potentially important isotropic contributions to the total flux with an intensity that cannot be predicted theoretically. For instance, interactions of high energy cosmic rays with debris in the hypothetical Oort cloud could produce a sizable gamma-ray flux, provided that the column density is larger than $10^{-3}\,\mathrm{g\,cm^{-2}}$ [269]. Since all these contributions to the total flux are perfectly isotropic, they cancel out when calculating the difference of the fluxes between the Galactic center and the Galactic anticenter hemispheres.

To analyze the prospects of detecting a gamma-ray anisotropy from dark matter decay at the Fermi LAT it is convenient to define the anisotropy parameter

$$A_{b_0:b_1} = \frac{\bar{J}_{\mathrm{GC}} - \bar{J}_{\mathrm{GAC}}}{\bar{J}_{\mathrm{GC}} + \bar{J}_{\mathrm{GAC}}}\,, \tag{4.35}$$

where $\bar{J}_{\mathrm{GC}}$ and $\bar{J}_{\mathrm{GAC}}$ denote in general the *total* diffuse gamma-ray flux (from dark matter and from astrophysical sources) integrated over E_γ in some energy range, and averaged over the hemisphere in direction of the Galactic center (GC) and anticenter (GAC), respectively. Furthermore, in the adopted definition, sky regions with small, $|b| < b_0$, or large, $|b| > b_1$, Galactic latitudes are excluded from the average.

We have summarized the values of the anisotropy parameter A as predicted for the pure dark matter gamma-ray signal in Tab. 4.7, neglecting ICS

Sky patch	Anisotropy $A_{b_0:b_1}$	
$b_0 : b_1$	Einasto	Isothermal
$10^\circ : 90^\circ$	0.21–0.36	0.20–0.33
$10^\circ : 20^\circ$	0.32–0.50	0.29–0.45
$20^\circ : 60^\circ$	0.21–0.35	0.20–0.33
$60^\circ : 90^\circ$	0.07–0.13	0.07–0.13

Table 4.7: Anisotropy of the gamma-ray signal from dark matter decay in different regions of the sky, see Eq. (4.35). The lower and upper values correspond to dark matter decay producing a monoenergetic line with energy 10 GeV and 1000 GeV, respectively. We show results for the Einasto and the isothermal profile. ICS radiation is neglected and fluxes are integrated over all energies.

radiation. We assume that dark matter decay produces a monoenergetic line with energies between $E'_\gamma = 10\,\text{GeV}$ and 1 TeV (coming for instance from the decay $\psi_{\text{DM}} \to \nu\gamma$), and we show results for different patches of the sky and different halo profiles. As apparent from this table, for large energies and relatively low latitudes the anisotropy A can be as large as 0.50. Including ICS radiation generally increases the overall anisotropy of the dark matter signal. In the region defined by $b_0 = 10^\circ$ and $b_1 = 90^\circ$ (on which we will concentrate below), the anisotropy of the pure dark matter signal ranges between 0.20 and 0.36, with only little dependence on the profile of the dark matter halo. These values have to be compared with the anisotropies of the Galactic foreground. We will discuss this in more details below. However, first we will discuss the detectability of the dipole-like anisotropy in the idealized case of perfect removal of the Galactic foreground.

Without Galactic foreground. To start, we will neglect inverse Compton radiation from electrons and positrons produced in the decay of dark matter particles, and we will assume perfect subtraction of the Galactic foreground. The remaining flux is then expected to be constituted by the isotropic EGBG, which is possibly contaminated by anisotropic prompt radiation from dark matter decay inside and outside the Galactic halo. For definiteness, we will assume that the remaining flux follows the a simple power law, which we take to agree with preliminary results from Fermi LAT

for the EGBG [219]

$$\frac{dJ_{\rm EGBG}}{dE_\gamma} = 5.6 \times 10^{-7} (\mathrm{GeV\,cm^2\,s\,sr})^{-1} \left(\frac{E_\gamma}{1\,\mathrm{GeV}}\right)^{-2.41} . \tag{4.36}$$

Provided that a fraction $f_{\rm s}$ of the considered gamma-ray photons in a given energy range is due to decaying dark matter, the measured anisotropy A is given by

$$A = f_{\rm s} A_{\rm s} + (1 - f_{\rm s}) A_{\rm bg} . \tag{4.37}$$

Here, $A_{\rm s}$ and $A_{\rm bg}$ denote the anisotropy of the dark matter signal, which can be read off from Tab. 4.7, and the anisotropy of the astrophysical background, which is $A_{\rm bg} = 0$ in our case, respectively. A possible evidence at the 2σ-level requires that

$$f_{\rm s} > \frac{2\sigma_A}{A_{\rm s} - A_{\rm bg}} , \tag{4.38}$$

where σ_A denotes the standard deviation of the anisotropy A. It depends on the total number of measured photons, N_γ and can be approximated by $\sigma_A \simeq N_\gamma^{-1/2}$.[17] The photon number is given by

$$N_\gamma = \varepsilon \cdot \Omega_{\rm sky} \int_{E_0}^{E_1} dE_\gamma \frac{dJ}{dE_\gamma} , \tag{4.39}$$

where ε denotes the experimentally given exposure and $\Omega_{\rm sky}$ is the solid angle of the observed sky, which is given by $\Omega_{\rm sky} = 0.83 \cdot 4\pi$ if the Galactic disk with $|b| < 10^\circ$ is excluded. Throughout this section we will assume exposures of $\varepsilon = 3 \times 10^{10}\,\mathrm{cm^2\,s}$ [218] and $\varepsilon = 2 \times 10^{11}\,\mathrm{cm^2\,s}$ [71] for one and five years of Fermi LAT data taking, respectively. Following Eq. (4.36) the Fermi LAT will then detect $N_\gamma \simeq 3.0 \times 10^4$ ($N_\gamma \simeq 1.1 \times 10^3$) photons with energies $E_\gamma \geq 10\,\mathrm{GeV}$ ($E_\gamma \geq 100\,\mathrm{GeV}$) after five years. Taking for definiteness $A_{\rm s} = 0.3$, this allows in principle a 2σ-signal of a dark matter contamination down to $f_s \simeq 4\%$ ($f_s \simeq 20\%$). Note, however, that additional statistical noise and systematic uncertainties from point source subtraction and the determination of the Galactic foreground are neglected and will most probably reduce the sensitivity to f_s by factors of order one.

Uncertainties in the determination of the large-scale anisotropy come from different sources. When neglecting ICS radiation, the prediction of an

[17] The adopted approximation for σ_A is better than 10% as long as $|A| \lesssim 0.3$ and $\sigma_A \lesssim 0.2$. See appx. B.1 for a short discussion.

anisotropy between 0.2 and 0.3 in the dark matter signal at latitudes $|b| > 10^\circ$ is relatively robust. The main sources of uncertainty are the profile of the Milky Way dark matter halo and its normalization. As discussed above, the dependence on the profile is rather weak (*cf.* Tab. 4.7). Only in the case of a much lower value for the local dark matter density, say $\rho_\odot = 0.2\,\mathrm{GeV\,cm^{-3}}$, and only for gamma rays with energies $E'_\gamma \lesssim 10\,\mathrm{GeV}$, the anisotropy of the pure prompt dark matter signal can become as small as $A \simeq 0.15$. On the other hand, the anisotropy of the ICS radiation from dark matter electrons and positrons is typically larger than the anisotropy of the prompt signal, but its exact calculation is plagued with many uncertainties like the exact height of the diffusion zone, the distribution of the ISRF and the size of the Galactic magnetic field (see Ref. [70] for a discussion).

With Galactic foreground. The anisotropy predicted for the radiation from dark matter decay has to be compared with the anisotropies of the Galactic foreground as predicted by *e.g.* GalProp. Most interestingly, they are typically somewhat smaller, around $A \lesssim 0.10$ in all the latitude regions in Tab. 4.7, up to energies above 300 GeV. Furthermore, the anisotropies measured by EGRET for energies below 10 GeV are consistent with the predictions for the Galactic foreground [57].

To illustrate the behavior of the anisotropy parameter A as could be in principle caused by dark matter decay, we will show predictions for different dark matter decay channels and masses, including Galactic foreground radiation and the astrophysical extragalactic background. As Galactic foreground we take predictions of the conventional GalProp-model as presented in Ref. [56] (model 44_500180), and as astrophysical EGBG we take the flux shown in Eq. (4.36).

We show in the left panels of Fig. 4.15 the predicted anisotropy of the *total* diffuse gamma-ray flux that would be measurable in different regions of the sky if the dark matter particles decay exclusively into $\tau^+\tau^-$ pairs. The dark matter mass is taken to be $M_{\mathrm{DM}} = 600\,\mathrm{GeV}$, and we set the lifetime to $\tau_{\mathrm{DM}} \simeq 3.5 \times 10^{27}\,\mathrm{s}$. The energy spectra $dN_{\gamma,\mathrm{e}}/dE_{\gamma,\mathrm{e}}$ of the photons, electrons and positrons produced in the decay are calculated with the event generator Pythia 6.4 [247]. The lifetime is chosen such that the gamma-ray fluxes are below and compatible with the EGBG, as demonstrated in the right panels of Fig. 4.15, where we also show preliminary results from the Fermi

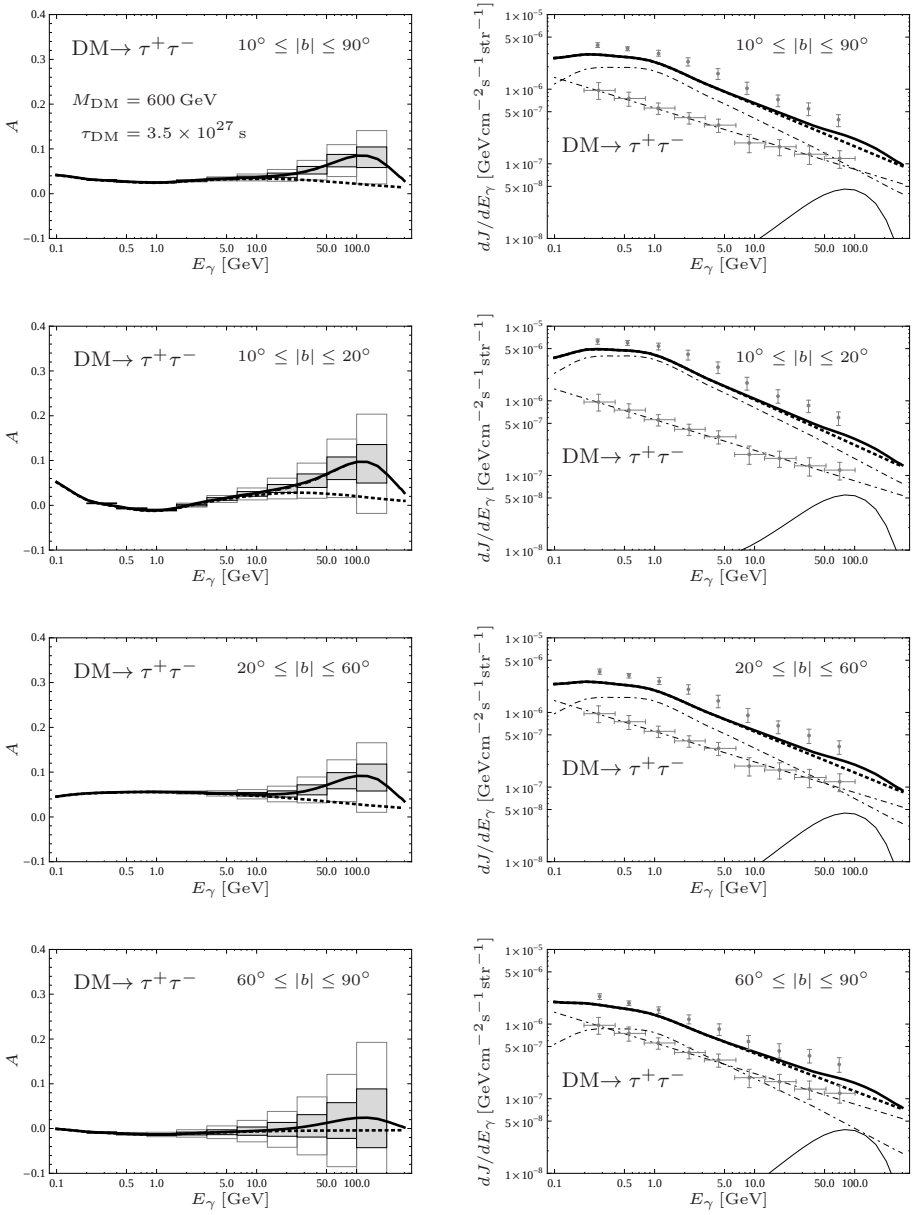

Figure 4.15: Anisotropy (*left*) and total flux (*right*) of gamma-ray flux from dark matter decay into $\tau^+\tau^-$, in different latitude regions of the sky. See caption of Fig. 4.17 for details.

LAT for comparison.[18] Furthermore, we note that the contribution to the local electron and positron fluxes from dark matter decay is negligible in this scenario. Interestingly, for the adopted choice of parameters, an anisotropy is predicted that is significantly different to the one expected from the diffuse Galactic emission in the conventional GalProp model. Such an anisotropy should, moreover, be observable by Fermi LAT, as illustrated by the boxes in the figure, which correspond to our estimates of the one-year and five-year statistical errors of Fermi LAT (for a discussion about our calculation of the statistical errors see above and appx. B.1). As expected, the size of the anisotropy is largest at low latitudes $b \lesssim 20^\circ$ (second row of panels in Fig. 4.15), and decreases slowly when considering higher latitudes (lower panels). On the other hand, the statistical error is smallest in the sky-patch shown in the upper panels of Fig. 4.15, where the whole sky with $|b| \geq 10^\circ$ is included. The effects of ICS radiation are negligible in the present case of decay into $\tau^+\tau^-$ pairs, since the electrons and positrons produced in the subsequent decay of the taus have only relatively small energies.

To illustrate the impact of ICS radiation on the anisotropy parameter A, we show in Fig. 4.16 the anisotropy of the gamma-ray flux assuming that the dark matter particle decays into e^+e^- pairs (with $M_{\rm DM} = 1000\,{\rm GeV}$ and $\tau_{\rm DM} = 2 \times 10^{27}\,{\rm s}$). In this case the dominant source of gamma rays is inverse Compton scattering.[19] For reference, we also show the anisotropy that would be measurable if ICS radiation were absent (dashed lines in left panels of Fig. 4.16). Note that in this scenario electrons and positrons produced in the dark matter decay give a sizeable contribution to the local cosmic-ray fluxes, without being in conflict with the PAMELA and Fermi LAT data. Again, we find that an increased anisotropy is expected in several patches of the sky at high energy. In this case, however, the gamma rays relevant for our predictions are mainly produced by ICS close to the Galactic center, above and below the Galactic disk. Hence, the anisotropies are relatively weak at higher latitudes $|b| \gtrsim 20^\circ$.

[18] Fitting the preliminary Fermi LAT results with a Galactic foreground model is well beyond the scope of this work. Hence, there is a mismatch between the total fluxes and the data.

[19] We assumed that the decaying dark matter particle has spin 1. For scalar dark matter particles, helicity suppression leads to an enhanced production of final-state radiation [270], weakening the relative contribution from ICS.

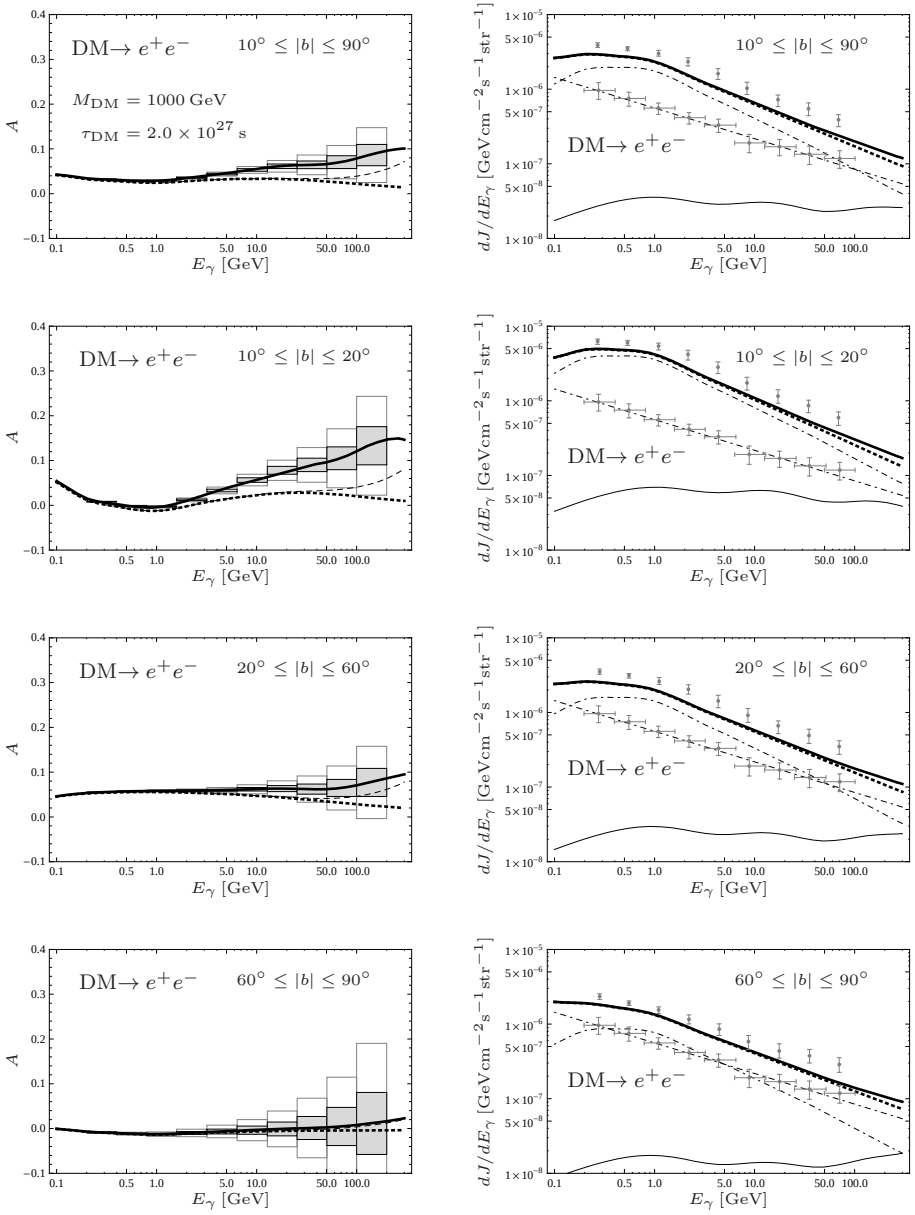

Figure 4.16: Anisotropy (*left*) and total flux (*right*) of gamma-ray flux from dark matter decay into e^+e^-, in different latitude regions of the sky. See caption of Fig. 4.17 for details.

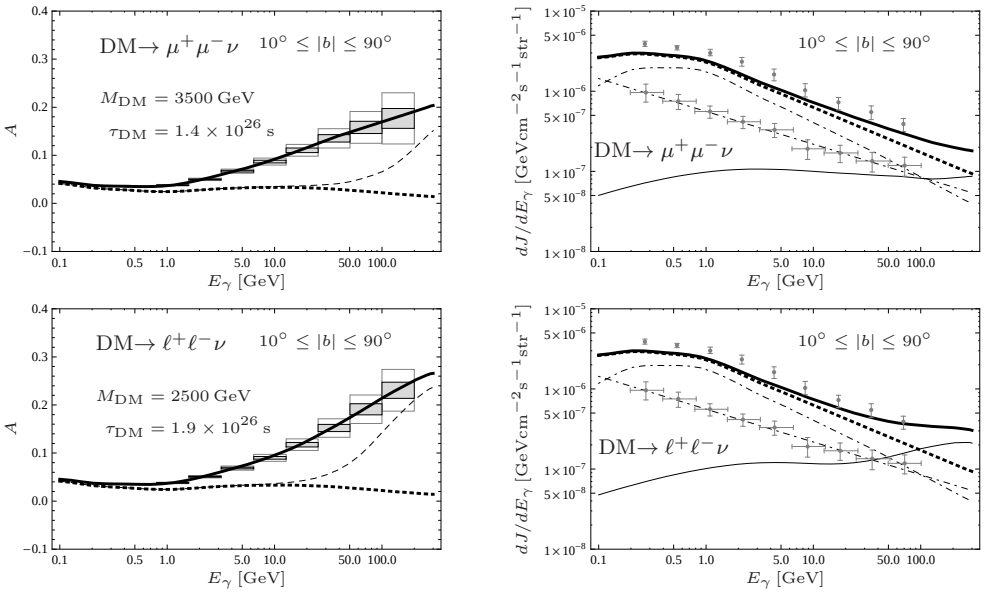

Figure 4.17: Predictions for the first two dark matter decay channels that were found to fit the positron excess as observed by PAMELA/Fermi, see Tab. 4.3. Here, we only consider the sky region defined by $10^\circ \leq |b| \leq 90^\circ$, as indicated in the plots. *Left panels:* Anisotropy of the gamma-ray flux from dark matter decay. The *dotted line* shows the background anisotropy as expected from the Galactic foreground, while the *solid line* shows the anisotropy of signal + background. We also show the signal + background anisotropy neglecting gamma rays from ICS (*dashed line*). The boxes show estimates of the statistical errors for 1-year and 5-year Fermi LAT observations. *Right panels:* Gamma-ray fluxes averaged over all Galactic longitudes as a function of energy. The *thin solid line* shows the gamma rays from dark matter decay. The two *dash-dotted lines* show the astrophysical EGBG and the Galactic foreground separately. The *thick solid line* shows the sum of all contributions, whereas the *dotted line* shows the sum without contributions from dark matter. From *top to bottom* the different panels show predictions for different patches of the sky. The data points show preliminary Fermi LAT data [218] for the total diffuse flux (*upper points*) and the EGBG (*lower points*).

4.3.4 Gamma-ray predictions for the decaying dark matter interpretation of the positron excess

If dark matter decay is the origin of the excess in the positron fraction observed by PAMELA and in the total electron-plus-positron flux observed by

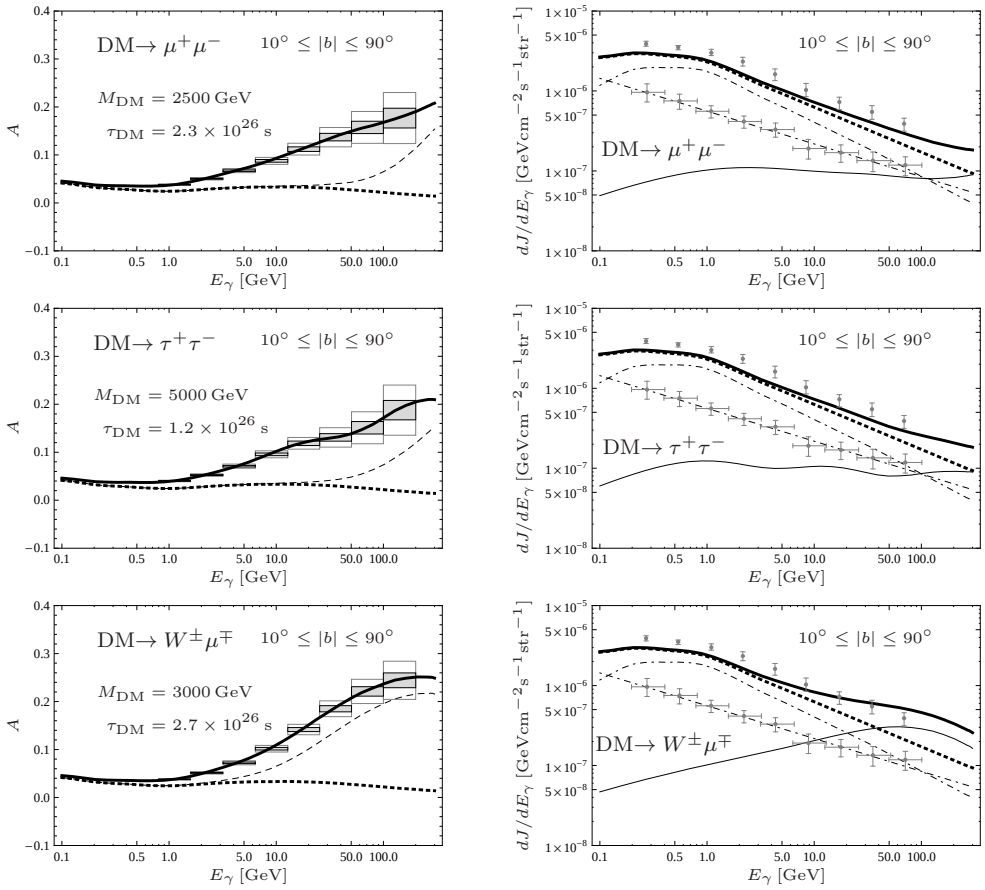

Figure 4.18: Predictions for the last three dark matter decay channels that were found to fit the positron excess as observed by PAMELA/Fermi, see Tab. 4.3. See caption of Fig. 4.17 for details.

the Fermi LAT, the predicted anisotropies in the gamma-ray flux can be quite large. In Figs. 4.17 and 4.18 we show our results for the anisotropy, A, which is expected to be observed by the Fermi LAT if the dark matter particle decays via one of the five different decay channels that were found above in section 4.2.2 to fit well the positron and electron data.[20] We concentrate on the region defined by $b_0 = 10^\circ$ and $b_1 = 90^\circ$. As apparent from

[20] We use slightly larger lifetimes than in the above section, to account for the larger value for the local dark matter density used in this section.

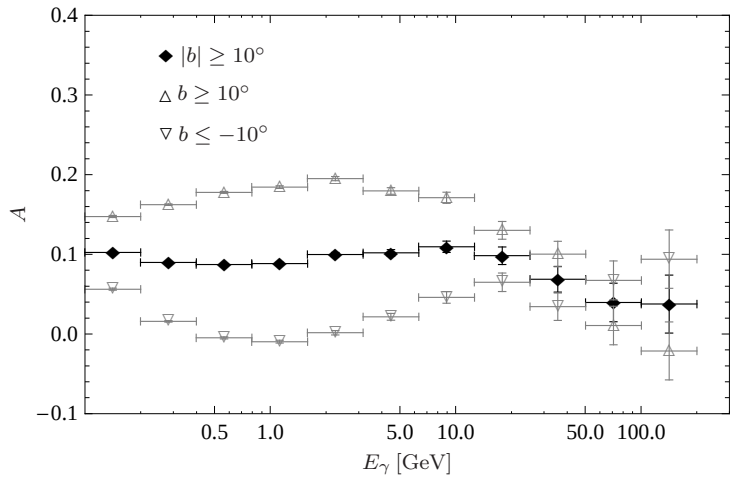

Figure 4.19: Observed anisotropy of the northern, the southern and both hemispheres, excluding the Galactic plane. The points and their statistical error-bars are derived from the unsubtracted one-year Fermi LAT data. No systematic errors are included. Point sources are expected to contribute only subdominantly to the overall flux [219, 220], hence the anisotropy is expected to be mainly due to the diffuse radiation component. At energies around and above 50 GeV isotropic background contamination becomes relevant. The shown data points are derived from publicly available photon event data, as described in the text, and are *no official data release.*

the plots, the predictions for some decay channels (namely the decay into $W^{\pm}\mu^{\mp}$) are already in conflict with the preliminary results of the Fermi LAT collaboration for the EGBG, whereas the other decay channels are marginally consistent. However, even for those channels which are compatible with the data, sizeable anisotropies, around $A \simeq 0.2$–0.3, are predicted at energies around $E_\gamma \approx 100\,\mathrm{GeV}$. This is significantly different from the anisotropy expected for the astrophysical foreground. As indicated by our estimates of the statistical error bars for one-year Fermi LAT data taking, this deviation could be visible in the upcoming results for the diffuse gamma-ray sky. On the other hand, its non-observation could potentially set very strong constraints on the decaying dark matter interpretation of the positron excess observed by PAMELA/Fermi LAT.

Discussion. Fermi LAT takes data for already more than one year. No official release of the point source subtracted diffuse flux exists at the moment, but the lists with detected photon events,[21] as well as the required analysis tools,[22] are publicly available. In Fig. 4.19 we show our results for the observed anisotropy in the energy range 0.1–200 GeV, as we derived from these public photon event data, using the "diffuse" event class, including data from 4 Aug 2008 to 25 Aug 2009. Our data analysis followed the description given on the Fermi LAT website,[23] and is also outlined in Ref. [271], whose results we confirm.

As apparent from Fig. 4.19, the anisotropy below 10 GeV is around 10% if north and south hemisphere are considered together, which is somewhat larger than predicted by the GalProp model that we used above, at energies above 10 GeV the anisotropy decrease and approaches almost zero. This latter effect is due to the fact that the data used is contaminated with isotropic background, which becomes severe at higher energies. Hence conclusions drawn from gamma rays with higher energies have to wait until data with better background rejection becomes public. However, the fact that already at lower energies the observed anisotropy is above the a-priori expectations is interesting, and in qualitative agreement with the claimed existence of the "Fermi Haze" [271]. It is also consistent with the fact that foreground models currently discussed in light of the Fermi LAT data typically require somewhat increased electron and positron fluxes (which produce anisotropic ICS radiation) with respect to previous models, to accommodate the observations [220].

In how far these increased fluxes can be due to decaying dark matter models which fit the PAMELA excess is a question left for future work. Note, however, that an increased Galactic foreground could also reduce the anisotropy of the overall signal with respect to our predictions when the dark matter contribution remains fixed. In any case, as shown in Fig. 4.17 and 4.18, dark matter would mainly affect the anisotropy at very high energies, a quantity which is not yet accessible with currently available data.

[21] See `http://fermi.gsfc.nasa.gov/ssc/data/access/`.
[22] See `http://fermi.gsfc.nasa.gov/ssc/data/analysis/`.
[23] See `http://fermi.gsfc.nasa.gov/ssc/data/analysis/documentation`.

4.4 Prospects

The *Fermi Gamma-ray Space Telescope* with the LAT (*Large Area Telescope*) as main detector was launched in June 2008 and is expected to take data 5 to 10 years in total. The Fermi LAT collaboration is expected to release the analysis of the diffuse gamma-ray sky soon, together with an interpretation in terms of astrophysical processes. Simultaneously, photon event data with better background rejection should become available. This data will be invaluable for putting more stringent bounds on—or finding more hints for—the dark matter interpretation of the PAMELA positron excess. However, publicly available data, which still has a sizeable background contamination at higher gamma-ray energies above around 50 GeV, is available online. This data, together with preliminary results shown in different public talks, was already used to derive first constraints on dark matter models [70, 72–74], which will be considerably improved once data with better background rejection becomes available. Apart from that, the Fermi LAT collaboration will also extend their results for the total electron plus positron flux down to energies of 5 GeV.

PAMELA (*Payload for Antimatter Matter Exploration and Light-nuclei Astrophysics*) was launched already in June 2006 and is still taking data. Up to now the positron fraction, as well as the $\bar{p}/p$-ratio are published up to energies of 100 GeV. However, also the publication of total positron and antiproton fluxes is announced, and the measurement of the positron fraction may increase up to energies of 2 TeV.[24] This, together with the total flux from Fermi LAT, would be of great importance to determine the exact energy spectrum of the electron and positron fluxes, giving much more stringent constraints on any particle-physics interpretation of the positron excess. Furthermore, PAMELA is measuring light nuclei up to $Z = 6$, up to energies around 200 GeV.

Finally, the launch of the AMS-02 (*Alpha Magnetic Spectrometer*), which will be mounted and operate on the International Space Station, is announced for July 2010. AMS-02 has similar physics goals than PAMELA and will measure cosmic-ray nuclei up to iron, as well as positrons and electrons, with great precision, and up to energies of 1 TeV depending on the particle species. It will, together with the above experiments, help to further understand the generation and propagation of cosmic rays in the Galaxy, and it will increase

[24] See `http://pamela.roma2.infn.it/`.

our knowledge about astrophysical foregrounds as well as the sensitivity of indirect dark matter searches in the upcoming years.

Chapter 5

Conclusions

One of the greatest mysteries of today's fundamental physics is the nature of dark matter. Beside the paradigmatic WIMP scenarios, many other models for dark matter exist, with dark matter particles that couple much more weakly than electroweak to the Standard Model sector. These superweakly coupled dark matter candidates give rise to a broad spectrum of phenomenology, with the details depending on the actual size of the coupling to Standard Model particles. For couplings that are associated with particle lifetimes of the order of seconds to hours, these dark matter particles can constitute typical superWIMP scenarios, where the dark matter particle is produced in the late decay of other particles, potentially interfering with BBN or the formation of LSS. For couplings that are associated with lifetimes much longer than the age of the Universe, the superweakly coupled dark matter particles can constitute decaying dark matter, potentially leaving their imprint in the observed cosmic-ray fluxes.

In this thesis we have studied scenarios with superweakly coupled dark matter in both the superWIMP and the decaying dark matter regime. As a concrete and important example, we discussed the gaugino of a hidden $U(1)_X$ gauge group, which remains unbroken and which kinetically mixes with the hypercharge $U(1)_Y$. We worked out the relevant cosmological bounds as well as discussed different phenomenological prospects like possible cosmic-ray signals. Furthermore, and beyond this particular scenario, we studied the cosmic-ray predictions of decaying dark matter in general, with emphasis on the positron excess as observed by PAMELA and corresponding prospects for gamma-ray observations with the Fermi LAT.

We have worked out different kinds of cosmological bounds on the hidden $U(1)_X$ gaugino superWIMP scenarios, with kinetic mixing parameters in the range $\chi \sim 10^{-16}$–10^{-2}, see section 3.3. To this end we mainly concentrated on cases where the hidden $U(1)_X$ gaugino is the LSP, and the NLSP is either a bino or a stau. The most model-independent constraint on the mixing parameter comes from the potential thermal overproduction of the hidden gaugino, yielding an upper bound of the order of $\chi \lesssim \mathcal{O}(10^{-11})$. Lower bounds on the mixing parameter can be derived by requiring that the NLSP decay, which produces the LSP, does not destroy the predictions of the standard BBN scenario. These bounds depend on the actual nature of the NLSP, and we showed that in typical scenarios with a bino NLSP the whole range of mixing parameters above can be excluded, whereas in scenarios with stau NLSPs an allowed band remains with mixings around $\chi \sim 10^{-13}$–10^{-10}. Bounds from the possible interference with structure formation turned out to be subdominant. Typical collider signatures of the stau NLSP would be displaced vertices and heavily ionizing charged tracks.

We also studied an intriguing case with two superWIMPs, where the gravitino is the LSP, the hidden gaugino the NLSP, and the stau the NNLSP. It turned out that the bare existence of the hidden gaugino can considerably weaken upper bounds that hold on the reheating temperature in gravitino dark matter scenarios with stau NLSPs. This in turn in principle allows us to reconcile gravitino dark matter with leptogenesis, which is a promising mechanism for generating the baryon asymmetry of the Universe. Possible collider predictions are again the observation of long-lived charged particles.

Recently, kinetically mixed gauginos of additional unbroken $U(1)$ gauge groups were emphasized in the literature to be generic structures that appear in type IIa and IIb string theories in form of RR $U(1)$s. In this context it was also pointed out that they are prototypic examples for models in which the dark matter particle is produced at low temperatures by "freeze-in", a mechanism which requires that the coupling to Standard Model particles is renormalizable, with a dimensionless coupling constant of the order of 10^{-12}. This is exactly what we had found in the special case of hidden $U(1)_X$ gauginos. Models of this kind, which in some sense generalize the phenomenology of hidden $U(1)_X$ gaugino superWIMPs, were called FIMP (*Feebly Interacting Massive Particle*) dark matter.

However, the maybe most intriguing aspect of the hidden $U(1)_X$ gaugino scenario is that it is an example of a supersymmetric model which is strongly constrained by current observations, whereas its pure non-supersymmetric

counterpart (with just a kinetically mixed massless Abelian gauge boson) remains practically unconstrained. Future questions, which lie beyond the scope of this work, include a more detailed study of the thermal production and the overproduction constraints, as well as a more thorough study of the outlined mechanism that allows us to weaken constraints on the reheating temperature. Actually, this mechanism is expected to be quite generic in scenarios with superweakly interacting hidden sectors and not limited to the case of hidden $U(1)_X$ gauginos.

For mixing parameters around $\chi \sim \mathcal{O}(10^{-24})$, well below the above values required for superWIMP behavior, scenarios with hidden $U(1)_X$ gauginos can constitute decaying dark matter, see section 4.2.3. We concentrated on the case that either the hidden $U(1)_X$ gaugino or a neutralino is the NLSP and decays with lifetimes $\mathcal{O}(10^{26}\,\mathrm{s})$ into the LSP, which is then assumed to be the neutralino or the hidden gaugino, respectively. For a reference mSUGRA model that completely defines the spectrum and mixing parameters in the MSSM sector, and that lies in the coannihilation region of the parameter space, we calculated explicitly all relevant tree-level branching ratios and decay modes as function of the mass of the hidden $U(1)_X$ gaugino. The mass of the lightest neutralino in this reference model is 301 GeV, whereas we considered smaller and larger hidden $U(1)_X$ gaugino masses ranging from 1 GeV up to 1600 GeV. It turned out that, although the kinetic mixing in principle allows decay into a multitude of different final states, in particular leptonic channels are favored for most hidden gaugino masses, making is an example for leptophilic dark matter. This is mainly due to the small slepton and large squark masses in our reference scenario. Furthermore, we calculated the energy spectra of the decay products as well as their spectra after propagation through the Galaxy with Monte Carlo and semi-analytical methods. Comparison of our results with the recent observations of PAMELA and Fermi LAT showed that it is difficult to account for the observations within the framework of our reference model. However, it is possible to find idealized, though cosmologically problematic, examples with *e.g.* purely three-body decaying very heavy binos that can fit the data well. Corresponding predictions are a sizeable gamma-ray flux that could be observable with the Fermi LAT in the near future.

Furthermore, and independently of concrete particle-physics models, we studied the cosmic-ray predictions of generic decaying dark matter scenarios. In particular we concentrated on the interpretation of the recently observed

positron excess in terms of decaying dark matter, see section 4.2.2. For standard background fluxes, and standard propagation models, we singled out some decay channels that can qualitatively well fit the $e^{\pm}$-observations of PAMELA, Fermi LAT and HESS. To this end we assumed that dark matter decays with 100% branching ratio into different final states, concentrating on two-body and three-body decay channels. We found that in particular muonic decays are favored, whereas the decay into electrons in general generates a too hard, and the decay into taus a too soft cosmic-ray $e^{\pm}$-spectrum with respect to the observations. Furthermore, we calculated the propagated antiproton spectra and the $\bar{p}/p$-ratio and compared it with recent results from PAMELA. It turned out that the decay into $W^{\pm}\mu^{\mp}$, which otherwise fits the $e^{\pm}$-data well, is disfavored by the observations of $\bar{p}/p$. In the, by now vast, literature about the dark matter interpretation of the PAMELA positron excess related works exist, where often χ^2-fits to the data were performed, coming to similar conclusions.

It is by now well established that the observed positron excess can be explained by different decaying dark matter models, and confirmation or rejection of this interpretation could come from observations in the gamma-ray channel, which is in principle sensitive to source distributions and currently measured by Fermi LAT. In the last part of this thesis we studied the gamma-ray predictions from decaying dark matter, see section 4.3. We reviewed the different sources of gamma rays that are generically produced in the decay of dark matter, as well as the fact that the prompt component of the gamma-ray signal is expected to show up at high Galactic latitudes, similar to the EGBG. We then discussed the peculiar dipole-like anisotropy of the dark matter signal, coming from the offset between Sun and Galactic center. We quantified this anisotropy, as defined in Eq. (4.35), by calculating differences between fluxes in the hemisphere pointing to the Galactic center and fluxes in the hemisphere pointing to the anti-center. For the EGBG this anisotropy is expected to be zero, whereas it is around 0.2–0.3 for decaying dark matter signals. After subtraction of the Galactic foreground one could hence use the anisotropy of the remaining signal to constrain the signal fraction that could come from decaying dark matter, and we discussed corresponding prospects for Fermi LAT.

Taking as Galactic foreground the predictions from a conventional GalProp model, we demonstrated that dark matter signals could even show up as a spectral feature in the anisotropy of the *total* diffuse flux, since the anisotropy of the adopted Galactic foreground was smaller than the

anisotropy of the pure dark matter signal. Furthermore, we showed predictions for the anisotropy of the total flux that should be observable with Fermi LAT if the PAMELA excess is due to decaying dark matter. We demonstrated that, relying on the above predictions for the Galactic foreground, significant anisotropies should be visible in the data at high energies. Finally, we presented results for the anisotropy of the *observed* overall flux, based on publicly available one-year Fermi LAT data, which at high energies however still is strongly contaminated with isotropic background and does not allow definite conclusions about the decaying dark matter scenario. An official data release with better background rejection and point source subtraction will improve this situation considerably in the next future.

Future work in connection with gamma-ray observations include for instance a more thorough study of inverse Compton radiation caused by dark matter decay inside the Galactic halo but outside the diffusion zone, a careful analysis of the upcoming Fermi LAT diffuse gamma-ray skymaps, and in particular a search for potential dipole-like anisotropies in the data.

Appendix A

Hidden $U(1)_X$ Gauginos

In this appendix we will give details about different calculations related to the hidden $U(1)_X$ gaugino dark matter. We will start with a discussion about the renormalization group for the kinetic and mass mixing parameters, than explain quickly the thermal production calculation, and we end with an table of decay widths relevant for this work.

A.1 Renormalization Group Equations

The RGEs for multiple $U(1)$ models with kinetic mixing were first presented in Ref. [197]. One-loop RGEs for gaugino masses and their mixings can be found in Ref. [272]. We confirmed their calculations, and will only present the results in a convenient form.

The RGEs acquire their simplest form in the basis where gauge bosons and gauginos have a canonical kinetic term. The matrix of the gauge couplings $\bar{g}_{ij}$ is defined according to the term $\mathcal{L} \supset \bar{g}_{ij} j_i^\mu A_\mu^j$ in the Lagrangian, where the indices $i = 1, 2$ and $j = 1, 2$ run over the charged currents of the two sectors and over the gauge boson states, respectively. The renormalization group equations for the couplings $\bar{g}$ are given by

$$\frac{d}{dt}\bar{g} = \frac{1}{16\pi^2}\bar{g}\bar{g}^T B \bar{g} \,, \tag{A.1}$$

where we have used the charge matrix $B_{ij} = \mathrm{tr}(Q_i Q_j)$, and $t = \ln(Q/Q_0)$ with Q as RG scale. The trace in B_{ij} runs over all chiral supermultiplets with mass $m < Q$. On the other hand, the RGEs for the gaugino mass matrix $\bar{\mathcal{M}}$

take a similar form

$$\frac{d}{dt}\bar{\mathcal{M}} = \frac{1}{16\pi^2}\left(\bar{\mathcal{M}}\bar{g}^T B\bar{g} + \bar{g}^T B\bar{g}\bar{\mathcal{M}}\right) . \tag{A.2}$$

Note that only three of the four entries of $\bar{g}$ are physical because the basis of the gauge bosons is only fixed up to a rotation. It is convenient to state the RGEs for the case where the non-diagonal elements in the couplings g_{ij} are chosen to vanish, and where the third free component of g_{ij} is absorbed into the kinetic mixing term like in Eq. (3.8). We obtain

$$\frac{d}{dt}g_{X,B} = \frac{1}{16\pi^2} g_{X,B}^3 B_{XX,BB} , \tag{A.3}$$

$$\frac{d}{dt}\chi = -\frac{1}{8\pi^2} g_X g_B B_{XB} + \frac{1}{16\pi^2}\chi\left(g_X^2 B_{XX} + g_B^2 B_{BB}\right) + \mathcal{O}(\chi^2) , \tag{A.4}$$

$$\frac{d}{dt}\hat{M}_{X,B} = \frac{1}{8\pi^2} g_{X,B}^2 B_{XX,BB}\hat{M}_{X,B} , \tag{A.5}$$

$$\frac{d}{dt}\delta\hat{M} = \frac{1}{16\pi^2}\left(g_X^2 B_{XX} + g_B^2 B_{BB}\right)\delta\hat{M} + \mathcal{O}(\chi^2) . \tag{A.6}$$

The first and the third equation are the standard RGEs for the coupling constants and gaugino masses of $U(1)$ gauge groups, the second and the fourth equation give the renormalization of the mixing parameters. Note that, as long as $B_{XB} = 0$, the renormalization of the mass and mixing parameter are related via $\delta\hat{M}d\chi/dt = d\delta\hat{M}/dt$.

A.2 Thermal Production

The thermal production of particles during the early Universe is described by a simple Boltzmann equation, which in our case reads

$$\frac{dn}{dt} + 3H(T)\, n = \gamma_{\text{int}}(T) . \tag{A.7}$$

Here, n denotes the number density of hidden gauginos and $\gamma_{\text{int}}(T)$ denotes their production rate per volume as function of of the actual plasma temperature T. Furthermore, the Hubble expansion rate H is simply given by the expression

$$H = \sqrt{\frac{g_*\pi^2}{90}}\frac{T^2}{M_P} , \tag{A.8}$$

and depends only on T and the number of relativistic degrees of freedom g_* [30]. In the MSSM the latter is given by $g_* = 915/4$ when all particles are included.

The production rate $\gamma_{\rm int}$ for two-particle scattering processes $p_1\, p_2 \to\ p_3\, p_4$, where the p_i denote the four-momenta of the participating particles, reads in general [164]

$$\gamma_{\rm int} = \int \prod_{i=1}^{4} \left(\frac{dp_i^3}{(2\pi)^3} \frac{1}{2E_i} \right) (2\pi)^4 \delta^{(4)}(p_1 + p_2 - p_3 - p_4) |\bar{\mathcal{M}}|^2 f(E_1) f(E_2) \ . \quad \text{(A.9)}$$

Here, $|\bar{\mathcal{M}}|^2$ denotes the squared matrix element of the a given production channel, summed over incoming and outgoing spins, and $f(E_i)$ denote the energy distribution function of the particles in the plasma.

For an arbitrary function of the four-momenta, $g(p_i)$, the above phase-space integral can be evaluated according to

$$\begin{aligned} &\int \prod_{i=1}^{4} \left(\frac{dp_i^3}{(2\pi)^3} \frac{1}{2E_i} \right) (2\pi)^4 \delta^{(4)}(p_1 + p_2 - p_3 - p_4) g(p_i) = \quad \text{(A.10)} \\ &\qquad \frac{1}{16\pi} \frac{1}{(2\pi)^5} \int_0^\infty dE_3 dE_4 \int_{-E_3}^{E_4} dE \int_{|E|}^\infty dk \int_0^{2\pi} d\phi_3 \times \\ &\qquad \times \theta(2E_3 + E - k)\, \theta(2E_4 - E - k)\ g(p_i) \ , \end{aligned}$$

where in general $E_{1,2} = E_{3,4} \pm E$, $\theta(x)$ denotes the Heaviside step functions with $\theta(x) = 1$ for $x > 0$ and $\theta(x) = 0$ for $x < 0$, and the Mandelstam variables obey the equations

$$\begin{aligned} s &= (p_1 + p_2)^2 = 2E_3 E_4 - 2\vec{p_3} \cdot \vec{p_4} \ , \\ t &= (p_1 - p_3)^2 = E^2 - k^2 \ , \\ u &= (p_1 - p_4)^2 = k^2 - E^2 - 2E_3 E_4 + 2\vec{p_3} \cdot \vec{p_4} \ , \end{aligned} \quad \text{(A.11)}$$

where

$$\begin{aligned} \vec{p_3} \cdot \vec{p_4} = &\cos\phi_3 \cdot \frac{k^2 - E^2}{4k^2} \sqrt{(E + 2E_3)^2 - k^2} \sqrt{(E - 2E_4)^2 - k^2} + \\ &+ \frac{1}{4k^2} (2EE_3 - k^2 + E^2)(2EE_4 + k^2 - E^2) \ . \end{aligned} \quad \text{(A.12)}$$

The dominant part of the hidden gaugino production is expected to come from superQCD sector, due to the large QCD couplings and the large multiplicity of particle states. The processes that we take into account in our calculation are summarized in Tab. 3.1. Participating particles in these processes are the quarks q, squarks $\tilde{q}$, gluons g, gluinos $\tilde{g}$ and hidden gauginos B. The corresponding 14 Feynman graphs and 7 matrix elements can be calculated with standard MSSM Feynman rules (see *e.g.* Refs. [9, 273]). Our results in terms of Mandelstam variables [164] are shown in Tab. 3.1.

It is now straightforward to apply Eq. (A.10) to the results shown in Tab. 3.1. For the phase space distributions $f(E_i)$ we simply adopt Boltzmann distributions for fermions as well as scalars. As result we obtain

$$\begin{aligned} \gamma_{\rm QCD} \equiv \frac{d^4 n_X}{dV dt} &= \frac{308}{3\pi^3}\alpha'\alpha_s\Theta(T)^2\left(1-\frac{4}{7}\gamma_E-\frac{4}{7}\ln\frac{k^*}{T}\right)T^4 \\ &\simeq 3\times 10^{-3}\Theta(T)^2 T^4 \,. \end{aligned} \tag{A.13}$$

In general one has to take into account the temperature dependence of the mixing angle Θ, which stems from the thermal mass of the bino, see Eq. (3.15). Here, we simply take $M_B(T) \simeq M_B$, since most of the production happens when the particles become non-relativistic, as discussed below. In this equation, α' and α_s denote the hypercharge and QCD couplings, respectively, and $\gamma_E \simeq 0.577$. Furthermore, k^* denotes the lower cut-off of intermediate three-momenta in t-channel processes, which diverge in the limit $k^* \to 0$. Only processes with quarks in the intermediate state contribute to these divergences, and we identify k^* with their thermal mass (at temperatures around $T \sim \mathcal{O}(100\,\mathrm{GeV})$ the thermal quark masses lie between $0.63T$ and $0.84T$, depending on the quantum numbers [184]). Finally, solving the Boltzmann equation yields the thermal abundance of hidden $U(1)_X$ gauginos,

$$\Omega_X h^2 \approx 5.5\times 10^7 \left(\frac{M_X}{100\,\mathrm{GeV}}\right)\int_{T_0}^{T_R} dT \frac{M_P}{T^2}\frac{\gamma_{\rm QCD}(T)\Theta^2(T)}{T^4} \,. \tag{A.14}$$

Taking into account thermal masses could actually lead to a further order-one enhancement due to particle decay in the QCD plasma [184]. Contributions from electroweak interactions and Yukawa couplings are also expected to give sizable corrections, again of order one. Bearing this limitations in mind, and requiring that $\Omega_X h^2 \lesssim 0.1$, we obtain the overproduction bound

$$\Theta \lesssim 5\times 10^{-12}\left(\frac{M_X}{M_B}\right)^{-1/2} \,. \tag{A.15}$$

Here, we have used $T_0 \simeq M_B$ as a cutoff in Eq. (A.14), which corresponds to squark- and gluino masses around $3M_B$. For other values the bound scales roughly like $\sqrt{T_0}$.

A.3 Decay Widths

We shortly summarize the decay widths of neutralinos, hidden gauginos, sleptons and gravitinos as used in section 3.3.

The required decay widths of a bino-like neutralino that decays via different decay channels into a hidden $U(1)_X$ gaugino can be derived from the results in Ref. [274, 275]. We obtain

$$\Gamma(\lambda_B \to Z\lambda_X) \simeq \frac{1}{128\pi} g'^2 s_W^2 \Theta^2 M_B \frac{M_Z^6}{\mu^4 M_B^2} \sqrt{\lambda\left(1, \frac{M_X^2}{M_B^2}, \frac{M_Z^2}{M_B^2}\right)} \times \\ \times \left(\frac{M_B^2}{M_Z^2} + \frac{M_X^2}{M_Z^2} - 2 + \left(\frac{M_B^2}{M_Z^2} - \frac{M_X^2}{M_Z^2}\right)^2 + 6\frac{M_X}{M_Z}\frac{M_B}{M_Z}\right) , \tag{A.16}$$

$$\Gamma(\lambda_B \to \gamma\lambda_X) \simeq \frac{e^2 g'^4 \Theta^2}{128\pi} \left(\frac{15}{32\pi^2}\right)^2 \frac{M_B^5}{M_{\text{sf}}^4} \left(1 - \frac{M_X^2}{M_B^2}\right)^3 \left(1 - \frac{M_X}{M_B}\right)^2 , \tag{A.17}$$

$$\Gamma(\lambda_B \to h\lambda_X) \simeq \frac{g'^2 \Theta^2}{32\pi} M_B \frac{M_Z^2 s_W^2}{\mu^2} \sqrt{\lambda\left(1, \frac{M_X^2}{M_B^2}, \frac{M_h^2}{M_B^2}\right)} \times \\ \times \left(1 + \frac{M_X^2}{M_B^2} - \frac{M_h^2}{M_B^2} + 2\frac{M_X}{M_B}\right) , \tag{A.18}$$

$$\Gamma(\lambda_B \to f\bar{f}\lambda_X) \simeq 1.4 \times 10^{-4} g'^4 \Theta^2 M_B \frac{M_B^4}{M_{\text{sf}}^4} \left(1 - \frac{M_X^2}{M_B^2}\right)^5 , \tag{A.19}$$

where we made use of the function $\lambda(a^2, b^2, c^2) = (a^2 - (b+c)^2)(a^2 - (b-c)^2)$. The assumed mass spectrum is $M_X < M_B < M_W \ll \mu$, where the approximations used for the neutralino mixing angles become exact in the limit $M_X \ll M_B < M_W \ll \mu$. Note that the two-body decay into a hidden $U(1)_X$

gaugino and a photon, Eq. (A.17), is one-loop suppressed. We sum over all (s)leptons that can run in the loop, assuming that they have a common mass around $M_{\rm sf}$. Furthermore, note that the final states in Eq. (A.19) incorporate neutrinos as well as charged leptons. We took into account sfermions with masses around $M_{\rm sf}$ in the intermediate state. Intermediate Z bosons contribute only subdominantly in our case (for parameters see caption of Fig. 3.2).

The relevant decay widths with gravitinos in the initial or final state can be found in Ref. [183, 276], and we reproduce them here for convenience

$$\Gamma(\lambda_X \to \tilde{G} X) = \frac{1}{48\pi M_{\rm pl}^2} \frac{M_X^5}{M_{\tilde{G}}^2} \left(1 - \frac{M_{\tilde{G}}^2}{M_X^2}\right)^3 \left(1 + 3\frac{M_{\tilde{G}}^2}{M_X^2}\right) , \quad \text{(A.20)}$$

$$\Gamma(\tilde{G} \to \lambda_X X) = \frac{1}{32\pi M_{\rm pl}^2} M_{\tilde{G}}^3 \left(1 - \frac{M_X^2}{M_{\tilde{G}}^2}\right)^3 \left(1 + \frac{1}{3}\frac{M_X^2}{M_{\tilde{G}}^2}\right) , \quad \text{(A.21)}$$

$$\Gamma(\tilde{l} \to \tilde{G} l) = \frac{1}{48\pi M_{\rm pl}^2} \frac{M_{\tilde{l}}^5}{M_{\tilde{G}}^2} \left(1 - \frac{M_{\tilde{G}}^2}{M_{\tilde{l}}^2}\right)^4 . \quad \text{(A.22)}$$

Appendix B

Dark Matter Searches

B.1 Statistical Error of the Anisotropy Parameter

Here, we shortly discuss the statistical errors of the anisotropy parameter as defined in Eq. (4.35), which are due to shot noise.

The measured anisotropy A and the total number of measured photons N are related to the number of photons measured in direction of the Galactic center, N_1, and anticenter, N_2, by $A = (N_1 - N_2)/(N_1 + N_2)$ and $N = N_1 + N_2$. The N_i follow a Poisson distribution with mean $\langle N_i \rangle$ and standard deviation $\sigma_{N_i} = \sqrt{\langle N_i \rangle}$. Considering the propagation of uncertainty, it is straightforward to derive that the statistical error of the anisotropy is given by

$$\sigma_A \simeq \sqrt{\frac{1 - \langle A \rangle^2}{\langle N \rangle}} \,, \tag{B.1}$$

which is expected to hold for small enough $\langle A \rangle \simeq A$ and large enough $\langle N \rangle \simeq N$.

On the other hand, one can derive the exact probability distribution function of the anisotropy A by starting with the above Poisson distributions for the N_i, performing an appropriate redefinition of the parameters and integrating out the total number of measured photons. The result is a function of the mean values $\langle A \rangle$ and $\langle N \rangle$ and can be written in the compact form

$$pdf(A) = \frac{\langle N \rangle}{2\langle N_1 \rangle! \langle N_2 \rangle!} \left(\frac{1 + A}{2} \right)^{\langle N_1 \rangle} \left(\frac{1 - A}{2} \right)^{\langle N_2 \rangle} \,. \tag{B.2}$$

From this equation one can check, for example, that a normal distribution with mean $\langle A \rangle$ and standard deviation as in Eq. (B.1) gives correct error bars at the 5% level as long as $\langle A \rangle < 0.6$ and $\sigma_A < 0.2$. For small enough anisotropies A, however, the standard deviation is just given by $\sigma_A \simeq \sqrt{N^{-1}}$ with good accuracy, and we use this approximation throughout the work.

Bibliography

[1] C. Amsler *et al.* (**Particle Data Group** Collaboration), *Review of particle physics,* Phys. Lett. **B667** (2008) 1.

[2] G. Jungman, M. Kamionkowski, and K. Griest, *Supersymmetric dark matter,* Phys. Rept. **267** (1996) 195, `hep-ph/9506380`.

[3] G. Bertone, D. Hooper, and J. Silk, *Particle dark matter: Evidence, candidates and constraints,* Phys. Rept. **405** (2005) 279, `hep-ph/0404175`.

[4] M. S. Turner, *Cosmological parameters,* (1998), `astro-ph/9904051`.

[5] L. Bergstrom, *Non-baryonic dark matter: Observational evidence and detection methods,* Rept. Prog. Phys. **63** (2000) 793, `hep-ph/0002126`.

[6] L. Bergstrom, *Dark Matter Candidates,* New J. Phys. **11** (2009) 105006, `0903.4849 [hep-ph]`.

[7] F. Zwicky, *Spectral displacement of extra galactic nebulae,* Helv. Phys. Acta **6** (1933) 110.

[8] V. C. Rubin and W. K. Ford, Jr., *Rotation of the Andromeda Nebula from a Spectroscopic Survey of Emission Regions,* Astrophys. J. **159** (1970) 379.

[9] S. P. Martin, *A supersymmetry primer,* (1997), `hep-ph/9709356`.

[10] R. D. Peccei and H. R. Quinn, *CP Conservation in the Presence of Instantons,* Phys. Rev. Lett. **38** (1977) 1440.

[11] S. Weinberg, *A New Light Boson?.* Phys. Rev. Lett. **40** (1978) 223.

[12] F. Wilczek, *Problem of Strong p and t Invariance in the Presence of Instantons,* Phys. Rev. Lett. **40** (1978) 279.

[13] P. Sikivie, *Axion cosmology,* Lect. Notes Phys. **741** (2008) 19, astro-ph/0610440.

[14] P. Van Nieuwenhuizen, *Supergravity,* Phys. Rept. **68** (1981) 189.

[15] J. Wess and J. Bagger, *Supersymmetry and supergravity* (Princeton, USA: Univ. Pr., 1992) p. 256.

[16] M. B. Green, J. H. Schwarz, and E. Witten, *Superstring Theory*, Vol. 1 (Cambridge, Uk: Univ. Pr., 1987) p. 469, Cambridge Monographs On Mathematical Physics; *Superstring Theory*, Vol. 2 (Cambridge, Uk: Univ. Pr., 1987) p. 596, Cambridge Monographs On Mathematical Physics.

[17] M. Kakizaki, S. Matsumoto, and M. Senami, *Relic abundance of dark matter in the minimal universal extra dimension model,* Phys. Rev. **D74** (2006) 023504, hep-ph/0605280.

[18] J. R. Ellis, K. A. Olive, Y. Santoso, and V. C. Spanos, *Gravitino dark matter in the CMSSM,* Phys. Lett. **B588** (2004) 7, hep-ph/0312262.

[19] F. D. Steffen, *Gravitino dark matter and cosmological constraints,* JCAP **0609** (2006) 001, hep-ph/0605306.

[20] A. Ibarra, A. Ringwald, and C. Weniger, *Hidden gauginos of an unbroken U(1): Cosmological constraints and phenomenological prospects,* JCAP **0901** (2008) 003, 0809.3196 [hep-ph].

[21] A. Ibarra, A. Ringwald, D. Tran, and C. Weniger, *Cosmic Rays from Leptophilic Dark Matter Decay via Kinetic Mixing,* JCAP **0908** (2009) 017, 0903.3625 [hep-ph].

[22] J. L. Feng, A. Rajaraman, and F. Takayama, *Superweakly-interacting massive particles,* Phys. Rev. Lett. **91** (2003) 011302, hep-ph/0302215.

[23] K. A. Olive, G. Steigman, and T. P. Walker, *Primordial Nucleosynthesis: Theory and Observations,* Phys. Rept. **333** (2000) 389, astro-ph/9905320.

[24] K. Jedamzik and M. Pospelov, *Big Bang Nucleosynthesis and Particle Dark Matter,* New J. Phys. **11** (2009) 105028, 0906.2087 [hep-ph].

[25] M. Kawasaki, K. Kohri, and T. Moroi, *Big-bang nucleosynthesis and hadronic decay of long-lived massive particles,* Phys. Rev. **D71** (2005) 083502, astro-ph/0408426.

[26] K. Jedamzik, *Big bang nucleosynthesis constraints on hadronically and electromagnetically decaying relic neutral particles,* Phys. Rev. **D74** (2006) 103509, hep-ph/0604251.

[27] R. H. Cyburt *et al.*, *Nucleosynthesis Constraints on a Massive Gravitino in Neutralino Dark Matter Scenarios,* JCAP **0910** (2009) 021, 0907.5003 [astro-ph.CO].

[28] M. Pospelov, *Particle physics catalysis of thermal big bang nucleosynthesis,* Phys. Rev. Lett. **98** (2007) 231301, hep-ph/0605215.

[29] M. Pospelov, J. Pradler, and F. D. Steffen, *Constraints on Supersymmetric Models from Catalytic Primordial Nucleosynthesis of Beryllium,* JCAP **0811** (2008) 020, 0807.4287 [hep-ph].

[30] E. W. Kolb and M. S. Turner, *The Early Universe* (Front. Phys., 1990).

[31] J. A. R. Cembranos, J. L. Feng, A. Rajaraman, and F. Takayama, *SuperWIMP solutions to small scale structure problems,* Phys. Rev. Lett. **95** (2005) 181301, hep-ph/0507150.

[32] P. McDonald *et al.* (**SDSS** Collaboration), *The Lyman-alpha Forest Power Spectrum from the Sloan Digital Sky Survey,* Astrophys. J. Suppl. **163** (2006) 80, astro-ph/0405013.

[33] F. Borzumati, T. Bringmann, and P. Ullio, *Dark matter from late decays and the small-scale structure problems,* Phys. Rev. **D77** (2008) 063514, hep-ph/0701007.

[34] L. E. Strigari, M. Kaplinghat, and J. S. Bullock, *Dark Matter Halos with Cores from Hierarchical Structure Formation,* Phys. Rev. **D75** (2007) 061303, astro-ph/0606281.

[35] M. Viel, J. Lesgourgues, M. G. Haehnelt, S. Matarrese, and A. Riotto, *Can sterile neutrinos be ruled out as warm dark matter candidates?.* Phys. Rev. Lett. **97** (2006) 071301, astro-ph/0605706.

[36] U. Seljak, A. Makarov, P. McDonald, and H. Trac, *Can sterile neutrinos be the dark matter?.* Phys. Rev. Lett. **97** (2006) 191303, astro-ph/0602430.

[37] A. A. Klypin, A. V. Kravtsov, O. Valenzuela, and F. Prada, *Where are the missing galactic satellites?.* Astrophys. J. **522** (1999) 82, astro-ph/9901240.

[38] M. Kaplinghat, *Dark matter from early decays,* Phys. Rev. **D72** (2005) 063510, astro-ph/0507300.

[39] W. Buchmüller, L. Covi, K. Hamaguchi, A. Ibarra, and T. Yanagida, *Gravitino dark matter in R-parity breaking vacua,* JHEP **03** (2007) 037, hep-ph/0702184.

[40] W. Buchmüller, K. Hamaguchi, M. Ratz, and T. Yanagida, *Supergravity at colliders,* Phys. Lett. **B588** (2004) 90, hep-ph/0402179.

[41] G. Bertone, W. Buchmüller, L. Covi, and A. Ibarra, *Gamma-Rays from Decaying Dark Matter,* JCAP **0711** (2007) 003, 0709.2299 [astro-ph].

[42] D. Eichler, *TeV particles as weakly unstable dark matter,* Phys. Rev. Lett. **63** (1989) 2440.

[43] A. Arvanitaki *et al.*, *Astrophysical Probes of Unification,* Phys. Rev. **D79** (2009) 105022, 0812.2075 [hep-ph].

[44] T. Hambye, *Hidden vector dark matter,* JHEP **01** (2009) 028, 0811.0172 [hep-ph].

[45] C. Arina, T. Hambye, A. Ibarra, and C. Weniger, *Intense Gamma-Ray Lines from Hidden Vector Dark Matter Decay,* (2009), 0912.4496 [hep-ph].

[46] Y. Gong and X. Chen, *Cosmological Constraints on Invisible Decay of Dark Matter,* Phys. Rev. **D77** (2008) 103511, 0802.2296 [astro-ph].

[47] S. De Lope Amigo, W. M.-Y. Cheung, Z. Huang, and S.-P. Ng, *Cosmological Constraints on Decaying Dark Matter,* JCAP **0906** (2009) 005, 0812.4016 [hep-ph].

[48] E. Nardi, F. Sannino, and A. Strumia, *Decaying Dark Matter can explain the electron/positron excesses,* JCAP **0901** (2009) 043, 0811.4153 [hep-ph].

[49] A. Ibarra, D. Tran, and C. Weniger, *Decaying Dark Matter in Light of the PAMELA and Fermi LAT Data,* JCAP **1001** (2010) 009, 0906.1571 [hep-ph].

[50] A. Bouquet, P. Salati, and J. Silk, *Gamma-ray lines as a probe for a cold dark matter halo,* Phys. Rev. **D40** (1989) 3168.

[51] E. A. Baltz and J. Edsjo, *Positron Propagation and Fluxes from Neutralino Annihilation in the Halo,* Phys. Rev. **D59** (1999) 023511, astro-ph/9808243.

[52] P. Ullio, L. Bergstrom, J. Edsjo, and C. G. Lacey, *Cosmological dark matter annihilations into gamma-rays: A closer look,* Phys. Rev. **D66** (2002) 123502, astro-ph/0207125.

[53] L. Pieri, J. Lavalle, G. Bertone, and E. Branchini, *Implications of High-Resolution Simulations on Indirect Dark Matter Searches,* (2009), 0908.0195 [astro-ph.HE].

[54] A. Ibarra, D. Tran, and C. Weniger, *Detecting Gamma-Ray Anisotropies from Decaying Dark Matter: Prospects for Fermi LAT,* (2009), to appear in Phys. Rev. D, 0909.3514 [hep-ph].

[55] P. L. Nolan *et al.*, *EGRET Observations of Gamma Rays from Point Sources with Galactic Latitude +10(degrees) $< b <$ +40(degrees),* Astrophys. J. **459** (1996) 100, astro-ph/9509023.

[56] A. W. Strong, I. V. Moskalenko, and O. Reimer, *Diffuse Galactic continuum gamma rays. A model compatible with EGRET data and*

cosmic-ray measurements, Astrophys. J. **613** (2004) 962, astro-ph/0406254.

[57] A. N. Cillis and R. C. Hartman, *EGRET diffuse gamma-ray maps between 30-MeV and 10-GeV,* Astrophys. J. **621** (2005) 291.

[58] P. Sreekumar *et al.* (**EGRET** Collaboration), *EGRET observations of the extragalactic gamma ray emission,* Astrophys. J. **494** (1998) 523, astro-ph/9709257.

[59] A. W. Strong, I. V. Moskalenko, and O. Reimer, *A new determination of the extragalactic diffuse gamma-ray background from EGRET data,* Astrophys. J. **613** (2004) 956, astro-ph/0405441.

[60] A. W. Strong, I. V. Moskalenko, and V. S. Ptuskin, *Cosmic-ray propagation and interactions in the Galaxy,* Ann. Rev. Nucl. Part. Sci. **57** (2007) 285, astro-ph/0701517.

[61] C. D. Dermer, *The Extragalactic Gamma Ray Background,* AIP Conf. Proc. **921** (2007) 122, 0704.2888 [astro-ph].

[62] V. Berezinsky, A. Bottino, and G. Mignola, *High-energy gamma radiation from the galactic center due to neutralino annihilation,* Phys. Lett. **B325** (1994) 136, hep-ph/9402215; L. Bergstrom, P. Ullio, and J. H. Buckley, *Observability of gamma rays from dark matter neutralino annihilations in the Milky Way halo,* Astropart. Phys. **9** (1998) 137, astro-ph/9712318; P. Gondolo and J. Silk, *Dark matter annihilation at the galactic center,* Phys. Rev. Lett. **83** (1999) 1719, astro-ph/9906391; P. D. Serpico and G. Zaharijas, *Optimal angular window for observing Dark Matter annihilation from the Galactic Center region: the case of $\gamma-$ray lines,* Astropart. Phys. **29** (2008) 380, 0802.3245 [astro-ph].

[63] M. Cirelli and P. Panci, *Inverse Compton constraints on the Dark Matter e+e- excesses,* Nucl. Phys. **B821** (2009) 399, 0904.3830 [astro-ph.CO].

[64] K. Ishiwata, S. Matsumoto, and T. Moroi, *Cosmic Gamma-ray from Inverse Compton Process in Unstable Dark Matter Scenario,* Phys. Lett. **B679** (2009) 1, 0905.4593 [astro-ph.CO].

[65] M. D. Kistler and J. M. Siegal-Gaskins, *Gamma-ray signatures of annihilation to charged leptons in dark matter substructure,* (2009), 0909.0519 [astro-ph.HE].

[66] S. Profumo and T. E. Jeltema, *Extragalactic Inverse Compton Light from Dark Matter Annihilation and the Pamela Positron Excess,* JCAP **0907** (2009) 020, 0906.0001 [astro-ph.CO].

[67] J. Zhang *et al.*, *Discriminating different scenarios to account for the cosmic e+/- excess by synchrotron and inverse Compton radiation,* Phys. Rev. **D80** (2009) 023007, 0812.0522 [astro-ph].

[68] E. Borriello, A. Cuoco, and G. Miele, *Secondary radiation from the Pamela/ATIC excess and relevance for Fermi,* Astrophys. J. **699** (2009) L59, 0903.1852 [astro-ph.GA].

[69] M. Pohl and D. Eichler, *Fermi Constrains Dark Matter Origin of High Energy Positron Anomaly,* (2009), 0912.1203 [astro-ph.HE].

[70] L. Zhang, C. Weniger, L. Maccione, J. Redondo, and G. Sigl, *Constraining Decaying Dark Matter with Fermi LAT Gamma-rays,* (2009), 0912.4504 [astro-ph.HE].

[71] E. A. Baltz *et al.*, *Pre-launch estimates for GLAST sensitivity to Dark Matter annihilation signals,* JCAP **0807** (2008) 013, 0806.2911 [astro-ph].

[72] C.-R. Chen, S. K. Mandal, and F. Takahashi, *Gamma-ray Constraints on Hadronic and Leptonic Activities of Decaying Dark Matter,* (2009), 0910.2639 [hep-ph].

[73] M. Cirelli, P. Panci, and P. D. Serpico, *Diffuse gamma ray constraints on annihilating or decaying Dark Matter after Fermi,* (2009), 0912.0663 [astro-ph.CO].

[74] M. Papucci and A. Strumia, *Robust implications on Dark Matter from the first FERMI sky gamma map,* (2009), 0912.0742 [hep-ph].

[75] O. Adriani *et al.* (**PAMELA** Collaboration), *An anomalous positron abundance in cosmic rays with energies 1.5-100 GeV,* Nature **458** (2009) 607, 0810.4995 [astro-ph].

[76] A. A. Abdo *et al.* (**The Fermi LAT** Collaboration), *Measurement of the Cosmic Ray e+ plus e- spectrum from 20 GeV to 1 TeV with the Fermi Large Area Telescope,* Phys. Rev. Lett. **102** (2009) 181101, 0905.0025 [astro-ph.HE].

[77] V. L. Ginzburg, V. A. Dogiel, V. S. Berezinsky, S. V. Bulanov, and V. S. Ptuskin, *Astrophysics of cosmic rays* (Amsterdam, Netherlands: North-Holland, 1990) p. 534.

[78] A. W. Strong, I. V. Moskalenko, and O. Reimer, *Diffuse continuum gamma rays from the Galaxy,* Astrophys. J. **537** (2000) 763, astro-ph/9811296.

[79] T. Delahaye *et al.*, *Galactic secondary positron flux at the Earth,* Astron. Astrophys. **501** (2009) 821, 0809.5268 [astro-ph].

[80] F. Aharonian *et al.* (**H.E.S.S.** Collaboration), *The energy spectrum of cosmic-ray electrons at TeV energies,* Phys. Rev. Lett. **101** (2008) 261104, 0811.3894 [astro-ph].

[81] F. Aharonian *et al.* (**H.E.S.S.** Collaboration), *Probing the ATIC peak in the cosmic-ray electron spectrum with H.E.S.S,* Astron. & Astrophys. **508** (2009) 561, 0905.0105 [astro-ph.HE].

[82] A. Ibarra and D. Tran, *Decaying Dark Matter and the PAMELA Anomaly,* JCAP **0902** (2009) 021, 0811.1555 [hep-ph].

[83] A. Ibarra and D. Tran, *Antimatter Signatures of Gravitino Dark Matter Decay,* JCAP **0807** (2008) 002, 0804.4596 [astro-ph].

[84] C.-R. Chen, F. Takahashi, and T. T. Yanagida, *Gamma rays and positrons from a decaying hidden gauge boson,* Phys. Lett. **B671** (2009) 71, 0809.0792 [hep-ph].

[85] C.-R. Chen and F. Takahashi, *Cosmic rays from Leptonic Dark Matter,* JCAP **0902** (2009) 004, 0810.4110 [hep-ph].

[86] P.-f. Yin *et al.*, *PAMELA data and leptonically decaying dark matter,* Phys. Rev. **D79** (2009) 023512, 0811.0176 [hep-ph].

[87] K. Hamaguchi, S. Shirai, and T. T. Yanagida, *Cosmic Ray Positron and Electron Excess from Hidden- Fermion Dark Matter Decays,* Phys. Lett. **B673** (2009) 247, 0812.2374 [hep-ph].

[88] M. Pospelov and M. Trott, *R-parity preserving super-WIMP decays,* JHEP **04** (2009) 044, 0812.0432 [hep-ph].

[89] S. Shirai, F. Takahashi, and T. T. Yanagida, *Decaying Hidden Gaugino as a Source of PAMELA/ATIC Anomalies,* (2009), 0902.4770 [hep-ph].

[90] A. Arvanitaki *et al.*, *Decaying Dark Matter as a Probe of Unification and TeV Spectroscopy,* Phys. Rev. **D80** (2009) 055011, 0904.2789 [hep-ph].

[91] K. J. Bae and B. Kyae, *PAMELA/ATIC Anomaly from Exotic Mediated Dark Matter Decay,* JHEP **05** (2009) 102, 0902.3578 [hep-ph].

[92] S.-L. Chen, R. N. Mohapatra, S. Nussinov, and Y. Zhang, *R-Parity Breaking via Type II Seesaw, Decaying Gravitino Dark Matter and PAMELA Positron Excess,* Phys. Lett. **B677** (2009) 311, 0903.2562 [hep-ph].

[93] K. Cheung, P.-Y. Tseng, and T.-C. Yuan, *Double-action dark matter, PAMELA and ATIC,* Phys. Lett. **B678** (2009) 293, 0902.4035 [hep-ph].

[94] H. Fukuoka, J. Kubo, and D. Suematsu, *Anomaly Induced Dark Matter Decay and PAMELA/ATIC Experiments,* Phys. Lett. **B678** (2009) 401, 0905.2847 [hep-ph].

[95] J. Hisano, K. Nakayama, and M. J. S. Yang, *Upward muon signals at neutrino detectors as a probe of dark matter properties,* Phys. Lett. **B678** (2009) 101, 0905.2075 [hep-ph].

[96] K. Kohri, A. Mazumdar, N. Sahu, and P. Stephens, *Probing Unified Origin of Dark Matter and Baryon Asymmetry at PAMELA/Fermi,* Phys. Rev. **D80** (2009) 061302, 0907.0622 [hep-ph].

[97] J. Mardon, Y. Nomura, and J. Thaler, *Cosmic Signals from the Hidden Sector,* Phys. Rev. **D80** (2009) 035013, 0905.3749 [hep-ph].

[98] N. Okada and T. Yamada, *The PAMELA and Fermi signals from long-lived Kaluza-Klein dark matter,* Phys. Rev. **D80** (2009) 075010, 0905.2801 [hep-ph].

[99] S. Shirai, F. Takahashi, and T. T. Yanagida, *R-violating Decay of Wino Dark Matter and electron/positron Excesses in the PAMELA/Fermi Experiments,* Phys. Lett. **B680** (2009) 485, 0905.0388 [hep-ph].

[100] C.-H. Chen, C.-Q. Geng, and D. V. Zhuridov, *Neutrino Masses, Leptogenesis and Decaying Dark Matter,* JCAP **0910** (2009) 001, 0906.1646 [hep-ph].

[101] C.-H. Chen, C.-Q. Geng, and D. V. Zhuridov, *Resolving Fermi, PAMELA and ATIC anomalies in split supersymmetry without R-parity,* (2009), 0905.0652 [hep-ph].

[102] W. Buchmüller, A. Ibarra, T. Shindou, F. Takayama, and D. Tran, *Probing Gravitino Dark Matter,* JCAP **0909** (2009) 021, 0906.1187 [hep-ph].

[103] I. Cholis, D. P. Finkbeiner, L. Goodenough, and N. Weiner, *The PAMELA Positron Excess from Annihilations into a Light Boson,* JCAP **0912** (2009) 007, 0810.5344 [astro-ph].

[104] P. J. Fox and E. Poppitz, *Leptophilic Dark Matter,* Phys. Rev. **D79** (2009) 083528, 0811.0399 [hep-ph].

[105] K. Ishiwata, S. Matsumoto, and T. Moroi, *Cosmic-Ray Positron from Superparticle Dark Matter and the PAMELA Anomaly,* Phys. Lett. **B675** (2009) 446, 0811.0250 [hep-ph].

[106] M. Cirelli, M. Kadastik, M. Raidal, and A. Strumia, *Model-independent implications of the e+, e-, anti-proton cosmic ray spectra on properties of Dark Matter,* Nucl. Phys. **B813** (2009) 1, 0809.2409 [hep-ph].

[107] G. Bertone, M. Cirelli, A. Strumia, and M. Taoso, *Gamma-ray and radio tests of the e+e- excess from DM annihilations,* JCAP **0903** (2009) 009, 0811.3744 [astro-ph].

[108] L. Bergstrom, J. Edsjo, and G. Zaharijas, *Dark matter interpretation of recent electron and positron data,* Phys. Rev. Lett. **103** (2009) 031103, 0905.0333 [astro-ph.HE].

[109] P. Meade, M. Papucci, A. Strumia, and T. Volansky, *Dark Matter Interpretations of the Electron/Positron Excesses after FERMI,* (2009), 0905.0480 [hep-ph].

[110] X.-J. Bi *et al.*, *Non-Thermal Production of WIMPs, Cosmic $e^{\pm}$ Excesses and γ-rays from the Galactic Center,* Phys. Rev. **D80** (2009) 103502, 0905.1253 [hep-ph].

[111] F. Chen, J. M. Cline, and A. R. Frey, *Nonabelian dark matter: models and constraints,* Phys. Rev. **D80** (2009) 083516, 0907.4746 [hep-ph].

[112] O. Adriani *et al.*, *A new measurement of the antiproton-to-proton flux ratio up to 100 GeV in the cosmic radiation,* Phys. Rev. Lett. **102** (2009) 051101, 0810.4994 [astro-ph].

[113] S. Profumo, *Dissecting Pamela (and ATIC) with Occam's Razor: existing, well-known Pulsars naturally account for the 'anomalous' Cosmic-Ray Electron and Positron Data,* (2008), 0812.4457 [astro-ph].

[114] D. Grasso *et al.* (**FERMI-LAT** Collaboration), *On possible interpretations of the high energy electron- positron spectrum measured by the Fermi Large Area Telescope,* Astropart. Phys. **32** (2009) 140, 0905.0636 [astro-ph.HE].

[115] D. Hooper, P. Blasi, and P. D. Serpico, *Pulsars as the Sources of High Energy Cosmic Ray Positrons,* JCAP **0901** (2009) 025, 0810.1527 [astro-ph].

[116] A. K. Harding and R. Ramaty, Proc. 20th ICRC, Moscow **2** (1987) 92.

[117] A. M. Atoian, F. A. Aharonian, and H. J. Volk, *Electrons and positrons in the galactic cosmic rays,* Phys. Rev. **D52** (1995) 3265.

[118] X. Chi, E. C. M. Young, and K. S. Cheng, *Pulsar-wind origin of cosmic ray positrons,* Astrophys. J. **459** (1995) L83.

[119] H. Yuksel, M. D. Kistler, and T. Stanev, *TeV Gamma Rays from Geminga and the Origin of the GeV Positron Excess,* Phys. Rev. Lett. **103** (2009) 051101, 0810.2784 [astro-ph].

[120] C. Grimani, *Pulsar birthrate set by cosmic-ray positron observations,* Astron. Astrophys. **418** (2004) 649.

[121] D. Malyshev, I. Cholis, and J. Gelfand, *Pulsars versus Dark Matter Interpretation of ATIC/PAMELA,* Phys. Rev. **D80** (2009) 063005, 0903.1310 [astro-ph.HE].

[122] M. Regis and P. Ullio, *Testing the Dark Matter Interpretation of the PAMELA Excess through Measurements of the Galactic Diffuse Emission,* Phys. Rev. **D80** (2009) 043525, 0904.4645 [astro-ph.GA].

[123] K. R. Dienes, C. F. Kolda, and J. March-Russell, *Kinetic mixing and the supersymmetric gauge hierarchy,* Nucl. Phys. **B492** (1997) 104, hep-ph/9610479.

[124] R. Blumenhagen, G. Honecker, and T. Weigand, *Loop-corrected compactifications of the heterotic string with line bundles,* JHEP **06** (2005) 020, hep-th/0504232.

[125] O. Lebedev *et al.*, *A mini-landscape of exact MSSM spectra in heterotic orbifolds,* Phys. Lett. **B645** (2007) 88, hep-th/0611095.

[126] S. A. Abel, J. Jaeckel, V. V. Khoze, and A. Ringwald, *Illuminating the hidden sector of string theory by shining light through a magnetic field,* Phys. Lett. **B666** (2008) 66, hep-ph/0608248.

[127] S. A. Abel, M. D. Goodsell, J. Jaeckel, V. V. Khoze, and A. Ringwald, *Kinetic Mixing of the Photon with Hidden U(1)s in String Phenomenology,* JHEP **07** (2008) 124, 0803.1449 [hep-ph].

[128] M. Goodsell, J. Jaeckel, J. Redondo, and A. Ringwald, *Naturally Light Hidden Photons in LARGE Volume String Compactifications,* JHEP **11** (2009) 027, 0909.0515 [hep-ph].

[129] A. Arvanitaki, N. Craig, S. Dimopoulos, S. Dubovsky, and J. March-Russell, *String Photini at the LHC,* (2009), 0909.5440 [hep-ph].

[130] W.-F. Chang, J. N. Ng, and J. M. S. Wu, *A very narrow shadow extra Z-boson at colliders,* Phys. Rev. **D74** (2006) 095005, hep-ph/0608068.

[131] J. Kumar and J. D. Wells, *LHC and ILC probes of hidden-sector gauge bosons,* Phys. Rev. **D74** (2006) 115017, hep-ph/0606183.

[132] K. Cheung and T.-C. Yuan, *Hidden fermion as milli-charged dark matter in Stueckelberg Z' model,* JHEP **03** (2007) 120, hep-ph/0701107.

[133] D. Feldman, Z. Liu, and P. Nath, *The Stueckelberg Z' extension with kinetic mixing and milli-charged dark matter from the hidden sector,* Phys. Rev. **D75** (2007) 115001, hep-ph/0702123.

[134] P. Langacker, *The Physics of Heavy Z' Gauge Bosons,* (2008), 0801.1345 [hep-ph].

[135] M. Pospelov, A. Ritz, and M. B. Voloshin, *Bosonic super-WIMPs as keV-scale dark matter,* Phys. Rev. **D78** (2008) 115012, 0807.3279 [hep-ph].

[136] B. Kors and P. Nath, *A supersymmetric Stueckelberg U(1) extension of the MSSM,* JHEP **12** (2004) 005, hep-ph/0406167.

[137] B. Kors and P. Nath, *Aspects of the Stueckelberg extension,* JHEP **07** (2005) 069, hep-ph/0503208.

[138] D. Feldman, B. Kors, and P. Nath, *Extra-weakly interacting dark matter,* Phys. Rev. **D75** (2007) 023503, hep-ph/0610133.

[139] L. J. Hall, K. Jedamzik, J. March-Russell, and S. M. West, *Freeze-In Production of FIMP Dark Matter,* (2009), 0911.1120 [hep-ph].

[140] M. Fukugita and T. Yanagida, *Baryogenesis Without Grand Unification,* Phys. Lett. **B174** (1986) 45.

[141] W. Buchmüller, P. Di Bari, and M. Plumacher, *Leptogenesis for pedestrians,* Ann. Phys. **315** (2005) 305, `hep-ph/0401240`.

[142] W. Buchmüller, R. D. Peccei, and T. Yanagida, *Leptogenesis as the origin of matter,* Ann. Rev. Nucl. Part. Sci. **55** (2005) 311, `hep-ph/0502169`.

[143] D. Hooper and P. D. Serpico, *Angular Signatures of Dark Matter in the Diffuse Gamma Ray Spectrum,* JCAP **0706** (2007) 013, `astro-ph/0702328`.

[144] C. Wetterich, *Cosmology and the Fate of Dilatation Symmetry,* Nucl. Phys. **B302** (1988) 668; B. Ratra and P. J. E. Peebles, *Cosmological Consequences of a Rolling Homogeneous Scalar Field,* Phys. Rev. **D37** (1988) 3406.

[145] J. Khoury and A. Weltman, *Chameleon cosmology,* Phys. Rev. **D69** (2004) 044026, `astro-ph/0309411`.

[146] M. Ahlers, A. Lindner, A. Ringwald, L. Schrempp, and C. Weniger, *Alpenglow - A Signature for Chameleons in Axion-Like Particle Search Experiments,* Phys. Rev. **D77** (2008) 015018, `0710.1555 [hep-ph]`; H. Gies, D. F. Mota, and D. J. Shaw, *Hidden in the Light: Magnetically Induced Afterglow from Trapped Chameleon Fields,* **D77** (2008) 025016, `0710.1556 [hep-ph]`.

[147] J. R. Ellis, J. S. Hagelin, D. V. Nanopoulos, K. A. Olive, and M. Srednicki, *Supersymmetric relics from the big bang,* Nucl. Phys. **B238** (1984) 453.

[148] M. Trodden and S. M. Carroll, *TASI lectures: Introduction to cosmology,* (2004), TASI lectures: Introduction to cosmology, `astro-ph/0401547`.

[149] S. M. Carroll, *Spacetime and geometry: An introduction to general relativity* (San Francisco, USA: Addison-Wesley, 2004) p. 513.

[150] M. Taoso, G. Bertone, and A. Masiero, *Dark Matter Candidates: A Ten-Point Test,* JCAP **0803** (2008) 022, 0711.4996 [astro-ph].

[151] K. G. Begeman, A. H. Broeils, and R. H. Sanders, *Extended rotation curves of spiral galaxies: Dark haloes and modified dynamics,* Mon. Not. Roy. Astron. Soc. **249** (1991) 523.

[152] M. Mateo, *Dwarf Galaxies of the Local Group,* Ann. Rev. Astron. Astrophys. **36** (1998) 435, astro-ph/9810070.

[153] D. Clowe *et al.*, *A direct empirical proof of the existence of dark matter,* Astrophys. J. **648** (2006) L109, astro-ph/0608407.

[154] M. Milgrom, *A Modification of the Newtonian dynamics as a possible alternative to the hidden mass hypothesis,* Astrophys. J. **270** (1983) 365; *The MOND paradigm,* (2008), 0801.3133 [astro-ph].

[155] P. M. Garnavich *et al.* (**Supernova Search Team** Collaboration), *Supernova Limits on the Cosmic Equation of State,* Astrophys. J. **509** (1998) 74, astro-ph/9806396.

[156] S. Perlmutter *et al.* (**Supernova Cosmology Project** Collaboration), *Measurements of Omega and Lambda from 42 High-Redshift Supernovae,* Astrophys. J. **517** (1999) 565, astro-ph/9812133.

[157] A. G. Riess *et al.* (**Supernova Search Team** Collaboration), *Observational Evidence from Supernovae for an Accelerating Universe and a Cosmological Constant,* Astron. J. **116** (1998) 1009, astro-ph/9805201.

[158] D. N. Spergel *et al.* (**WMAP** Collaboration), *First Year Wilkinson Microwave Anisotropy Probe (WMAP) Observations: Determination of Cosmological Parameters,* Astrophys. J. Suppl. **148** (2003) 175, astro-ph/0302209.

[159] S. W. Allen, R. W. Schmidt, and A. C. Fabian, *Cosmological constraints from the X-ray gas mass fraction in relaxed lensing clusters observed with Chandra,* Mon. Not. Roy. Astron. Soc. **334** (2002) L11, astro-ph/0205007.

[160] J. Dunkley *et al.* (**WMAP** Collaboration), *Five-Year Wilkinson Microwave Anisotropy Probe (WMAP) Observations: Likelihoods and Parameters from the WMAP data,* Astrophys. J. Suppl. **180** (2009) 306, 0803.0586 [astro-ph].

[161] S. L. Glashow, *Partial Symmetries of Weak Interactions,* Nucl. Phys. **22** (1961) 579.

[162] S. Weinberg, *A Model of Leptons,* Phys. Rev. Lett. **19** (1967) 1264.

[163] A. Salam, *Weak and Electromagnetic Interactions,* – Originally printed in *Svartholm: Elementary Particle Theory, Proceedings Of The Nobel Symposium Held 1968 At Lerum, Sweden*, Stockholm 1968, 367-377.

[164] M. E. Peskin and D. V. Schroeder, *An Introduction to Quantum Field Theory* (Reading, USA: Addison-Wesley, 1995) p. 842.

[165] S. F. Novaes, *Standard model: An Introduction,* (1999), hep-ph/0001283.

[166] G. L. Fogli *et al.*, *Observables sensitive to absolute neutrino masses: A reappraisal after WMAP-3y and first MINOS results,* Phys. Rev. **D75** (2007) 053001, hep-ph/0608060.

[167] D. N. Spergel *et al.* (**WMAP** Collaboration), *Wilkinson Microwave Anisotropy Probe (WMAP) three year results: Implications for cosmology,* Astrophys. J. Suppl. **170** (2007) 377, astro-ph/0603449.

[168] U. Seljak, A. Slosar, and P. McDonald, *Cosmological parameters from combining the Lyman-alpha forest with CMB, galaxy clustering and SN constraints,* JCAP **0610** (2006) 014, astro-ph/0604335.

[169] J. R. Primack, *The nature of dark matter,* (2001), astro-ph/0112255.

[170] A. Boyarsky, J. Lesgourgues, O. Ruchayskiy, and M. Viel, *Lyman-alpha constraints on warm and on warm-plus-cold dark matter models,* JCAP **0905** (2009) 012, 0812.0010 [astro-ph].

[171] A. Boyarsky, J. Lesgourgues, O. Ruchayskiy, and M. Viel, *Realistic sterile neutrino dark matter with keV mass does not contradict*

cosmological bounds, Phys. Rev. Lett. **102** (2009) 201304, 0812.3256 [hep-ph].

[172] F. D. Steffen, *Supersymmetric Dark Matter Candidates - The Lightest Neutralino, the Gravitino, and the Axino,* (2007), 0711.1240 [hep-ph].

[173] H. Pagels and J. R. Primack, *Supersymmetry, Cosmology and New TeV Physics,* Phys. Rev. Lett. **48** (1982) 223.

[174] F. Takayama and M. Yamaguchi, *Gravitino dark matter without R-parity,* Phys. Lett. **B485** (2000) 388, hep-ph/0005214.

[175] L. Bergstrom, J. Edsjo, and P. Ullio, *Cosmic antiprotons as a probe for supersymmetric dark matter?.* Astrophys. J. **526** (1999) 215, astro-ph/9902012.

[176] F. Donato, N. Fornengo, D. Maurin, and P. Salati, *Antiprotons in cosmic rays from neutralino annihilation,* Phys. Rev. **D69** (2004) 063501, astro-ph/0306207.

[177] D. Spolyar, M. Buckley, K. Freese, D. Hooper, and H. Murayama, *High Energy Neutrinos As A Test of Leptophilic Dark Matter,* (2009), 0905.4764 [astro-ph.CO].

[178] M. R. Buckley, K. Freese, D. Hooper, D. Spolyar, and H. Murayama, *High-Energy Neutrino Signatures of Dark Matter Decaying into Leptons,* (2009), 0907.2385 [astro-ph.HE].

[179] A. Ibarra and D. Tran, *Antideuterons from Dark Matter Decay,* JCAP **0906** (2009) 004, 0904.1410 [hep-ph].

[180] M. Kadastik, M. Raidal, and A. Strumia, *Enhanced anti-deuteron Dark Matter signal and the implications of PAMELA,* (2009), 0908.1578 [hep-ph].

[181] J. T. Ruderman and T. Volansky, *Searching for Smoking Gun Signatures of Decaying Dark Matter,* (2009), 0907.4373 [hep-ph].

[182] D. Gorbunov, A. Khmelnitsky, and V. Rubakov, *Is gravitino still a warm dark matter candidate?.* (2008), 0805.2836 [hep-ph].

[183] J. L. Feng, S. Su, and F. Takayama, *Supergravity with a gravitino LSP,* Phys. Rev. **D70** (2004) 075019, hep-ph/0404231.

[184] V. S. Rychkov and A. Strumia, *Thermal production of gravitinos,* Phys. Rev. **D75** (2007) 075011, hep-ph/0701104.

[185] K. Hamaguchi, T. Hatsuda, M. Kamimura, Y. Kino, and T. T. Yanagida, *Stau-catalyzed Li-6 production in big-bang nucleosynthesis,* Phys. Lett. **B650** (2007) 268, hep-ph/0702274.

[186] B. Holdom, *Two U(1)'s and Epsilon Charge Shifts,* Phys. Lett. **B166** (1986) 196.

[187] R. Foot and X.-G. He, *Comment on Z Z-prime mixing in extended gauge theories,* Phys. Lett. **B267** (1991) 509.

[188] B. A. Dobrescu, *Massless gauge bosons other than the photon,* Phys. Rev. Lett. **94** (2005) 151802, hep-ph/0411004.

[189] E. Boos, V. Bunichev, and H. J. Schreiber, *Prospects of a Search for a New Massless Neutral Gauge Boson at the ILC,* Phys. Rev. **D78** (2008) 015007, 0709.4535 [hep-ph].

[190] J. L. Feng, H. Tu, and H.-B. Yu, *Thermal Relics in Hidden Sectors,* JCAP **0810** (2008) 043, 0808.2318 [hep-ph].

[191] J. Redondo, *The low energy frontier: probes with photons,* (2008), 0805.3112 [hep-ph].

[192] J. Redondo, *Helioscope Bounds on Hidden Sector Photons,* JCAP **0807** (2008) 008, 0801.1527 [hep-ph].

[193] L. B. Okun, *Limits of Electrodynamics: Paraphotons?.* Sov. Phys. JETP **56** (1982) 502.

[194] B. Holdom, *Oblique electroweak corrections and an extra gauge boson,* Phys. Lett. **B259** (1991) 329.

[195] I. J. R. Aitchison, *Supersymmetry and the MSSM: An Elementary introduction,* (2005), hep-ph/0505105.

[196] P. C. Argyres, *Lecture Notes: An Introduction to Global Supersymmetry,* (2001), http://www.physics.uc.edu/~argyres/661/susy2001.pdf.

[197] F. del Aguila, G. D. Coughlan, and M. Quiros, *Gauge Coupling Renormalisation with several U(1) factors,* Nucl. Phys. **B307** (1988) 633.

[198] D. Lüst and S. Stieberger, *Gauge threshold corrections in intersecting brane world models,* Fortsch. Phys. **55** (2007) 427, hep-th/0302221.

[199] S. A. Abel and B. W. Schofield, *Brane-antibrane kinetic mixing, millicharged particles and SUSY breaking,* Nucl. Phys. **B685** (2004) 150, hep-th/0311051.

[200] M. Berg, M. Haack, and B. Kors, *Loop corrections to volume moduli and inflation in string theory,* Phys. Rev. **D71** (2005) 026005, hep-th/0404087.

[201] G. F. Giudice and R. Rattazzi, *Theories with gauge-mediated supersymmetry breaking,* Phys. Rept. **322** (1999) 419, hep-ph/9801271.

[202] M. Bolz, A. Brandenburg, and W. Buchmüller, *Thermal Production of Gravitinos,* Nucl. Phys. **B606** (2001) 518, [Erratum-ibid. B **790** (2008) 336], hep-ph/0012052.

[203] J. Pradler and F. D. Steffen, *Thermal gravitino production and collider tests of leptogenesis,* Phys. Rev. **D75** (2007) 023509, hep-ph/0608344.

[204] E. Braaten and T. C. Yuan, *Calculation of screening in a hot plasma,* Phys. Rev. Lett. **66** (1991) 2183.

[205] M. Viel, J. Lesgourgues, M. G. Haehnelt, S. Matarrese, and A. Riotto, *Constraining warm dark matter candidates including sterile neutrinos and light gravitinos with WMAP and the Lyman-alpha forest,* Phys. Rev. **D71** (2005) 063534, astro-ph/0501562.

[206] A. Palazzo, D. Cumberbatch, A. Slosar, and J. Silk, *Sterile neutrinos as subdominant warm dark matter,* Phys. Rev. **D76** (2007) 103511, 0707.1495 [astro-ph].

[207] K. Ishiwata, S. Matsumoto, and T. Moroi, *Gravitino Dark Matter with Weak-Scale Right-Handed Sneutrino,* Phys. Rev. **D77** (2008) 035004, 0710.2968 [hep-ph].

[208] M. Viel, M. G. Haehnelt, and V. Springel, *Inferring the dark matter power spectrum from the Lyman- alpha forest in high-resolution QSO absorption spectra,* Mon. Not. Roy. Astron. Soc. **354** (2004) 684, astro-ph/0404600.

[209] J. Pradler and F. D. Steffen, *Constraints on the reheating temperature in gravitino dark matter scenarios,* Phys. Lett. **B648** (2007) 224, hep-ph/0612291.

[210] M. Kawasaki, K. Kohri, T. Moroi, and A. Yotsuyanagi, *Big-Bang Nucleosynthesis and Gravitino,* (2008), 0804.3745 [hep-ph].

[211] W. Buchmüller, K. Hamaguchi, M. Ibe, and T. T. Yanagida, *Eluding the BBN constraints on the stable gravitino,* Phys. Lett. **B643** (2006) 124, hep-ph/0605164.

[212] J. Pradler and F. D. Steffen, *Thermal relic abundances of long-lived staus,* Nucl. Phys. **B809** (2009) 318, 0808.2462 [hep-ph].

[213] M. Ratz, K. Schmidt-Hoberg, and M. W. Winkler, *A note on the primordial abundance of stau NLSPs,* JCAP **0810** (2008) 026, 0808.0829 [hep-ph].

[214] S. Kachru, R. Kallosh, A. Linde, and S. P. Trivedi, *De Sitter vacua in string theory,* Phys. Rev. **D68** (2003) 046005, hep-th/0301240.

[215] A. Ibarra and D. Tran, *Gamma Ray Spectrum from Gravitino Dark Matter Decay,* Phys. Rev. Lett. **100** (2008) 061301, 0709.4593 [astro-ph].

[216] K. Ishiwata, S. Matsumoto, and T. Moroi, *High Energy Cosmic Rays from the Decay of Gravitino Dark Matter,* Phys. Rev. **D78** (2008) 063505, 0805.1133 [hep-ph].

[217] A. Boyarsky, O. Ruchayskiy, and M. Shaposhnikov, *The role of sterile neutrinos in cosmology and astrophysics,* Ann. Rev. Nucl. Part. Sci. **59** (2009) 191, 0901.0011 [hep-ph].

[218] M. Ackermann, *Observation of the extragalactic diffuse gamma-ray emission with the Fermi Large Area Telescope,* Talk given at TeV Particle Astrophysics 2009, `www-conf.slac.stanford.edu/tevpa09/`.

[219] M. Ackermann, *Observations of the isotropic diffuse gamma-ray emission with the Fermi Large Area Telescope,* Talk given at Fermi Symposium 2009, `http://fermi.gsfc.nasa.gov/science/symposium/2009/`.

[220] T. Porter, *Galactic Diffuse Emission,* Talk given at Fermi Symposium 2009, `http://fermi.gsfc.nasa.gov/science/symposium/2009/`.

[221] S. W. Barwick *et al.* (**HEAT** Collaboration), *Measurements of the cosmic-ray positron fraction from 1 GeV to 50 GeV,* Astrophys. J. **482** (1997) L191, `astro-ph/9703192`.

[222] M. Boezio, P. Carlson, T. Francke, N. Weber, M. Suffert, *et al.*, *The Cosmic-Ray Electron and Positron Spectra Measured at 1 AU during Solar Minimum Activity,* Astrophys. J. **532** (Mar. 2000) 653.

[223] M. Aguilar *et al.* (**AMS-01** Collaboration), *Cosmic-ray positron fraction measurement from 1 GeV to 30 GeV with AMS-01,* Phys. Lett. **B646** (2007) 145, `astro-ph/0703154`.

[224] J. Chang *et al.*, *An excess of cosmic ray electrons at energies of 300-800 GeV,* Nature **456** (2008) 362.

[225] S. Torii *et al.* (**PPB-BETS** Collaboration), *High-energy electron observations by PPB-BETS flight in Antarctica,* (2008), `0809.0760 [astro-ph]`.

[226] S. Torii *et al.*, *The energy spectrum of cosmic ray electrons from 10 GeV to 100 GeV observed with a highly granulated imaging calorimeter,* Astrophys. J. **559** (2001) 973.

[227] M. Aguilar *et al.* (**AMS** Collaboration), *The Alpha Magnetic Spectrometer (AMS) on the International Space Station. I: Results from the test flight on the space shuttle,* Phys. Rept. **366** (2002) 331.

[228] M. A. DuVernois *et al.*, *Cosmic ray electrons and positrons from 1 GeV to 100 GeV: Measurements with HEAT and their interpretation,* Astrophys. J. **559** (2001) 296.

[229] H. Matsunaga *et al.*, *Measurement of low-energy cosmic-ray antiprotons at solar minimum,* Phys. Rev. Lett. **81** (1998) 4052, astro-ph/9809326.

[230] S. Orito *et al.* (**BESS** Collaboration), *Precision measurement of cosmic-ray antiproton spectrum,* Phys. Rev. Lett. **84** (2000) 1078, astro-ph/9906426.

[231] M. Boezio, P. Carlson, T. Francke, N. Weber, M. Suffert, *et al.*, *The Cosmic-Ray Antiproton Flux between 0.62 and 3.19 GeV Measured Near Solar Minimum Activity,* Astrophys. J. **487** (Sep. 1997) 415.

[232] M. Boezio, V. Bonvicini, P. Schiavon, A. Vacchi, N. Zampa, *et al.*, *The Cosmic-Ray Antiproton Flux between 3 and 49 GeV,* Astrophys. J. **561** (Nov. 2001) 787.

[233] J. W. Mitchell *et al.*, *Measurement of 0.25 GeV to 3.2 GeV anti-protons in the cosmic radiation,* Phys. Rev. Lett. **76** (1996) 3057.

[234] Y. Asaoka *et al.*, *Measurements of cosmic-ray low-energy antiproton and proton spectra in a transient period of the solar field reversal,* Phys. Rev. Lett. **88** (2002) 051101, astro-ph/0109007.

[235] A. S. Beach *et al.*, *Measurement of the cosmic-ray antiproton to proton abundance ratio between 4 GeV and 50 GeV,* Phys. Rev. Lett. **87** (2001) 271101, astro-ph/0111094.

[236] F. Donato *et al.*, *Antiprotons from spallation of cosmic rays on interstellar matter,* Astrophys. J. **563** (2001) 172, astro-ph/0103150.

[237] J. Hisano, S. Matsumoto, O. Saito, and M. Senami, *Heavy Wino-like neutralino dark matter annihilation into antiparticles,* Phys. Rev. **D73** (2006) 055004, hep-ph/0511118.

[238] T. Delahaye, R. Lineros, F. Donato, N. Fornengo, and P. Salati, *Positrons from dark matter annihilation in the galactic halo: theoretical uncertainties,* Phys. Rev. **D77** (2008) 063527, 0712.2312 [astro-ph].

[239] D. Maurin *et al.*, *Galactic cosmic ray nuclei as a tool for astroparticle physics,* (2002), astro-ph/0212111.

[240] D. Maurin, F. Donato, R. Taillet, and P. Salati, *Cosmic Rays below Z=30 in a diffusion model: new constraints on propagation parameters,* Astrophys. J. **555** (2001) 585, astro-ph/0101231.

[241] L. C. Tan and L. K. Ng, *Calculation of the equilibrium anti-proton spectrum,* J. Phys. **G9** (1983) 227.

[242] H. S. Ahn *et al.*, *Measurements of cosmic-ray secondary nuclei at high energies with the first flight of the CREAM balloon-borne experiment,* Astropart. Phys. **30** (2008) 133, 0808.1718 [astro-ph].

[243] L. J. Gleeson and W. I. Axford, *Cosmic Rays in the Interplanetary Medium,* Astrophys. J. **149** (Sep. 1967) L115; *Solar Modulation of Galactic Cosmic Rays,* **154** (Dec. 1968) 1011.

[244] J. S. Perko, *Solar modulation of galactic antiprotons,* Astron. Astrophys. **184** (Oct. 1987) 119.

[245] P. Blasi, *The origin of the positron excess in cosmic rays,* Phys. Rev. Lett. **103** (2009) 051104, 0903.2794 [astro-ph.HE].

[246] L. Covi, M. Grefe, A. Ibarra, and D. Tran, *Unstable Gravitino Dark Matter and Neutrino Flux,* JCAP **0901** (2009) 029, 0809.5030 [hep-ph].

[247] T. Sjostrand, S. Mrenna, and P. Skands, *PYTHIA 6.4 physics and manual,* JHEP **05** (2006) 026, hep-ph/0603175.

[248] J. F. Navarro, C. S. Frenk, and S. D. M. White, *The Structure of Cold Dark Matter Halos,* Astrophys. J. **462** (1996) 563, astro-ph/9508025.

[249] T. Bringmann and P. Salati, *The galactic antiproton spectrum at high energies: background expectation vs. exotic contributions,* Phys. Rev. **D75** (2007) 083006, astro-ph/0612514.

[250] A. M. Lionetto, A. Morselli, and V. Zdravkovic, *Uncertainties of cosmic ray spectra and detectability of antiproton mSUGRA*

contributions with PAMELA, JCAP **0509** (2005) 010, astro-ph/0502406.

[251] P. Gondolo *et al.*, *DarkSUSY: Computing supersymmetric dark matter properties numerically,* JCAP **0407** (2004) 008, astro-ph/0406204, http://www.physto.se/~edsjo/darksusy.

[252] T. Hahn, *Generating Feynman diagrams and amplitudes with FeynArts 3,* Comput. Phys. Commun. **140** (2001) 418, hep-ph/0012260.

[253] T. Hahn and M. Perez-Victoria, *Automatized one-loop calculations in four and D dimensions,* Comput. Phys. Commun. **118** (1999) 153, hep-ph/9807565.

[254] N. Arkani-Hamed, A. Delgado, and G. F. Giudice, *The well-tempered neutralino,* Nucl. Phys. **B741** (2006) 108, hep-ph/0601041.

[255] S. Gillessen *et al.*, *Monitoring stellar orbits around the Massive Black Hole in the Galactic Center,* Astrophys. J. **692** (2009) 1075, 0810.4674 [astro-ph].

[256] J. F. Navarro *et al.*, *The Inner Structure of LambdaCDM Halos III: Universality and Asymptotic Slopes,* Mon. Not. Roy. Astron. Soc. **349** (2004) 1039, astro-ph/0311231.

[257] V. Springel *et al.*, *The Aquarius Project: the subhalos of galactic halos,* Mon. Not. Roy. Astron. Soc. **391** (2008) 1685, 0809.0898 [astro-ph].

[258] R. Catena and P. Ullio, *A novel determination of the local dark matter density,* (2009), 0907.0018 [astro-ph.CO].

[259] R. J. Gould and G. P. Schreder, *Pair Production in Photon-Photon Collisions,* Phys. Rev. **155** (1967) 1404.

[260] F. W. Stecker, M. A. Malkan, and S. T. Scully, *Intergalactic photon spectra from the far IR to the UV Lyman limit for $0 < z < 6$ and the optical depth of the universe to high energy gamma-rays,* Astrophys. J. **648** (2006) 774, astro-ph/0510449.

[261] A. Cuoco, J. Brandbyge, S. Hannestad, T. Haugboelle, and G. Miele, *Angular Signatures of Annihilating Dark Matter in the Cosmic Gamma-Ray Background,* Phys. Rev. **D77** (2008) 123518, 0710.4136 [astro-ph].

[262] I. V. Moskalenko, T. A. Porter, and A. W. Strong, *Attenuation of VHE gamma rays by the Milky Way interstellar radiation field,* Astrophys. J. **640** (2006) L155, astro-ph/0511149.

[263] G. R. Blumenthal and R. J. Gould, *Bremsstrahlung, synchrotron radiation, and compton scattering of high-energy electrons traversing dilute gases,* Rev. Mod. Phys. **42** (1970) 237.

[264] L. Zhang, G. Sigl, and J. Redondo, *Galactic Signatures of Decaying Dark Matter,* JCAP **0909** (2009) 012, 0905.4952 [astro-ph.GA].

[265] K. Ishiwata, S. Matsumoto, and T. Moroi, *Synchrotron Radiation from the Galactic Center in Decaying Dark Matter Scenario,* Phys. Rev. **D79** (2009) 043527, 0811.4492 [astro-ph].

[266] I. V. Moskalenko and A. W. Strong, *Anisotropic inverse Compton scattering in the Galaxy,* Astrophys. J. **528** (2000) 357, astro-ph/9811284.

[267] T. A. Porter and A. W. Strong, *A new estimate of the Galactic interstellar radiation field between 0.1 microns and 1000 microns,* (2005), astro-ph/0507119.

[268] C. Calcaneo-Roldan and B. Moore, *The surface brightness of dark matter: Unique signatures of neutralino annihilation in the galactic halo,* Phys. Rev. **D62** (2000) 123005, astro-ph/0010056.

[269] I. V. Moskalenko and T. A. Porter, *Isotropic Gamma-Ray Background: Cosmic-Ray Induced Albedo from Debris in the Solar System?.* Astrophys. J. **692** (2009) 54, 0901.0304 [astro-ph.HE].

[270] V. Barger, Y. Gao, W. Y. Keung, and D. Marfatia, *Generic dark matter signature for gamma-ray telescopes,* Phys. Rev. **D80** (2009) 063537, 0906.3009 [hep-ph].

[271] G. Dobler, D. P. Finkbeiner, I. Cholis, T. R. Slatyer, and N. Weiner, *The Fermi Haze: A Gamma-Ray Counterpart to the Microwave Haze,* (2009), 0910.4583 [astro-ph.HE].

[272] D. Suematsu, *Vacuum structure of the mu-problem solvable extra U(1) models,* Phys. Rev. **D59** (1999) 055017, hep-ph/9808409.

[273] J. Rosiek, *Complete Set of Feynman Rules for the Minimal Supersymmetric Extension of the Standard Model,* Phys. Rev. **D41** (1990) 3464, [Erratum hep-ph/9511250 (1995)].

[274] H. E. Haber and D. Wyler, *Radiative Neutralino Decay,* Nucl. Phys. **B323** (1989) 267.

[275] A. Bartl, H. Fraas, and W. Majerotto, *Production and Decay of Neutralinos in e+e- Annihilation,* Nucl. Phys. **B278** (1986) 1.

[276] K. Kohri, T. Moroi, and A. Yotsuyanagi, *Big-bang nucleosynthesis with unstable gravitino and upper bound on the reheating temperature,* Phys. Rev. **D73** (2006) 123511, hep-ph/0507245.

Acknoweledgments

I am deeply grateful to my supervisor Andreas Ringwald for his professional and personal support and advice in the last three years, and for giving me the opportunity to work with him and others at DESY on exciting topics in theoretical high-energy and astroparticle physics. I am also very thankful to Alejandro Ibarra and David Tran in whose collaboration most of the work presented in this thesis was done. Furthermore I want to thank the people at the DESY theory group for the inspiring environment, with doors always open for questions and discussions, in particular Wilfried Buchmüller, Laura Covi and Günter Sigl. I thank all the people that made life in general, in Hamburg and at DESY pleasurable, in particular Ruth Tietjen, my awesome band colleagues Sebastian Mendizabal, Chloé Papineau, Javier Redondo and Jonas Schmidt, my office colleagues Alexander Goritschnig and Jan Hajer, and the people from the second floor, including Clare Burrage, Mark Goodsell, Thomas Hack, Christian Hambrock, Cecelie Hector, Kai Keller and Saul Ramos.